NATIONAL ACADEMY OF SCIENCES OF UKRAINE
INSTITUTE OF MACROMOLECULAR CHEMISTRY
OF THE NAS OF UKRAINE

НАЦІОНАЛЬНА АКАДЕМІЯ НАУК УКРАЇНИ
ІНСТИТУТ ХІМІЇ ВИСОКОМОЛЕКУЛЯРНИХ СПОЛУК
НАН УКРАЇНИ

ОЛЕКСАНДР ФАЙНЛЕЙБ
ОЛЬГА ГРИГОР'ЄВА
ОЛЬГА СТАРОСТЕНКО
КРІСТІНА ГУСАКОВА
ДАНІЕЛЬ ГРАНДЕ

ТЕРМОСТІЙКІ НАНОПОРИСТІ ПОЛІЦІАНУРАТИ

ПРОЄКТ
«УКРАЇНСЬКА НАУКОВА КНИГА
ІНОЗЕМНОЮ МОВОЮ»

КИЇВ
АКАДЕМПЕРІОДИКА
2023

ALEXANDER FAINLEIB
OLGA GRIGORYEVA
OLGA STAROSTENKO
KRISTINA GUSAKOVA
DANIEL GRANDE

THERMOSTABLE NANOPOROUS POLYCYANURATES

PROJECT
«UKRAINIAN SCIENTIFIC BOOK
IN A FOREIGN LANGUAGE»

KYIV
AKADEMPERIODYKA
2023

https://doi.org/10.15407/akademperiodyka.477.112
UDC 66.095.26
T37

Reviewers:

Valery SHEVCHENKO, Institute of Macromolecular Chemistry of the National Academy of Sciences of Ukraine, Head of Department of Chemistry of Oligomers and Network polymers, Corresponding Member of the NAS of Ukraine, PhD, Doctor of Sciences, Professor; https://orcid.org/0000-0003-2100-4468

Oleksandr PUD, V.P. Kukhar Institute of Bioorganic Chemistry and Petrochemistry of the National Academy of Sciences of Ukraine, Head of Department of Chemistry of Functional Materials, PhD, Doctor of Sciences, Professor; https://orcid.org/0000-0002-0681-633X

Borys GORELOV, Chuiko Institute of Surface Chemistry of the National Academy of Sciences of Ukraine, Head of Department of Composite Materials, PhD, Doctor of Sciences; https://orcid.org/0000-0002-1211-0579

Approved for publication by Institute of Macromolecular Chemistry of the NAS of Ukraine (October, 18, 2022, Protocol No. 5)

The publication was funded within the framework of the Targeted Complex Program of the NAS of Ukraine "Scientific Bases of Functioning and Providing for Conditions for the Development of the Scientific and Publishing Complex of the NAS of Ukraine"

Thermostable Nanoporous Polycyanurates / Alexander
T37 Fainleib, Olga Grigoryeva, Olga Starostenko, Kristina Gusakova, Daniel Grande; Institute of Macromolecular Chemistry of the NAS of Ukraine. — Kyiv: Akademperiodyka, 2023. — 112 p.

ISBN 978-966-360-477-0

The monograph is devoted to the synthesis, analysis of the structure and morphology, porosity parameters and physicochemical properties of heat-resistant nanoporous polycyanurates, as well as the possibility of their application for gas separation. Nanoporous films obtained using reactive and inert porogens, high-boiling-temperature liquids, incomplete conversion of cyanate monomers, as well as radiation technologies (production of track membranes by irradiation thin films of polycyanurates with subsequent chemical etching and sensitization) are described.

UDC 66.095.26

ISBN 978-966-360-477-0

CONTENTS

Chapter 6

THERMALLY STABLE NANOPOROUS CYANATE ESTER RESIN/LINEAR POLYURETHANE GRAFTED SEMI-INTERPENETRATING POLYMER NETWORKS CREATED BY IRRADIATION TECHNOLOGIES

ABBREVIATION LIST

BET — Brunauer-Emmett-Teller
CER-A — cyanate ester resins derived from DCBA
CER-E — cyanate ester resins derived from DCBE
CERs — cyanate ester resins
CML — cumulative mass loss
CRS — laser-interferometric creep rate spectroscopy
DBP — dibutyl phthalate
DCBA — dicyanate ester of bisphenol A, dicyanate monomer
DCBE — dicyanate ester of bisphenol E, dicyanate monomer
DMP — dimethyl phthalate
DMTA — dynamic mechanical thermal analysis
DOP — dioctyl phthalate
DSC — differential scanning calorimetry
EDX — energy dispersive X-ray
FTIR — Fourier transform infrared spectroscopy
IL — ionic liquid
IPNs — Interpenetrating polymer networks
LPU — linear polyurethane
NMR — nuclear magnetic resonance
PCL — poly(ε-caprolactone)
PCNs — polycyanurates, polycyanurate networks
PTFE — polytetrafluorethylene
SAXS — small-angle X-ray scattering
SEC — size-exclusion chromatography
SEM — scanning electron microscopy
TGA — thermogravimetric analysis
TMs — track-etched membranes

PREFACE

Polycyanurates, which are produced from cyanate ester resins by the high-temperature catalytic polycyclotrimerization process, represent a relatively new class of high-performance polymer matrices for high-temperature printed wiring board laminates and structural composites. Polycyanurates possess a unique combination of low dielectric loss characteristics, low water and moisture adsorption, dimensional stability, and excellent adhesion to conductive metals up to 250 °C. Unusually, the low capacitance properties of polycyanurates and associated low dissipation factors make them at the moment irreplaceable as matrix resins for applications in constructions of radomes and aircrafts with reduced radar signatures. Since the late 1970s, cyanate ester resins have been used with glass or aramid fiber in high-speed multilayer circuit boards, which remains their primary application. Polycyanurates have already flown in radomes and high gain antennae for primary and secondary structures of the High-Speed Civil Transport and Fighter Aircraft. The main drawback of such polymer matrices is the high brittleness inherent to high-crosslink-density polymer networks. To solve this problem, polycyanurates are used in combination with epoxy oligomers, engineering thermoplastics and rubbers. In 1994 the leading scientists working in the field of cyanate ester resins published the book entitled "Chemistry and Technology of Cyanate Ester Resins" edited by I. Hamerton (Glasgow: Chapman & Hall), where the most interesting and useful published information on polycyanurates synthesis, processing, modification, characterization, and properties was reviewed. That monograph has become a handbook for many scientists specializing in the field. In 2000 Nair, Mathew and Ninan published a review on the advantages in of cyanate ester resins in *Adv. Polym*. Sci.

In the early 1990s, my team started research on polycyanurates, and later colleagues from Greece, Italy, France, Great Britain *etc.* joined this research. In 2010 we published a book entitled "Thermostable Polycyanurates. Synthesis, Modification, Structure and Properties" edited by A. Fainleib (Nova Science Publishers, Inc., New York) containing the results of our studies on synthesis, modification, and characterization of polycyanurate networks, their co-networks with other monomers, interpenetrating polymer networks, and (nano) composites based on them.

Since 2010 many publications have appeared on nanocomposites based on cyanate ester resins (polycyanurates). A specific direction of research in this field is the synthesis and characterization of nanoporous polycyanurates. The present book contains the results of our studies in the framework of the international collaboration of the Institute of Macromolecular Chemistry of the National Academy of Sciences of Ukraine mainly with Institut de Chimie et des Matériaux Paris-Est from Thiais, France, and other French partners on the generation of nanoporous structure in polycyanurate films using different chemical and physical approaches and investigation of the structure-properties relationships in these new materials.

I would like to express my gratitude to my co-authors for their valuable contributions.

Alexander Fainleib

INTRODUCTION

Seven complementary methods have been developed for preparing nanoporous film systems based on thermostable polycyanurates (PCNs). Three methods were based on the modification of PCN networks by a reactive porogen (*i.e.*, poly(ε-caprolactone), PCL), which was partially chemically incorporated into the PCN network framework. Porous structures were then created either by extraction of the non-incorporated part of PCL or by partial hydrolysis of PCL, followed by removal of hydrolysis products from the system. Alternatively, thermal degradation of polyester sub-chains at 250 °C (temperature much lower than the onset temperature for degradation of the PCN matrix) also allowed for the creation of nanoporous frameworks. Furthermore, four other original methods for pore generation were developed: 1 — the synthesis of PCN networks in the presence of high-boiling-temperature liquids (phthalates), and their subsequent removal upon extraction, 2 — the synthesis of PCN networks with different degrees of conversion of cyanate groups, followed by the extraction of unreacted monomer or PCN fragments non-incorporated into the network structure, 3 — the synthesis of PCN networks in the presence of ionic liquids and their subsequent removal upon extraction, and 4 — the preparation of track-etch membranes from PCN-based films *via* irradiation by α particles, followed by an alkaline etching to reveal the tracks created after the bombing.

Novel nanoporous film thermosets were developed from PCN obtained by polycyclotrimerization of dicyanate ester of bisphenol E in the presence of hydrolytically labile poly(ε-caprolactone). During the synthesis of PCL-modified PCN networks, it was established that PCL was partially incorporated into the PCN structure. Porous frameworks were then

derived from such PCN/PCL-based hybrid networks by selective hydrolysis of a significant part of PCL sub-chains under mild conditions. The structure and properties of the precursory networks as investigated by FTIR, solid-state ^{13}C NMR, DSC, TGA, and pycnometry were compared to those of the resulting porous materials. Thermogravimetric analyses showed that the porous hybrid systems were characterized by thermal and thermal oxidative stabilities higher than those of their non-hydrolyzed homologues. The porosity of the resulting hydrolyzed networks was examined by SEM and DSC-thermoporometry: pore sizes ranging from 10 to 150 nm at most were thus determined.

The nanoporous structure was also generated in PCN/PCL hybrid networks after extraction of unreacted free PCL sub-chains, which were not chemically incorporated into the PCN crosslinked framework. Structure-property relationships for precursory and porous PCN/PCL hybrid networks were investigated using a large array of physicochemical techniques. The porosity associated with the networks after extraction was evaluated by SEM and DSC-based thermoporometry: pore sizes around 10—90 nm were determined along with pore volumes as high as about 0.3 $cm^3 \cdot g^{-1}$. Density and dielectric measurements strongly suggested the occurrence of closed pore structures. Due to their high thermal stability as investigated by TGA, nanoporous PCN/PCL hybrid crosslinked films could be considered promising materials for potential applications as thermostable membranes.

Original mesoporous PCN films were generated by polycyclotrimerization of dicyanate ester of bisphenol E in the presence of varying amounts of inert high-boiling-temperature liquids, *i.e.* dimethyl phthalate, dibutyl phthalate, or dioctyl phthalate followed by their quantitative extraction after complete formation of PCN crosslinked frameworks. The chemical structures of precursory networks and resulting porous thermosetting films were confirmed by FTIR analysis and gel fraction determination. The porosity of the latter was examined by SEM and DSC-based thermoporometry. Average pore diameters were found to be smaller than 50 nm and pore volumes as big as 0.16 $cm^3 \cdot g^{-1}$. The density of porous samples was found to be lower than that of non-porous pure PCN synthesized as a model system, thus suggesting the occurrence of closed pore structures. Moreover, the thermal properties of PCN-based films were investigated by DSC and TGA. The high-boiling-temperature liquids decreased their glass transition temperatures (T_g) and their degradation temperatures by acting as plasticizers. This plasticizing effect logically disappeared after the removal of pore-forming phthalates from the networks: the T_g values of the mesoporous films were even higher than those of non-porous neat PCN, while their thermal stability turned out to be nearly identical to that of neat PCN.

The annealing behavior and thermal stability of nanoporous film materials based on cyanate ester resins (CERs) obtained by the chemically induced

phase separation technique through the use of porogenic molecules of different sizes and concentrations were studied. Measurements were performed by the thermogravimetric analysis in dynamic and isothermal modes as well as by FTIR spectroscopy. Isothermal annealing in the temperature range from 50 to 150 °C led to mass losses observed at temperatures far below the glass transition. They were associated with the desorption of moisture and residual porogen molecules trapped in the bulk. Therefore, these processes were described by diffusion laws, and the values of the basic kinetic parameters were determined. Further, thermal-oxidative degradation took place in the glass transition temperature domain (expected between 220 and 250 °C) during isothermal annealing at 250 °C. The gas transport properties of CER films were analyzed after the different processing steps, and relationships between the material structure and the main gas transport parameters were established.

Novel nanoporous film materials of thermostable CER were generated by polycyclotrimerization of dicyanate ester of bisphenol E in the presence of varying amounts (from 20 to 40 wt%) of an ionic liquid (IL), *i.e.* 1-heptylpyridinium tetrafluoroborate, followed by its quantitative extraction after complete CER network formation. The completion of CER formation and IL extraction was assessed using gel fraction content determination, FTIR, ^{1}H NMR, and EDX. SEM and DSC-based thermoporometry analyses demonstrated the formation of nanoporous structures after IL removal from CER networks, thus showing the effective role of IL as a porogen. Pore sizes varied from ~20 to ~180 nm with an average pore diameter of around 45—60 nm depending on the initial IL content. The thermal stability of nanoporous CER-based films was investigated by thermogravimetric analysis.

A straightforward and effective method for producing nanoporous thermosetting CERs with controlled conversion of the reactive groups of cyanate monomer has been developed by varying polymerization temperature and duration of CER synthesis, followed by a simple extraction procedure. Using FTIR spectroscopy, the conversion degree ranging from about 79 to 96 % was determined. DSC-based thermoporometry and SEM analyses evidenced the generation of nanoporous structures in the crosslinked CER films produced. The pore size distribution varied from ~10 to 220 nm with an average pore diameter of within 20—45 nm, and the porosity was comprised between 2.8 and 7.4 % for all the nanoporous CERs studied. It has been established that the thermal stability of nanoporous CERs remains high enough and depends on the final conversion of cyanate groups in the partly cured CER networks.

Thermally stable nanoporous polymer films have been created as promising materials for track membranes and filters using nuclear technologies. Thermosetting CERs with 10 wt% of linear polyurethane (LPU) were combined by stepwise thermal curing, and the films of resulting hybrid polymers were irradi-

ated with α-particles followed by chemical etching. Well-defined highly regular nanoporous structures were developed in the films as evidenced by SEM. No significant changes in the chemical structure of the polymer systems obtained after α-irradiation were observed by FTIR spectroscopy measurements. The polymer films obtained from CER/LPU grafted semi-IPNs had narrow pore diameter distribution with an average pore diameters of around 12 nm. DSC and TGA measurements showed that the thermal characteristics of the nanoporous films were sufficiently high (T_g ~ 167 °C to ~199 °C $T_{d5\%}$ ~ 293—359 °C, and $T_{d\ \max}$ ~ 429—457 °C). The CER/LPU nanoporous thermosetting materials demonstrated effective gas transport properties tested with such gases as O_2, CO_2, N_2, and CH_4. The combination with an additional sensitization step using γ-rays and a longer time of chemical etching improved the properties of the nanoporous systems developed. Such materials open the way to numerous applications, for example, as ultrafiltration membranes for advanced technologies, especially under extreme conditions.

CHAPTER 1

NANOPOROUS THERMOSETS CREATED BY PARTIAL HYDROLYSIS OF POLY(ε-CAPROLACTONE) FRAGMENTS IN POLYCYANURATE-BASED HYBRID NETWORKS

1.1. Introduction

Porous polymer films are widely used in many branches of industry as membranes, adsorbents, and filters for separation, depuration or filtration, as well as low dielectric permittivity films for microelectronics [1, 2]. Numerous advanced technologies require a combination of properties for polymer films, including high thermal stability, inertness, excellent resistance toward solvents and aggressive media, etc. Polycyanurates (PCNs) represent a family of thermosetting polymers that meet such requirements, in addition to their attractive intrinsic features, *i.e.* excellent dimensional stability, high purity, low dielectric constants (2.6—3.2), inherent flame-retardancy, and high adhesion to metals and composites [3, 4]. Therefore, they constitute promising materials for producing membranes, adsorbents, and filters working under severe conditions (high temperatures, corrosive media, etc.). Porous materials based on thermostable polymers are generally prepared either through the irradiation of their thin films by ions of heavy metals, followed by a track-etching procedure [5—8], or by *in situ* synthesis of them in the presence of different porogens (for example, gases, solvents, and thermally or photochemically labile thermoplastic polymers) with further removal of the latter [9—14]. Nevertheless, forming porous PCN thermosetting films still remains a key challenge, as to the best of our knowledge, only a few reports on the design and synthesis of porous PCNs have been published so far [15—17].

Interestingly, Kiefer *et al.* [15, 16] synthesized such porous systems from dicyanate ester of bisphenol E (DCBE) using cyclohexane as a porogen. The generation of foam struc-

tures was accomplished by removing the nonreactive liquid porogen having a low boiling point upon heating. Hedrick *et al.* [17] described the synthesis of PCN systems with thermally labile fragments by polycyclotrimerization of 4,4′-(hexafluorineisopropylidene) diphenyl dicyanate in the presence of poly(propylene oxide) or propylene oxide-urethane copolymer. The propylene oxide-based oligomers were molecularly miscible with the cyanate monomer over the entire range of compositions studied but developed a two-phase structure upon the reaction to form a thermoplastic modified PCN thermoset. Upon thermolysis of the propylene oxide segments, the foam generated was found to collapse, which might be related to an increase of polymer chain mobility in the PCN network at temperatures close to T_g. Accordingly, it is obvious that detailed studies on porous thermosets derived from PCNs remain scarce. In this context, we have undertaken a thorough investigation of the scope and limitations associated with the use of miscellaneous PCN systems for the design of (meso)porous crosslinked film materials. One of our groups has reported several works on the modification of PCNs with telechelic thermoplastic polymers [18—24], and we have recently broadened this family of modified PCN networks through the synthesis and characterization of the PCN/PCL systems [25]. Herein, we propose an alternative route to porous PCN networks without using high temperatures, where hybrid networks can be effectively employed as precursors. Indeed, under mild hydrolytic conditions, the hydrolyzable PCL segments can be selectively removed, thus playing the role of porogens.

The present chapter is essentially concerned with the preparation of such porous PCN networks and their characterization by different physicochemical techniques, namely Fourier transform infrared (FTIR) spectroscopy, solid-state Carbon-13 nuclear magnetic resonance (^{13}C NMR), differential scanning calorimetry (DSC), thermogravimetric analysis (TGA), and pycnometry. The potentialities afforded by the envisioned approach are addressed, and we particularly focus our attention on the correlations between the structure and properties of the precursory networks and those of the resulting porous materials, as well as their morphology as examined by scanning electron microscopy (SEM) and DSC-based thermoporometry.

1.2. Synthesis and generation of porous thermosetting materials

The PCN(DCBE)/PCL mass compositions ranged from 95/5 to 50/50 wt%, and the two neat partners were also considered. The systems prepared were step-by-step cured in the temperature range 150—210 °C, and the resulting film thickness was in the range of 45—60 μm [26]. The films

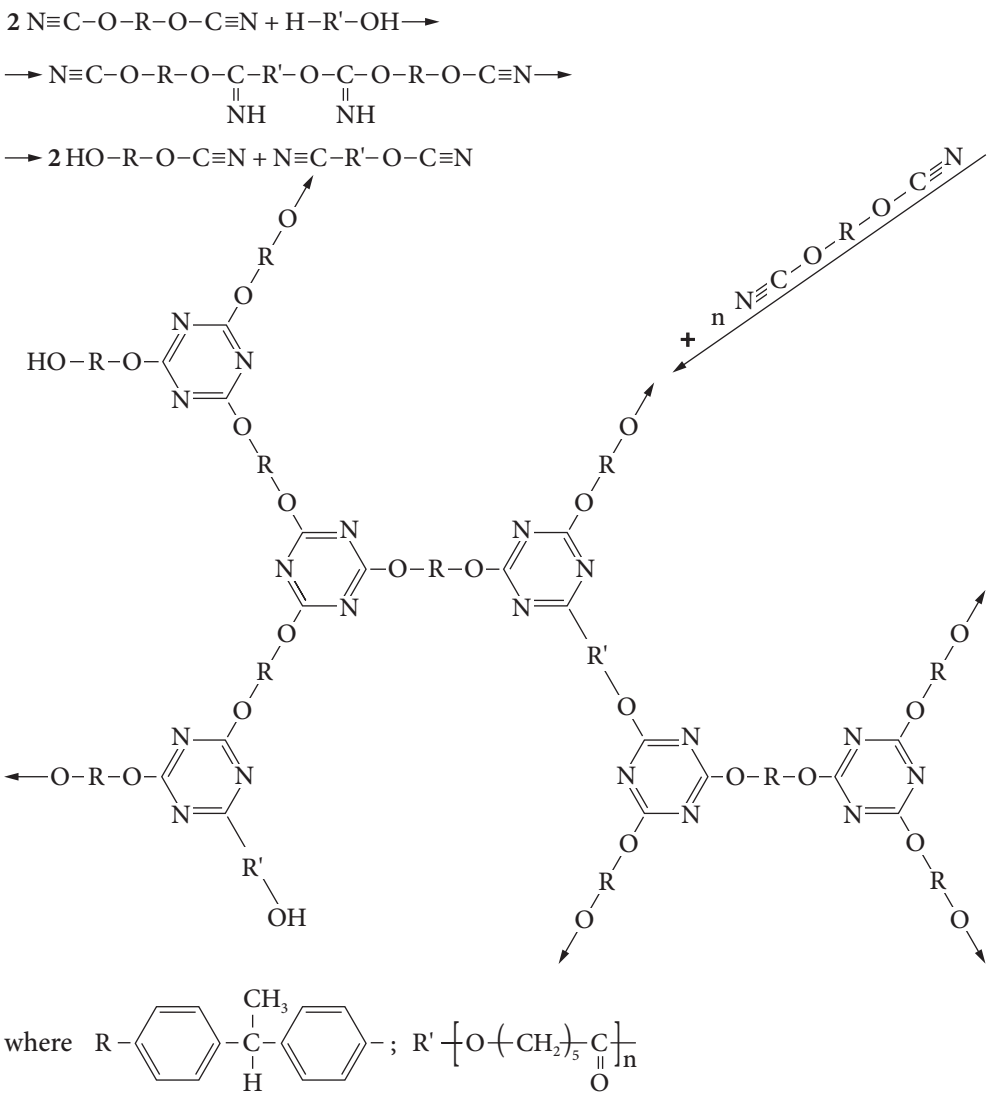

Fig. 1.1. Scheme of chemical incorporation of dihydroxy-telechelic PCL into PCN structure

of PCN/PCL networks were immersed in a 50/50 vol.% mixture of phosphate buffer solution ($5 \cdot 10^{-2}$ mol $\cdot L^{-1}$ KH_2PO_4, $4.9 \cdot 10^{-2}$ mol $\cdot L^{-1}$ NaOH, pH = 8.2)/ethanol and maintained for 15 days at 70 °C. The samples were then rinsed with distilled water up to neutral pH and dried to constant weight under vacuum at 60 °C.

Some time ago we demonstrated [18—24] that the *in situ* synthesis of PCN networks in the presence of thermoplastic modifiers, such as polyesters and polyurethanes, led to the formation of the so-called hybrid networks. In fact,

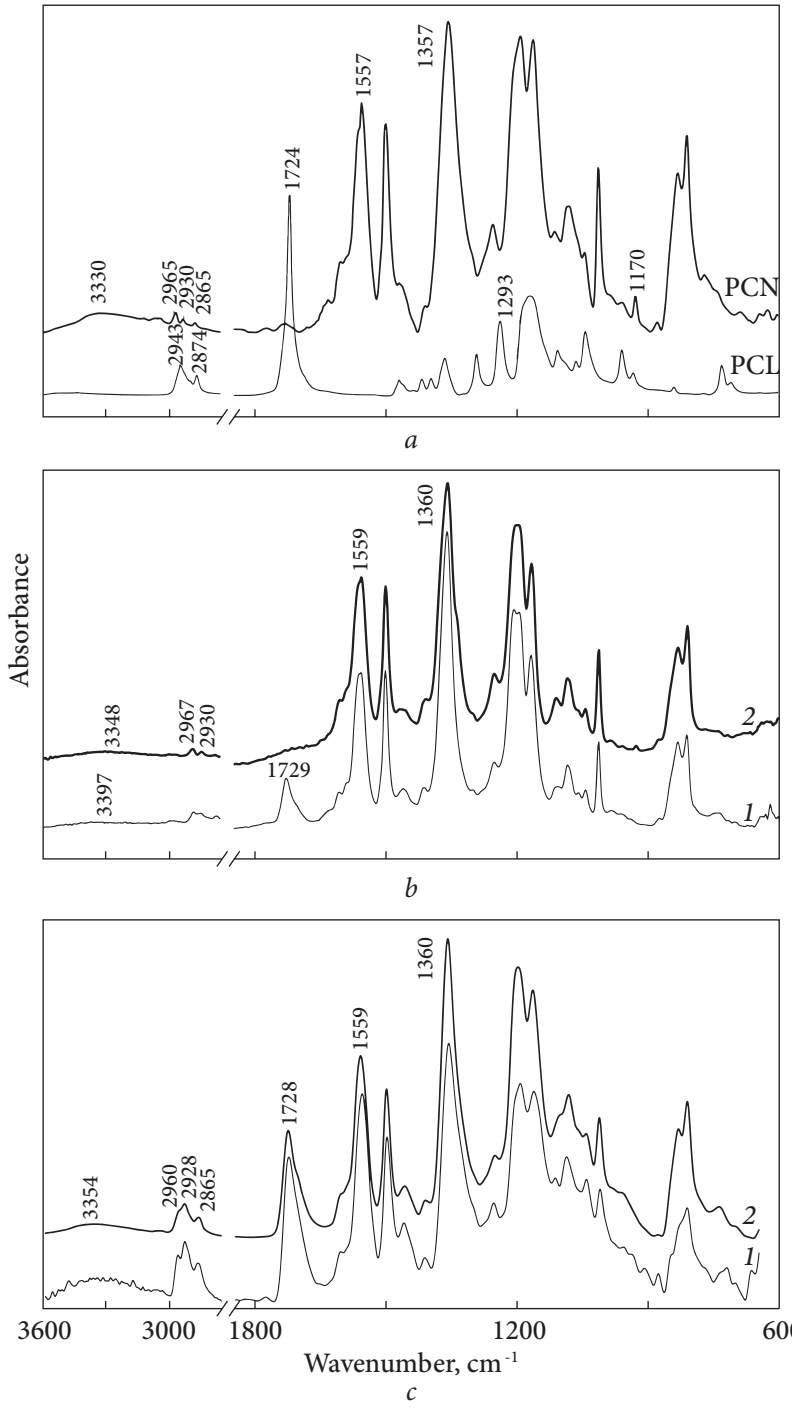

Fig. 1.2. FTIR spectra of *a* — pure PCN network, PCL oligomer, and PCN/PCL samples with an initial PCL content of *b* — 30 wt% and *c* — 50 wt%: *1* — before hydrolysis, *2* — after hydrolysis

the aforementioned reactive modifiers were partly chemically incorporated into the network structure through the condensation reaction of their terminal hydroxyl or urethane groups with cyanate (—O—C≡N) functions of the growing PCN network. In our previous work [25], we have investigated the structure and properties of PCN/PCL hybrid networks derived from DCBE and a dihydroxy-telechelic oligomer of PCL. Fig. 1.1 shows the process of chemical incorporation of PCL oligomeric sub-chains into the PCN structure during the polycyclotrimerization reaction of dicyanate monomer (DCBE) in the presence of one such reactive oligomer.

FTIR spectra of the pure PCN network, PCL oligomer, and two representative PCN/PCL samples are presented in Fig. 1.2. In the spectra of the pure PCN and PCN/PCL networks, the absence of strong absorption bands at 2272—2236 cm^{-1} corresponding to C≡N stretching vibrations from O—C≡N groups [3], along with the appearance of strong absorption bands at 1358 and 1557 cm^{-1} associated with the stretching vibrations of cyanurate rings (C=N in triazine and phenyl-oxygen-triazine, respectively), clearly indicated the completion of the DCBE polymerization process. Moreover, the occurrence of the strong carbonyl absorption band at 1729 cm^{-1} in the FTIR spectra of all PCN/PCL samples confirmed the presence of PCL sub-chains. Nevertheless, the absence of the absorption band at 1293 cm^{-1} arising from C—O and C—C stretching vibrations of PCL crystallites [27, 28], revealed that PCL fragments did not crystallize within the PCN network. In these systems, PCL sub-chains are either covalently incorporated within the PCN network or constrained within the matrix (free PCL oligomers), preventing any PCL crystallization [25].

The advantage of the hydrolytic degradability of PCL was taken to produce porous PCN-based networks through the selective hydrolysis of PCL sub-chains from PCN/PCL hybrid systems. This hydrolysis was conducted at 70 °C under mild conditions, namely by using a mixture of phosphate buffer and ethanol. We adopted similar experimental conditions to those utilized elsewhere for the partial degradation of oligoester-derivatized networks [29]. Under the basic conditions chosen, it was checked by FTIR and gravimetry that the pure PCN network was unaffected after 15 days. In contrast, the PCL oligomer was completely degraded as expected. According to the mass loss values determined for PCN/PCL networks after hydrolysis, the PCL degradation process was not quantitative, and the degree of hydrolyzed PCL was lower than 60 wt%, regardless of the initial PCL content (Table 1.1). These results suggest that PCL segments are difficult to access within the PCN network, thus illustrating its protective role.

Thus, after partial hydrolysis of PCL, FTIR spectra of PCN/PCL systems still displayed the presence of the characteristic bands associated with PCL segments, even though a significant decrease in their intensity was noticed (Fig.1.2*b*, *c*).

Moreover, proton nuclear magnetic resonance (^{1}H NMR) and size-exclusion chromatography (SEC) analyses of degradation products gave evidence that not only the PCL oligomer but also smaller fragments of oligo(ε-caprolactone) ($M_n \sim 300$ g · mol^{-1} $M_w/M_n \sim 1.5$), and 6-hydroxyhexanoic acid were removed [26].

Fig. 1.3 depicts the solid-state ^{13}C NMR spectra of the PCN/PCL system characterized by an initial PCL content of 30 wt%, before and after hydrolysis. For the sake of comparison, the ^{13}C NMR spectra of the neat PCN network and PCL oligomer were recorded under the same experimental conditions.

The assignments of the ^{13}C NMR lines in Fig. 1.3 are in agreement with those reported in the literature [30—32]. The ^{13}C NMR peaks of the spectrum associated with the pure PCN network (Fig. 1.3*a*) are rather broad, as expected for a polymer system in the glassy state. For the semi-crystalline PCL homopolymer at room temperature, the ^{1}H-^{13}C dipolar couplings for the carbons in the crystalline regions are higher than those in the amorphous domains. In addition, the ^{1}H spin-lattice relaxation signal in the rotating frame is not monoexponential and may be described by two $T1_p(^1H)$ components [32]. The fast (slow) relaxing component is related to a dominant amount of amorphous (crystalline) domains. For both reasons, the ^{1}H → ^{13}C CP efficiency is much higher for the PCL carbons in the crystalline regions. Thus, the ^{13}C NMR spectrum recorded on the neat PCL (Fig. 1.3*b*) with a crystallinity of 51 % could mainly result from the contributions of the carbons involved in the crystalline

Table 1.1. **Characteristics of PCN/PCL networks after hydrolysis** [a]

Initial PCL content in PCN/PCL samples w_i, wt%	Mass loss Δm [b], wt%	Degree of hydrolyzed PCL w_h^c, wt%	PCL content in PCN/PCL samples after hydrolysis w_f^d, wt%
0	0	—	—
5	<1	<20	~4
10	4	40	6
15	6	40	9
20	11	55	10
30	18	60	15
40	22	56	23
50	17	34	40
100	100	100	0

[a] Hydrolysis conditions: phosphate buffer/ethanol 50/50 vol.%, T = 70 °C, t = 15 days; [b] $\Delta m = (m_0 - m_d) / m_0 \cdot 100$, where m_0 and m_d stand for the initial mass of the sample and the mass of the residual network after vacuum drying, respectively; [c] $w_h = \Delta m / w_i \cdot 100$; [d] $w_f = (w_i - \Delta m) / (w_{PCN} + w_i - \Delta m) \cdot 100$, where w_{PCN} stands for the initial PCN content.

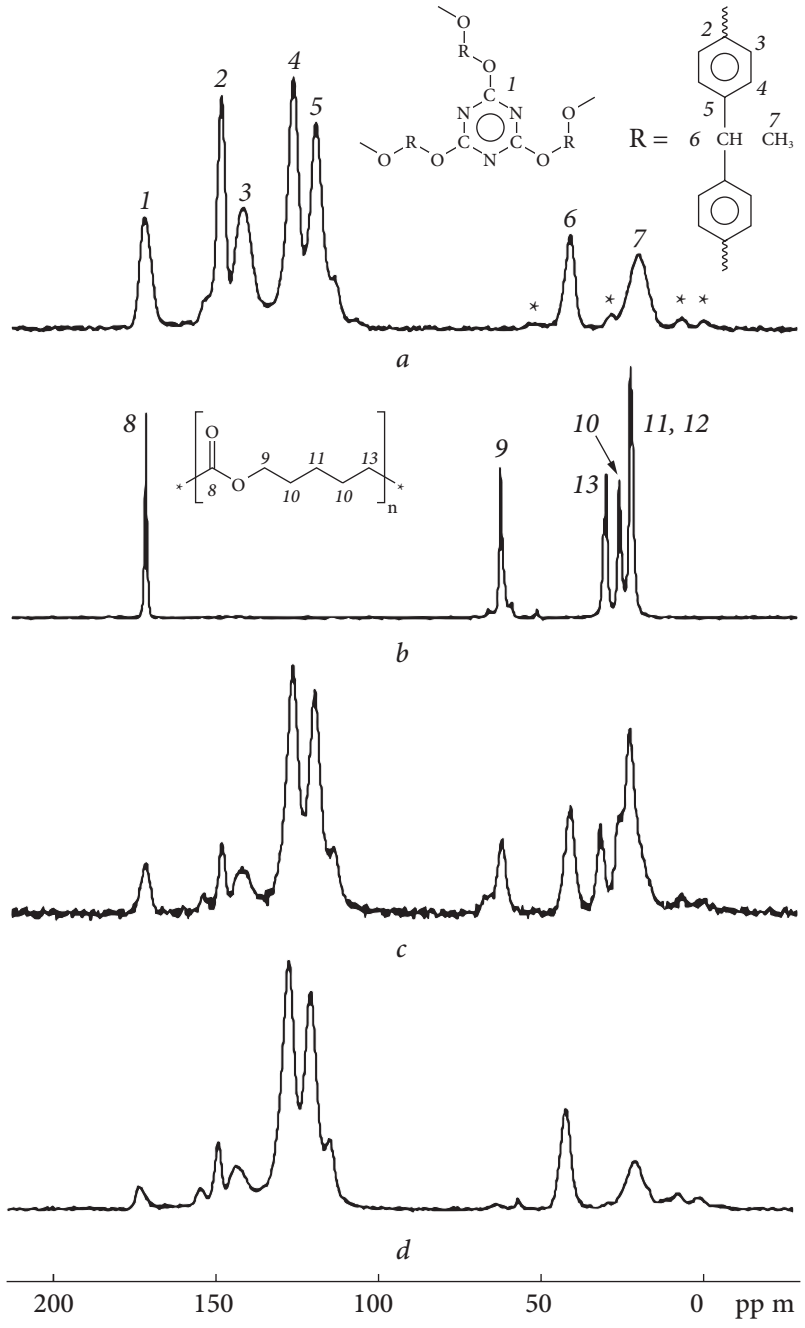

Fig. 1.3. ^{13}C CP/MAS/DD spectra of (*a*) pure PCN network, (*b*) PCL oligomer, PCN/PCL 70/30 wt% hybrid network (*c*) before and (*d*) after hydrolysis. The asterisks stand for the first-order spinning side bands

regions, and this feature might well account for the relatively low line width of the peaks observed.

The peaks observed on both the PCN network and PCL oligomer spectra were also detected on the ^{13}C CP/MAS/DD NMR spectrum recorded for the PCN/PCL (70/30 wt%) system. The line at 64.0 ppm, related to the carbons from —OCH_2— groups of the PCL monomeric unit, does not superimpose with any contribution from the PCN component. It is worth remarking that this peak displays a stronger broadening by comparison with that obtained in the spectrum of the neat PCL. This broadening is somehow consistent with the absence of PCL crystallization within the PCN network, as revealed by FTIR [26].

Let us now consider the ^{13}C CP/MAS/DD NMR spectrum of the corresponding PCN/PCL system after hydrolysis. The intensity of the ^{13}C NMR peak at 64 ppm, characteristic for the PCL component, was significantly reduced, suggesting that most of PCL oligomers had been removed during the hydrolysis. The same result was also obtained by considering the ^{13}C MAS/DD NMR spectra recorded during ^{13}C direct polarization experiments, which confirmed that a great proportion of the PCL component was indeed extracted from the network after hydrolysis [26].

1.3. DSC investigation

The solid-state arrangement of the PCN/PCL systems was investigated by DSC [26]. Fig. 1.4 shows the DSC traces for the PCL oligomer, pure PCN, and PCN/PCL sample with 30 wt% of PCL before and after hydrolysis; their main thermal characteristics are summarized in Table 1.2.

As shown, the DSC thermogram of the neat PCL exhibits the typical behaviour of a semi-crystalline polymer with the occurrence of a well-defined glass transition temperature (T_g) at –66 °C and an intensive endothermic peak with a maximum at melting temperature T_m = 49 °C resulted from the melting of PCL crystallites.

On the other hand, the pure PCN network is an amorphous polymer with a T_g onset at 219 °C and a fairly narrow T_g range (ΔT_g) of 34 °C. Interestingly, no endothermic peak is observed in the thermograms of PCN/PCL systems, thus corroborating the conclusions inferred from the FTIR and solid-state NMR spectra: the presence of the PCN network prevents the crystallization of both chemically incorporated and unreacted free PCL oligomers. Furthermore, single glass transitions were detected for PCL contents varying from 5 to 50 wt%.

As a matter of fact, the presence of PCL as a low-T_g component in the hybrid networks generally caused both a shift of T_g toward lower values and a widening of ΔT_g, as well as an increase in the heat capacity jump (ΔC_p), compared to

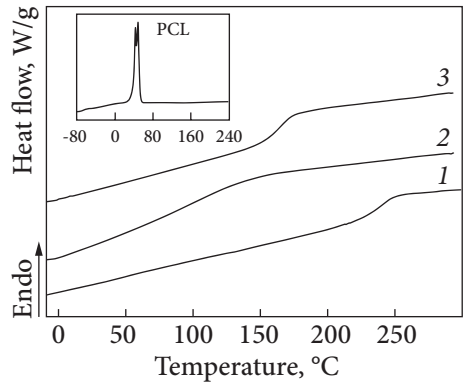

Fig. 1.4. Typical DSC thermograms (second heating scan) for PCL oligomer, (*1*) pure PCN network and PCN/PCL hybrid network with a PCL content of 30 wt% (*2*) before and (*3*) after hydrolysis. The DSC traces are shifted vertically for the sake of clarity

Table 1.2. **DSC data for PCN/PCL systems before and after hydrolysis**

System	PCL content, wt%	$T_{g,onset}$ [a], °C	ΔT_g [b], °C	ΔC_p [c], J · g^{-1} · °C^{-1}
PCN	0	219	34	0.29
PCN/PCL				
before hydrolysis	30.0	79	51	0.85
after hydrolysis	14.6	150	26	0.36
PCL[d]	100	–66	17	0.05

[a] $T_{g,onset}$: value associated with the intercept of the tangent to the midpoint of the specific heat increment with glassy baseline; [b] $\Delta T_g = T_{g,end} - T_{g,onset}$: width of glass transition temperatures, where $T_{g,end}$ is associated with the intercept of the tangent to midpoint of specific heat increment with the viscous baseline; [c] $\Delta C_p = C_{p,v} - C_{p,g}$: heat capacity jump at T_g, where C_p is the heat capacity, and the subscripts *v* and *g* refer to the viscous and glassy states, respectively; [d] thermal characteristics of PCL oligomer: T_m = 49 °C, ΔH_m = 72 J × × g^{-1}, degree of crystallinity: X_c = 51%; X_c is equal to ΔH_m / ΔH_{m0} × 100, where ΔH_m and ΔH_{m0} correspond to the melting enthalpy of PCL oligomer and 100 % crystalline PCL sample, respectively (ΔH_{m0} = 142 J × g^{-1} [33]).

the situation found for pure PCN. Such a broadening of T_g is consistent with the noticeable extent of structural heterogeneity in the PCN/PCL networks, as previously evidenced by dynamic mechanical thermal analysis (DMTA) [25]. After partial hydrolysis of the PCL fragments from PCN/PCL hybrid networks, the $T_{g,onset}$ dramatically increased and ΔT_g narrowed, due to the removal of substantial amounts of PCL. Even though the T_g ranges were quite close to that determined for pure PCN, the T_g values were significantly lower than the corresponding one for the latter network. This strongly suggests that the residual PCL sub-chains in the hydrolyzed networks were chemically incorporated and, on the contrary, most of the PCL sub-chains hydrolyzed were not covalently attached to the precursory network.

Tabl. 1.3. **Thermal properties of PCN/PCL systems before and after hydrolysis as investigated by TGA**

PCN/PCL composition (wt%)	T_{d1}^{a}, °C	T_{d2}^{a}, °C	T_{d3}^{a}, °C	$T_{d(5\%)}$, °C	$T_{d(50\%)}$, °C	m_1^{d}, wt%	m_2^{d}, wt%	m_3^{d}, wt%	$m_{char.}^{e}$, wt%
Thermal degradation (N_2)									
100/0	—	427	—	411	698	—	17	—	46
70/30 (before hydrolysis)	299	409	—	268	411	11	48	—	20
85/15 (after hydrolysis)	309	431	536	267	548	9	33	51	42
85/15 (before hydrolysis)	—	419	—	384	441	—	30	—	33
0/100	284	393	—	280	381	6	67	—	2
Thermal oxidative degradation (O_2)									
100/0	—	420	540	406	518	—	19	69	0.2
70/30 (before hydrolysis)	328	383	518	253	386	17	47	87	0.1
85.4/14.6 (after hydrolysis)	279	374	484	230	426	8	30	73	0.6
85/15 (before hydrolysis)	—	412	529	380	437	—	31	76	0.4
0/100	275	327	461	220	270	56	91	98	0.3

[a] T_{di}: temperature of maximum degradation rate for stage i considered; [b] $T_{d(5\%)}$: temperature for a 5 % mass loss; [c] $T_{d(50\%)}$: temperature value for a 50 % mass loss; [d] m_i: mass loss at degradation temperature T_{di}; [e] m_{char}: mass corresponding to char residue.

1.4. Thermal stability by thermogravimetric analysis

Fig. 1.5 displays typical TGA curves of mass loss for different PCN/PCL systems, before and after hydrolysis, during thermal (under a nitrogen atmosphere) and thermal-oxidative (under an oxygen atmosphere) degradation. The main thermal characteristics of the samples studied are listed in Table 1.3. The peculiarities of thermal stability of PCN/PCL precursors depending on the PCL content have recently been investigated in detail [25]. Also, we have analyzed the influence of hydrolysis on the thermal behavio r of PCN/PCL hybrid networks [26].

An inspection of the data for the 30 wt% PCL-containing system clearly showed that the thermal stability under oxygen was lower than that under nitrogen, due to the occurrence of oxidation in the former case. Besides, both the thermal and thermal-oxidative stabilities in the precursor and in the resulting network after hydrolysis were lower than that of the neat PCN network. Nevertheless, such stabilities were significantly higher than those for pure PCL, and the hybrid networks could be considered thermally stable polymers. After partial removal of PCL fragments through hydrolysis, the thermal stability of the residual network was logically higher than that of the precursory network: the partially hydrolyzed sample displayed higher values of temperature degradation for the first two stages (T_{d1} and T_{d2}) and for a 50% mass loss ($T_{d\,(50\%)}$), and correspondingly lower values of mass loss m_1 and m_2, as well as a higher value of the char residue. Interestingly, the T_{d2} value (431 °C, N_2 atmosphere) for the hydrolyzed network with a residual

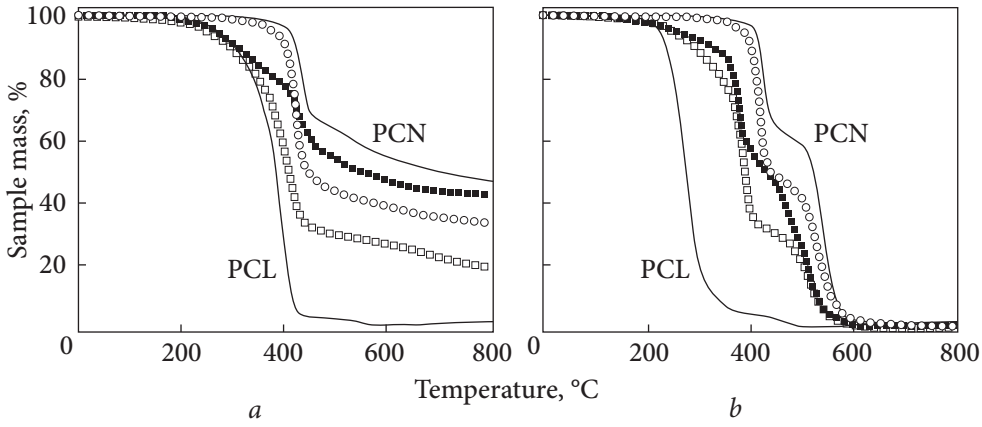

Fig. 1.5. Mass loss curves from TGA for PCL oligomer, pure PCN network, and PCN/PCL hybrid networks with a PCL content of (○) 15 wt% before hydrolysis, and 30 wt% (□) before and (■) after hydrolysis: *a* — nitrogen atmosphere, *b* — oxygen atmosphere

PCL content of 14.6 wt% was close to that determined for pure PCN and higher than that found (419 °C, N_2 atmosphere) for the homolog network non-subjected to hydrolysis with a close PCL content (15 wt%).

1.5. Morphological analysis of porous networks

The morphologies of PCN-based networks, before and after hydrolysis, were examined by SEM (Fig. 1.6) [26]. Regardless of the initial PCL content, the non-degraded samples displayed compact and non-porous structures.

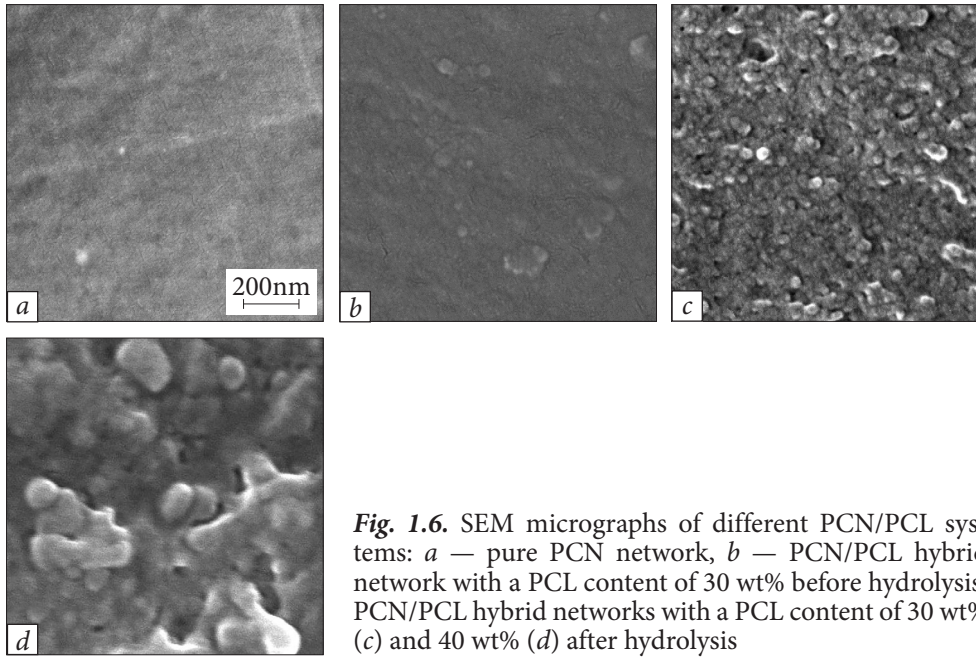

Fig. 1.6. SEM micrographs of different PCN/PCL systems: *a* — pure PCN network, *b* — PCN/PCL hybrid network with a PCL content of 30 wt% before hydrolysis, PCN/PCL hybrid networks with a PCL content of 30 wt% (*c*) and 40 wt% (*d*) after hydrolysis

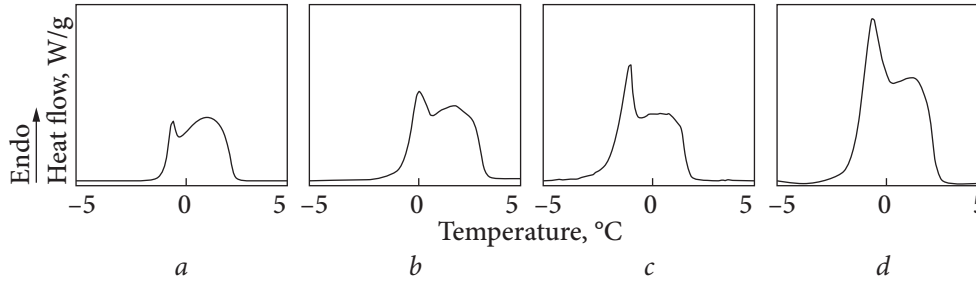

Fig. 1.7. DSC melting thermograms of water associated with porous samples from PCN/PCL hybrid networks with different compositions (wt%): *a* — 95/5, *b* — 90/10, *c* — 80/20, and *d* — 70/30

Table 1.4. **Pore diameters of porous networks as determined by SEM and DSC-based thermoporometry after hydrolysis of PCN/PCL systems**[a]

Initial PCN/PCL composition	D_p, nm		Initial PCN/PCL composition	D_p, nm	
	SEM[b]	DSC-thermoporometry[c]		SEM[b]	DSC-thermoporometry[c]
5 / 95	—	25—65	30 / 70	10—100	20—120
10 / 90	20—50	20—80	40 / 60	20—100	20—100
15 / 85	—	25—80	50 /50	15—150	15—120
20 / 80	15—100	15—115			

[a] Hydrolysis conditions: phosphate buffer/ethanol 50/50 vol.%, T = 70 °C, t = 15 days; [b] calculated from SEM; [c] calculated from DSC-thermoporometry analysis.

The pure PCN network, after undergoing the hydrolysis conditions aforementioned, did not exhibit any pore either, indicating a high compacity in this type of network. After partial PCL hydrolysis from the PCN/PCL hybrid systems (15 days), the residual networks revealed porous structures with pore diameters (D_p) ranging from 10 to 150 nm, depending on the PCN/PCL composition. Pore sizes generally increased and pore size distributions (dV/dR) widened with increasing the PCL content (Table 1.4).

1.6. DSC-based thermoporometry

Although SEM is a common and easy tool to observe porous materials, it is not a very precise technique to determine pore sizes smaller than a few tens of nanometers. Accordingly, we resorted to an alternative technique, namely DSC-based thermoporometry [26], which is a quantitative and sensitive technique allowing for the precise determination of pore size distributions in a wide array of (meso)porous materials, provided pore diameters are smaller than 200—300 nm. It relies on the melting temperature (T_m) depression and the Gibbs-Thompson effect shown by a solvent constrained within the pores [34—37]. When applying thermoporometry through DSC measurements using water as the penetrant solvent to the porous networks under study, we detected two endothermic peaks, i.e. one related to the melting of bulk water with a maximum around 1 °C and a second one, not fully resolved, at lower temperatures arising from the melting of water confined within the pores (Fig. 1.7).

Pore size distributions are plotted in Fig. 1.8 and the corresponding pore diameter ranges are listed in Table 1.4. Whatever the PCL content, fairly narrow pore size distributions were obtained. In addition, a higher

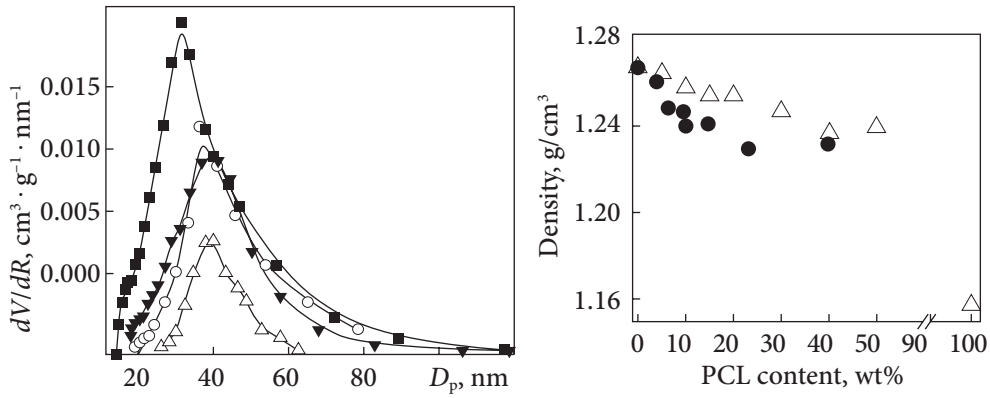

Fig. 1.8. Pore size distribution profiles of porous samples as determined by DSC-based thermoporometry for PCN/PCL hybrid networks with different compositions (wt%): (△) 95/5, (○) 90/10, (▼) 80/20, (■) 70/30

Fig. 1.9. Dependence of density on PCL content for hybrid PCN/PCL networks: (△) before and (●) after hydrolysis

PCL content in the hybrid networks was generally associated with an increase in the peak intensity in the dV/dR vs. D_p curves, in agreement with the increase in the peak intensity due to the melting of confined water in the DSC thermograms. This indicates the presence of higher pore volumes in the residual porous networks with increasing PCL contents in the hybrid precursors. Due to the high hydrophobicity of the PCN matrix, one cannot discard that water does not probe all the pores of the analyzed samples. Nevertheless, the results of for pore sizes determined by thermoporometry match those obtained from SEM, thus illustrating the reliability and complementarity of both techniques.

1.7. Density measurements on porous networks

Fig. 1.9 displays the composition dependence of the density for hybrid PCN/PCL systems before and after hydrolysis. After partially removing PCL segments from hybrid networks, the density slightly decreased. Such a decrease might account for the formation of closed pore structures. Indeed, if the residual networks after hydrolysis were constituted of interconnected open pores, their density values would be equal or close to those of non-hydrolyzed networks with the corresponding compositions. The conclusion drawn from the density measurements is supported by SEM analyses (cf. Fig. 1.6), in spite of their qualitative character.

1.8. Conclusions

This study has expanded the scope of the use of PCN-based networks as nanostructured precursors to (meso)porous thermosets. Novel nanoporous films have been prepared from thermostable PCN/PCL-based hybrid networks synthesized by polycyclotrimerization of DCBE in the presence of dihydroxytelechelic PCL. As a matter of fact, the advantage of the hydrolytic degradability of PCL is taken to generate porous networks through the selective hydrolysis of a significant part of PCL sub-chains from PCN/PCL hybrid systems. Interestingly, TGA analyses have shown that the porous hybrid systems can still be considered thermally stable polymers, and they are characterized by thermal and thermal-oxidative stabilities higher than those of non-hydrolyzed homologues with similar compositions. The porous thermosetting films display quite narrow pore size distributions with pore diameters ranging from 10 to 150 nm at most. The development of more efficient pore-generation methods is currently in progress. Novel nanoporous PCN films may find miscellaneous applications, and especially in membrane technologies requiring polymeric materials with high thermal and dimensional stability.

CHAPTER 2

NANOPOROUS POLYCYANURATE/POLY-(ε-CAPROLACTONE) HYBRID NETWORKS GENERATED USING NON-INCORPORATED POLY(ε-CAPROLACTONE) AS A POROGEN

2.1. Introduction

In Chapter 1 we have reported a novel approach to porous PCN frameworks via the selective hydrolysis of PCL sub-chains from PCN/PCL hybrid networks. During the synthesis of PCL-modified PCN networks, it was established that PCL oligomers were partially incorporated into the PCN crosslinked structure through the condensation reaction of their terminal hydroxyl groups with cyanate functions of the growing PCN network. Porous frameworks were then derived from such PCN/PCL-based hybrid networks by alkaline hydrolysis of a significant part of PCL sub-chains under mild conditions.

As PCL oligomers are partly chemically incorporated into the network structure, the question that arises is whether (nano)pores can be generated due to the removal of the non-incorporated part of PCL without resorting to the hydrolysis of PCL fragments. In this context, the present chapter focuses on an alternative and easier route toward nanoporous PCN-based films through the mere extraction of unreacted free PCL in PCN/PCL hybrid networks.

The potentialities offered by this straightforward and effective approach are addressed: in particular, we report the correlations between the structure and properties of the precursory hybrid networks and those of the resulting porous systems as investigated by various physicochemical techniques, as well as the pore morphology as evaluated through SEM, DSC-based thermoporometry, as well as density and dielectric measurements.

The PCN/PCL hybrid networks were synthesized as described in Chapter 1.

2.2. Generation of porous structure in PCN-based films

For the generation of porous structures, PCN/PCL films were extracted with acetone using a Soxhlet apparatus for 16 h and then dried under vacuum. The degree of PCL incorporation into the network was calculated based on suggestions that (*i*) 98.7 wt% of DCBE participated in network formation and 1.3 wt% of DCBE is extracted from the PCN network (gel fraction of pure PCN network was found to be 98.7 wt%), and (*ii*) unreacted (free, non-incorporated into the network structure) PCL is completely extracted from the system.

The experimental values of gel fractions, $w_{g(t)}$, were determined as the insoluble contents of completely extracted samples using the equation:

$$w_{g(e)}\,(\text{wt\%}) = \frac{m_2}{m_1} \times 100\,, \tag{2.1}$$

where m_1 and m_2 stand for the mass of dried samples before and after extraction, respectively.

The theoretical values of gel fractions, $w_{g(t)}$, were calculated considering the hypothesis that no PCL sub-chains were covalently linked to the PCN network structure by using the equation:

$$w_{g(t)}\,(\text{wt\%}) = w_{g(e)PCN} - w_{PCL}\,, \tag{2.2}$$

where $w_{g(e)\,PCN}$ and w_{PCL} stand for the experimental values of gel fraction for pure PCN (98.7 wt%) and the PCL content in the initial DCBE/PCL mass composition, respectively.

The content of PCL (α_{PCL}) chemically incorporated into PCN/PCL hybrid networks, namely the PCL mass percentage in the hybrid networks after extraction, was calculated using the equation:

$$\alpha_{PCL}\,(\text{wt\%}) = \frac{w_{g(e)} - w_{g(t)}}{w_{g(e)}} \times 100\,, \tag{2.3}$$

The PCL incorporation degree (β_{PCL}) was calculated as the fraction of chemically incorporated PCL compared to the initial mass fraction of PCL in the system after extraction using the equation:

$$\beta_{PCL}\,(\text{wt\%}) = \frac{w_{g(e)} - w_{g(t)}}{w_{PCL}} \times 100\,, \tag{2.4}$$

In previous reports [23, 25, 38], it has been demonstrated that dihydroxy-telechelic polyesters are able to react with dicyanate esters during their poly-

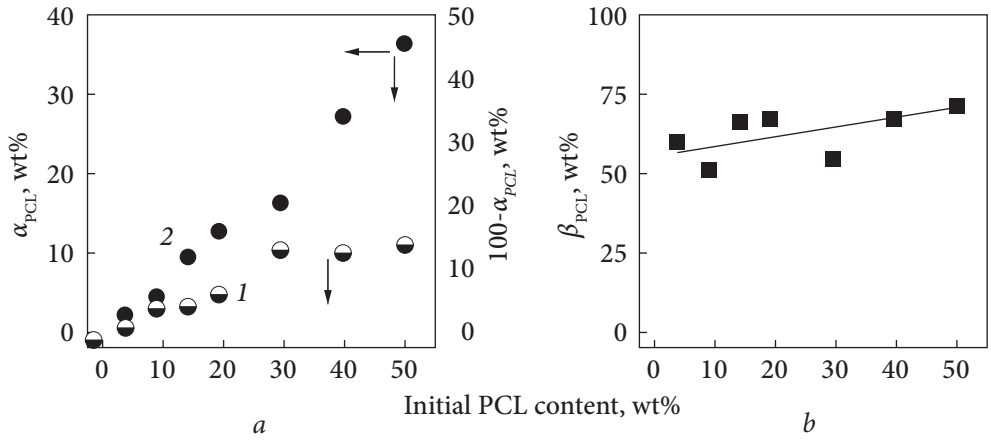

Fig. 2.1. Dependence of (*a*) contents of: *1* — non-incorporated PCL (w_{PCL} — α_{PCL}); *2* — chemically incorporated PCL (α_{PCL}) and (*b*) PCL incorporation degree (β_{PCL}) on the initial PCL content in PCN/PCL hybrid networks

Table 2.1. **Characteristics of PCN/PCL hybrid networks before and after extraction**

PCN/PCL hybrid network before extraction			PCN/PCL hybrid network after extraction			
Composition, wt%	Density[a], g · cm^{-3}	Gel fraction content[b], wt%	Composition[c], wt%	Density[a], g · cm^{-3}	Porosity (*P*)	
					Experimental	Theoretical[d]
100 / 0	1.266	98.7	100/ 0	1.258	0.05	0.01
95 / 5	1.261	97.9	97 / 3	1.246	0.06	0.02
90 / 10	1.257	94.9	95 / 5	1.248	0.07	0.06
85 / 15	1.255	94.3	90 / 10	1.243	0.09	0.06
80 / 20	1.250	92.1	87 / 13	1.246	0.11	0.09
70 / 30	1.249	83.8	84 / 16	1.238	0.13	0.17
60 / 40	1.243	82.1	73 / 27	1.232	0.16	0.19
50 / 50	1.233	77.7	64 / 36	1.223	0.15	0.24
0 / 100	1.158	0	—	—	—	—

[a] True density determined by Archimedes' balance method; [b] See Eq. 2.1 for calculation; [c] See Eq. 2.3 for calculation; [d] Theoretical *P* values calculated taking into account the volume fraction released by the uncrosslinked polymer extracted from the network.

cyclotrimerization through the reaction of hydroxyl end groups with cyanate functions of the growing PCN network. The sol-gel analysis is a good method for investigating the reactivity of PCL in the dicyanate ester/PCL systems. The extent of PCL chemical incorporation into PCN structures was established by comparison of experimental and theoretical values of gel fraction contents

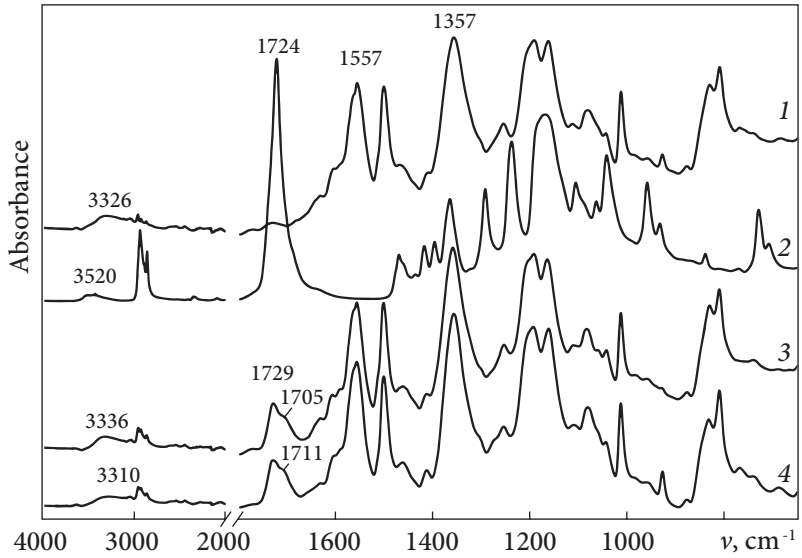

Fig. 2.2. FTIR spectra of (*1*) pure PCN, (*2*) PCL oligomer, and PCN/PCL samples with an initial PCL content of 20 wt% (*3*) before and (*4*) after partial extraction of PCL

(Eqs. 2.3 and 2.4). As illustrated in Table 2.1 and Fig. 2.1 regardless of the initial PCN/PCL composition, the experimental value of gel fraction was higher than that calculated. Moreover, the higher the PCL content in the initial composition, the greater the difference between experimental and theoretical values. These results confirm that a significant part of PCL was covalently linked to the PCN network structure and so could not be extracted from the system.

The chemical reactions running during PCN/PCL hybrid network synthesis are detailed in Section 1.1 (Fig. 1.1) [25]. Due to the rapid decomposition of the intermediate product, namely iminocarbonate (IC), a specific band of one such a product could not be observed by FTIR. The specific character of the subsequent reaction of the IC into the triazine ring consists in the possibility of the exchange of hydroxyl and cyanate groups between the reacting units [1]. Grigat and Putter [39] observed that the most acidic phenol was released, and consequently, a substituting triazine ring should be obtained with the release of the monophenol from DCBE (MCBE). In the case of such an exchange, the oligomeric dicyanate (ODC) derived from PCL had to be obtained simultaneously. Thus, three kinds of cyanate molecules, *i.e.* DCBE, MCBE, and ODC (formed from IC) participate in the cyanurate-containing network formation.

In our previous work, described in Section 1.1 the pore generation in PCN/PCL films was carried out by partial hydrolysis of PCL fragments under mild

alkaline conditions [26]. In order to develop an easier and faster route, we decided to take advantage of the simple acetone extraction used in the sol-gel analysis of PCN/PCL hybrid networks to investigate the plausible porosity created due to the removal of unreacted PCL. We assume that free PCL oligomers are totally removed as acetone is an excellent solvent of PCL, and the Soxhlet extraction is fulfilled up to constant mass for each sample (generally reached within 16 h). It is noteworthy that the chemically incorporated PCL segments cannot be degraded during the extraction process, thus not contributing to the creation of porosity.

Analyses of sol fractions associated with PCN/PCL samples after PCL extraction by acetone were performed using ^{1}H NMR and SEC techniques. It was found that in the extraction process, pure PCL macromolecules (M_n ~ 2 100 g × × mol^{-1} M_w/M_n ~ 2.03) were mainly removed from the samples. Additionally, some minor amounts of polymers with M_n ~7 800 g · mol^{-1} were detected. According to ^{1}H NMR spectra (not shown here), these soluble polymers arise from the chemical reaction of PCL with cyanurate-containing pre-polymers.

FTIR spectra of the pure PCN network, PCL oligomer, and a typical PCN/PCL hybrid network before and after extraction are shown in Fig. 2.2.

The correlations of between the changes in FTIR spectra and the chemical reactions during synthesis of the PCN-based systems have been analyzed in detail in Section 1.1. It should be noted that for all the samples after extraction of free PCL sub-chains, a decrease in the $\nu_{C=O}$ intensity is observed, which confirms a significant lowering of PCL content in these samples compared to that in non-extracted analogs [40].

2.3. Phase structure investigation

It was reasonable to investigate by DSC the solid-state arrangement of PCN/PCL hybrid networks before and after extraction as a function of the initial PCL content in different systems under study (Table 2.2 and Fig. 2.3). A single glass transition as detected for PCL contents varying from 5 to 50 wt% [25]. Moreover, regardless of the mass composition, it is noteworthy that the films were transparent before and after extraction, thus suggesting the absence of macrophase separation between PCL sub-chains and the PCN crosslinked matrix. Considering the difference between the refractive indices of both components significant (n_D^{25} (PCL) = 1.49 and n_D^{25} (PCN) = 1.53), the transparency of all samples was at least indicative of the occurrence of microdomains smaller than a few hundred nanometers [40]. As indicated in Table 2.2 the hybrid systems display two types of microphases. At low PCL initial content (*i.e.* up to 20 wt%), the glass transition associated with a single PCN-rich phase, mainly

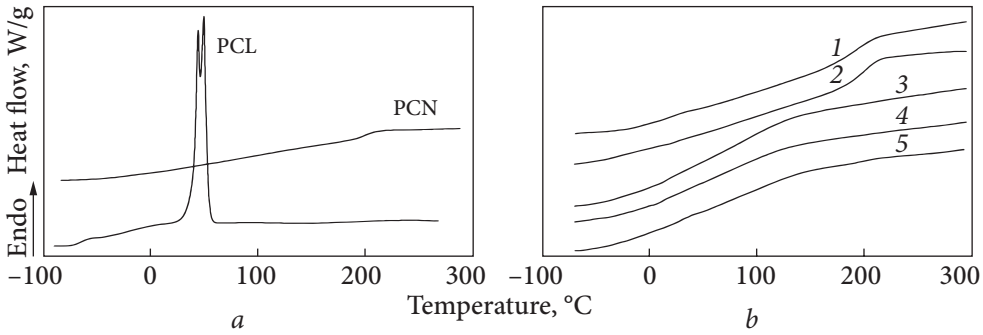

Fig. 2.3. Typical DSC thermograms (second heating scan) for (*a*) PCL oligomer and pure PCN network, as well as (*b*) PCN/PCL hybrid networks after extraction with various PCL contents (wt%): *1* — 5; *2* — 13; *3* — 16; *4* — 27; *5* — 36. The DSC traces are shifted vertically for the sake of clarity

Table 2.2. **DSC data for PCN/PCL hybrid networks after extraction**

PCN/PCL hybrid network composition after extraction [a] (wt%)	PCN-rich microphase [b]			PCN/PCL mixed microphase [b]		
	$T^{c}_{g,\,onset\ 1}$, °C	$\Delta T^{d}_{g\ 1}$, °C	$T^{e}_{g\ 1}$, °C	$T^{c}_{g,\,onset\ 2}$, °C	$\Delta T^{d}_{g\ 2}$, °C	$T^{e}_{g\ 2}$, °C
100/0 [f]	187 (219)	18 (34)	201 (233)	—	—	—
97/3 (95/5)	184 (186)	32 (46)	199 (204)	—	—	—
95/5 (90/10)	182 (176)	28 (41)	198 (196)	—	—	—
90/10 (85/15)	181 (156)	34 (48)	196 (184)	—	—	—
87/13 (80/20)	180 (162)	31 (36)	194 (179)	—	—	—
84/16 (70/30)	—	—	—	24 (79)	105 (51)	77 (104)
73/27 (60/40)	—	—	—	10 (72)	110 (38)	66 (90)
64/36 (50/50)	180 (—)	30 (—)	200 (—)	9 (66)	120 (38)	62 (83)
	0 / 100	1.158	0	—	—	—

[a] In the brackets: the initial compositions of hybrid networks before extraction; [b] In the brackets: the data corresponding to the compositions before extraction; [c] $T_{g,onset}$: the temperature associated with the intercept of the tangent to midpoint of the specific heat increment with the glassy baseline; [d] $\Delta T_g = T_{g,end} - T_{g,onset}$: the T_g range, where $T_{g,end}$ is the temperature associated with the intercept of tangent to midpoint of specific heat increment with the viscous baseline; [e] T_g: the temperature determined at the midpoint of the specific heat increment; [f] Pure PCN sample after extraction in acetone in conditions identical to those used for other samples studied.

constituted of PCN crosslinked sub-chains modified by PCL embeddings is observed. The sole T_g (T_{g1}) detected for these samples nearly corresponds to that of the neat PCN network. Still, the T_{g1} value slightly decreases with increasing PCL contents, due to the incorporation of soft PCL segments into the rigid PCN

structure. For the samples with initial PCL contents higher than 20 wt%, the PCN/PCL mixed phase formed by the PCL-modified PCN network becomes predominant over the PCN-rich microphase, therefore only the T_g (T_{g2}) of the hybrid network can clearly be observed.

No visible specific heat increment associated with T_{g1} was detected for the samples with an initial PCL content of 30—40 wt%. Due to the chemical incorporation of PCL into PCN structures, we observed a compatibilization effect of components, and broad glass transition zones situated between the T_g values of individual components could be determined: the higher the PCL content, the broader the T_{g2} range [40]. Such wide distributions of polymer chain mobility strongly indicate a substantial heterogeneity of composition in PCN/PCL hybrid networks with an initial PCL content of higher than 20 wt%.

As expected, the T_g values for the hybrid networks after extraction of free PCL were higher than those obtained for the PCN/PCL hybrid networks before extraction, due to the removal of non-incorporated PCL sub-chains having their own low T_g and acting as plasticizers [25]. All DSC data are in good agreement with the results previously obtained for non-extracted PCN/PCL networks using a dynamic mechanical thermal analysis [25].

2.4. Porosity analysis of PCN/PCL hybrid networks after extraction

The morphology associated with extracted PCN/PCL hybrid networks was assessed using SEM and DSC-based thermoporometry. The presence of pores in PCN/PCL samples after the extraction of unreacted free PCL was experimentally confirmed through SEM observations as illustrated in Fig. 2.4. The pore size and density depended on the initial PCL content in PCN/PCL networks. By means of the Origin 7 software, SEM micrographs were transformed into pixel matrices that allowed for the determination of pore diameters, as well as pore size distributions (Fig. 2.5*a*) [40]. Previous calculations have shown that the relative error of such measurements is in the range of 3.0—7.5 % [41—43], which may attest to the reliability of the results obtained. For the typical samples investigated, it was found that the average pore diameters were equal to 2—25 nm and the corresponding pore size distributions were in the range of 5—90 nm (Table 2.3). It is noteworthy that pore diameters smaller than 50 nm represented up to 95 % of all pore sizes. As expected, the total pore volume increased with increasing the initial PCL content (means the porogen content).

DSC-based thermoporometry allowed for the quantitative determination of the characteristics of porous structures, such as pore diameter (D_p)

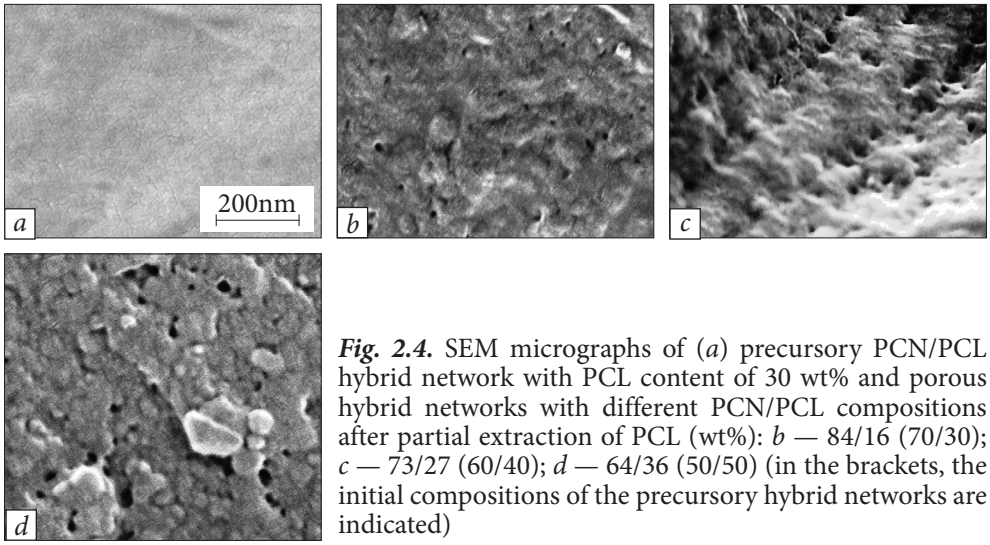

Fig. 2.4. SEM micrographs of (*a*) precursory PCN/PCL hybrid network with PCL content of 30 wt% and porous hybrid networks with different PCN/PCL compositions after partial extraction of PCL (wt%): *b* — 84/16 (70/30); *c* — 73/27 (60/40); *d* — 64/36 (50/50) (in the brackets, the initial compositions of the precursory hybrid networks are indicated)

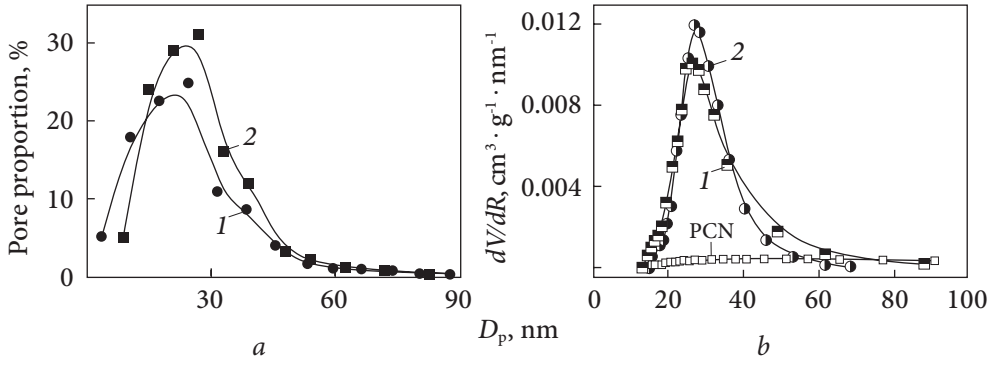

Fig. 2.5. Pore size distribution profiles obtained from (*a*) SEM analysis (the term "pore proportion" represents the mole percentage of pores for a given pore diameter) and (*b*) DSC-based thermoporometry: the neat PCN film (after extraction) and porous films of hybrid networks with different PCN/PCL compositions (wt%): *1* — 73/27 and *2* — 64/36

Table 2.3. **Porosity characteristics for typical porous hybrid networks**

PCN/PCL hybrid network composition [a], wt%	Average pore diameter, $D_{p(av)}$, nm		Pore size distribution, D_p, nm		Total pore volume, $cm^3 \cdot g^{-1}$	Percentage of pores with $D_p \le 50$ nm, %
	SEM	DSC	SEM	DSC		
73 / 27 (60/40)	22	26	3—90	15—90	0.25	95
64 / 36 (50/50)	25	28	5—80	15—70	0.28	94

[a] In the brackets, the initial compositions of hybrid networks before extraction are indicated.

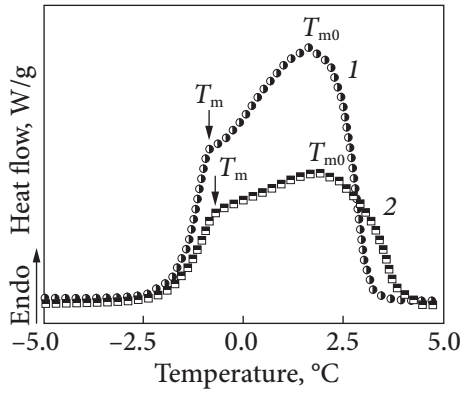

Fig. 2.6. DSC melting thermograms of water associated with porous films of hybrid networks with different PCN/PCL compositions (wt%): *1* — 73/27 and *2* — 64/36

and pore size distribution (dV/dR). The pore size distributions for typical samples investigated are presented in Fig. 2.5*b*.

When using water as a penetrating solvent for porous networks, two endothermic peaks appear in the DSC thermograms (Fig. 2.6), which evidence the melting of both water confined within the pores (T_m) and bulk water (T_{m0}) [34—36].

It should be noticed that PCL segments could not be hydrolyzed in the conditions employed for preparing the samples for DSC-based thermoporometry, *i.e.* pure water at room temperature for 2 weeks. Therefore, porous frameworks could only be obtained by acetone extraction of free PCL sub-chains. As discussed above, the higher the initial PCL content in the PCN/PCL system, the higher the amount of unreacted PCL extracted from the network matrix. Consequently, a higher porosity was expected for the resulting porous material (Table 2.3). As a result, the maximum intensity on the curve $dV/dR = f(D_p)$ for such a sample was higher (Fig. 2.5). The calculations showed that the average pore diameters were centered around 26—30 nm. Thus, the data obtained using thermoporometry are in good agreement with those derived from SEM analysis.

The porosity for the PCN/PCL hybrid networks after extraction was determined from density measurements [40] (Table 2.1). It can be seen that the higher the amount of extracted PCL from the network, the higher the porosity of the resulting porous film. In parallel, the porosity was calculated theoretically for each sample taking into account the volume fraction released by the uncrosslinked polymer extracted from the network. Both sets of values are in good agreement.

Dielectric measurements showed that the value of dielectric permittivity ε' (at 10^6 Hz) for the neat PCN was 2.56 (after extraction). For the PCN/PCL 70/30 wt% sample before extraction, the ε' value was equal to 2.90 due to the presence of PCL fragments of higher ε' (the values for polyesters are known to be comprised between 3.12 and 4.00) [44]. After partial PCL extraction, ε' decreased to 2.64, which is a quite low value and close to that of the pure PCN. Such a decrease might account for the occurrence of closed pore structures. The concomitant decrease in the density values (Table 2.1) tends to corroborate this assertion. Indeed, if the residual networks after extraction were constituted

of interconnected open pores, their density values would be equal or closer to those of non-extracted samples with the corresponding compositions. The conclusion drawn from the density and dielectric measurements was supported by SEM analysis, despite their qualitative character.

2.5. Thermal stability by TGA

The thermal stability associated with initial and porous films of PCN/PCL hybrid networks was investigated by TGA. The TGA curves of typical samples are given in Fig. 2.7 and the main thermal features are summarized in Table 2.4.

As previously described in detail [24], the thermal stability of PCN/PCL hybrid samples is lower than that of the pure PCN network, due to the incor-

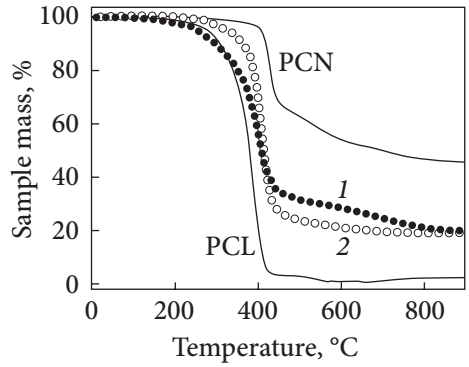

Fig. 2.7. Typical mass loss curves from TGA for PCL oligomer, pure PCN network, as well as precursory PCN/PCL hybrid network of 70/30 wt% composition (*1*) and resulting porous sample after extraction (*2*, actual PCN/PCL composition of 84/16 wt%)

Table 2.4. **Thermal properties of typical PCN/PCL hybrid networks before and after extraction as investigated by TGA**

PCN/PCL hybrid network composition, wt%	$T^{a}_{d\,(5\%)}$, °C	$T^{b}_{d\,(max)}$ / Δm [c] (°C) / (wt%)	$T^{d}_{d\,(50\%)}$, °C	Char residue, %
90/10 (before extraction)	389	421 / 28	470	35
95/5 (after extraction)	394	424 / 26	481	40
70/30 (before extraction)	268	409 / 49	411	20
84/16 (after extraction)	335	415 / 47	415	21
50/50 (before extraction)	252	396 / 51	396	4
64/36 (after extraction)	355	413 / 46	414	16
100/0 (pure PCN)	411	427 / 17	698	46
0/100 (pure PCL)	280	393 / 67	381	2

[a] $T_{d\,(max)}$, temperature of maximum degradation rate; [b] $T_{d\,(5\%)}$, temperature for a 5% mass loss; [c] Δm, mass loss at degradation temperature $T_{d\,(max)}$; [d] $T_{d\,(50\%)}$), temperature for a 50% mass loss.

poration of soft PCL fragments into the network structure, and also may be due to the formation of less regular structures with a lower crosslink density. As expected, the degradation temperature for the frameworks after extraction is higher than that of the corresponding non-extracted samples, due to the absence of free PCL sub-chains (thermally labile component) in the resulting systems. For a 5% mass loss, it is noticeable that the higher the initial PCL content, the greater the difference between the temperatures of 5% mass loss for the samples before and after extraction. In contrast, for a 50% mass loss, no remarkable dependence of the difference between the degradation temperatures for extracted and non-extracted samples was noticed with varying PCL contents. Overall, porous PCN/PCL hybrid crosslinked films were characterized by high thermal stability, and thus can be considered promising materials for applications involving thermostable membranes.

2.6. Conclusions

A straightforward and effective route to nanoporous film thermosets has been implemented through the partial removal of PCL sub-chains from PCN/PCL hybrid networks. Such crosslinked structures have been synthesized by *in situ* polycyclotrimerization of DCBE in the presence of varying amounts of PCL oligomers. The advantage of the non-quantitative chemical incorporation of PCL into the growing network structure was taken to generate nanoporous networks through the Soxhlet extraction of a significant part of PCL sub-chains. SEM and DSC-based thermoporometry analyses clearly show the formation of nanoporous frameworks with a maximal pore size lower than 90 nm and an average pore diameter of around 30 nm. The density and dielectric measurements strongly suggest the occurrence of closed pore structures.

In addition to their low average pore diameters and narrow pore size distributions, such novel porous PCN/PCL hybrid films are characterized by high glass transition temperatures and high thermal stability. All these important structural and physico chemical features make them suitable candidates for membrane technology requiring especially high dimensional and thermal stability.

CHAPTER 3

NOVEL MESOPOROUS HIGH-PERFORMANCE FILM MATERIALS FROM CYANATE ESTER RESINS AND INERT HIGH-BOILING-TEMPERATURE PHTHALATES AS POROGENS

3.1. Synthesis and nanoporous structure generation

Different methodologies have been reported to produce porous polymers [45]. Thermally and chemically induced phase separation is a very convenient method for preparing porous thermosets. Solvents are often used as porogens in synthesis of porous thermosets. Chemically induced phase separation was first proposed by Kiefer *et al.* in 1996 for epoxy resins [15, 16]; they used low molar mass liquids, *i.e.* hexane and cyclohexane, as the solvents for epoxy precursors. During the curing process, the homogeneous precursory system undergoes a phase separation into a polymer-rich continuous phase and a solvent-rich dispersed phase. The solvent-rich droplets subsequently grow and merge with each other. After the removal of the solvent, a porous structure is formed [46].

The main thrust of the present work relies on the implementation of an unprecedented methodology for the formation of mesoporous pure PCN films. First, a PCN network is synthesized in the presence of an inert liquid having a high boiling temperature and solely acting as a porogen that is not evaporated from the system before the completion of the polymerization process. Dimethyl phthalate (DMP) and dibutyl phthalate (DBP) are selected as porogenic agents. Such liquids are then extracted using a low-boiling-temperature solvent, *i.e.* acetone, thus leaving behind empty mesopores after drying. The scope and limitations associated with this straightforward and effective approach are addressed: in particular, we report on the correlations between the structure and properties of the precursory networks and those of the resulting porous systems as investigated by various physicochemical techniques, including gel fraction determination, FTIR, DSC, SEM, DSC-based thermoporometry, pycnometry, and TGA.

The PCN/DMP and PCN/DBP polymer systems were synthesized by step-by-step heating in a temperature interval of 150—

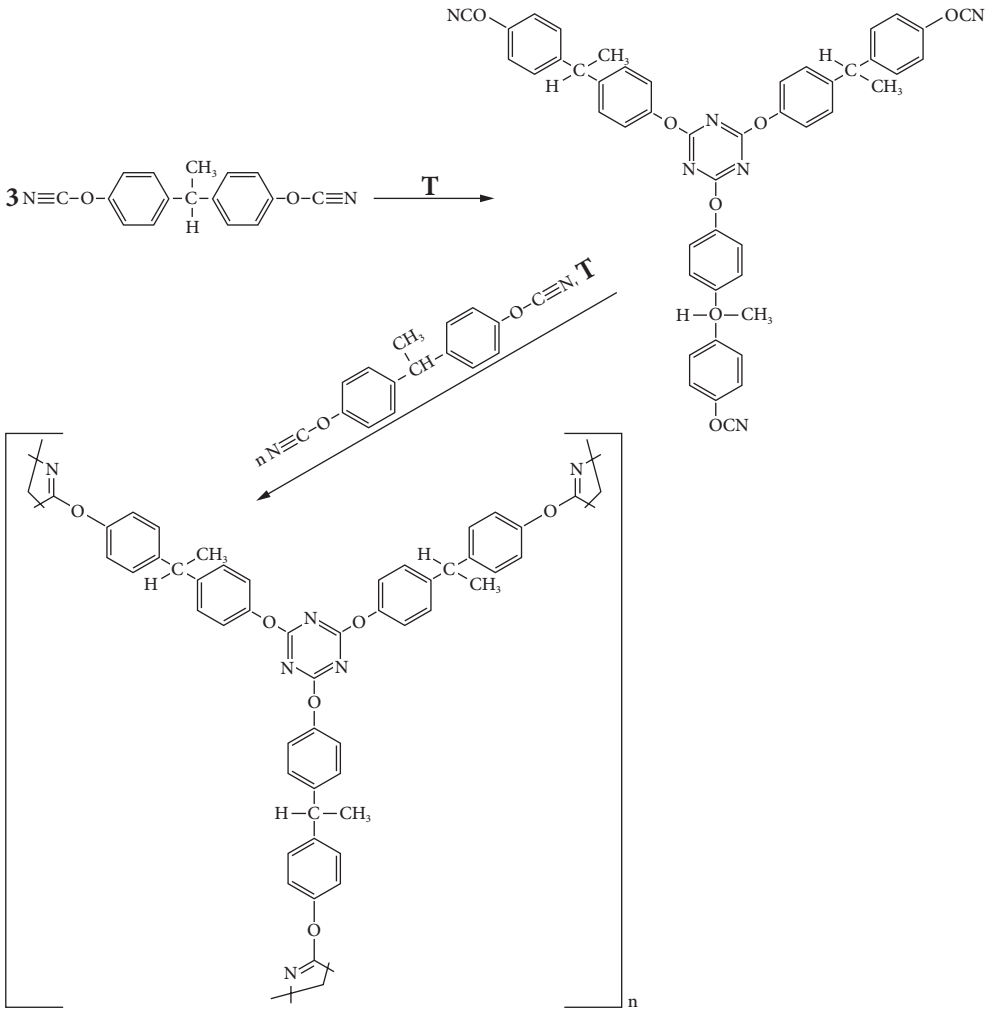

Fig. 3.1. Reaction scheme associated with polycyclotrimerization of DCBE cyanate monomer

210 °C for ~10 h. PCN/DMP and PCN/DBP films with a phthalate content of 5 10, 15, and 30 wt% were prepared. To accelerate the polycyclotrimerization of DCBE, 3 mol.% of triethylamine was added. The films with a thickness varying from 45 to 150 μm were removed from the oven and subjected to extraction [47, 48]. Then PCN/DMP and PCN/DBP films were extracted with acetone in a Soxhlet apparatus for 16 h followed by drying under vacuum at 50 °C up to the constant mass. The total extraction of the high-boiling-temperature liquids thus led to the creation of porous PCN materials.

The polycyclotrimerization of cyanate ester monomer results in the formation of a PCN network (Fig. 3.1).

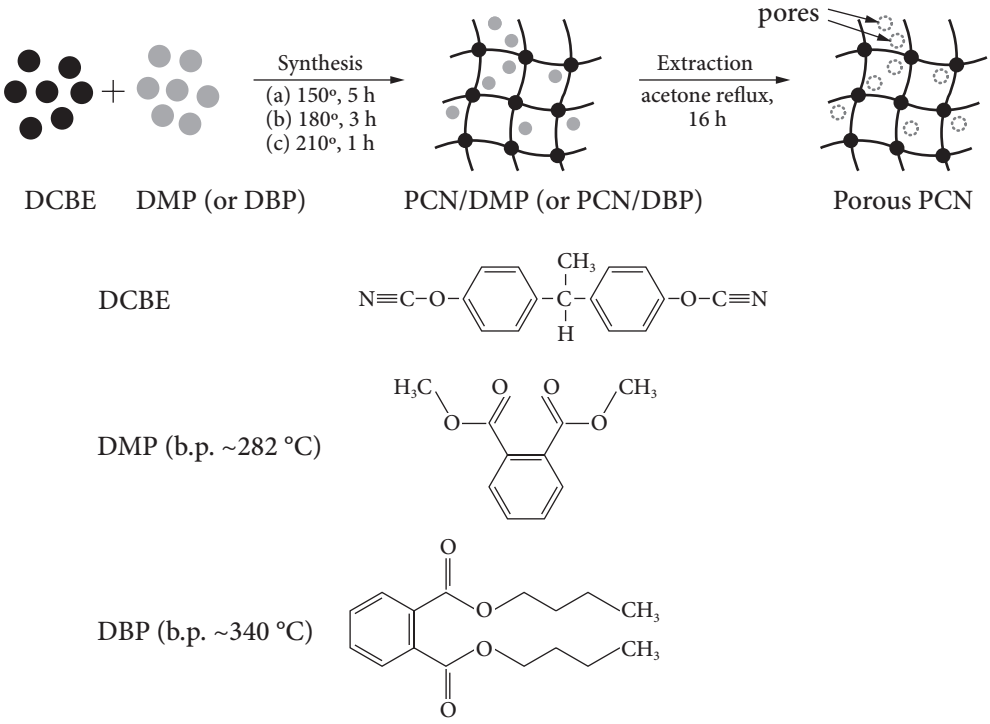

Fig. 3.2. Design of porous PCN networks using high-boiling-temperature liquids as porogenic agents

The mechanism proceeds through a step-growth process that is carried out via step-by-step heating described in detail in Chapter 2. After the first heating stage, a PCN gel possessing a moderate T_g value is generally formed. To increase the conversion of cyanate groups, and therefore the crosslinking degree of PCN, the polymerization temperature should be increased over the T_g of the growing network [49, 50]. At a higher reaction temperature, the network reaches higher T_g, and the next heating step has to be applied to reach the completion. Such a stepwise process results in the generation of a rather regular and fully crosslinked structure. Consequently, in order to generate pores in this structure by the phase-induced separation technique, the porogen should stay within the network up to the final stage of curing, and then has to be extracted from the resulting network. If the pore-forming solvent evaporates from the network during the intermediate stages of the curing procedure, the pores generated will collapse after the next heating step, *i.e.* at a temperature higher than the T_g of the growing network. Thus, the porogenic solvent should possess a higher boiling temperature than that of the last step of PCN curing, *i.e.* 210 °C in the present case, and be inert toward cyanate ester resins to avoid

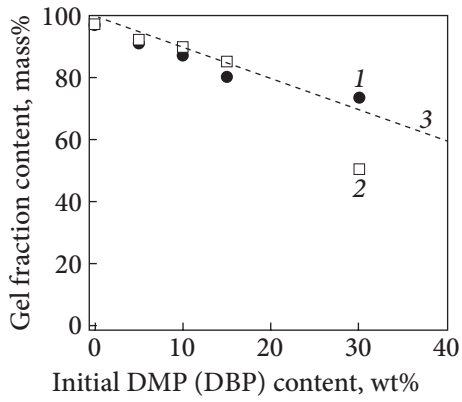

Fig. 3.3. Dependence of gel fraction content on (*1*) DMP or (*2*) DBP content in initial compositions with DCBE. The dotted line (*3*) is related to theoretical values

chemical grafting onto the network. Certainly, a two-phase morphology structure will be generated during curing as the forming PCN framework is insoluble in the porogen (poor solvent for PCN), while the cyanate monomer forms a homogeneous solution with the porogen (good solvent).

To ensure the compatibility of DCBE with high-boiling-temperature porogens, the solubility parameters associated with the different components were first calculated according to [51]. Since the solubility parameters of phthalates, in particular DMP (δ (DMP) = 21.9 $MPa^{1/2}$) and DBP (δ (DBP) = 19.0 $MPa^{1/2}$), turned out to be close to the value for DCBE (δ (DCBE) = 22.1 $MPa^{1/2}$) as well as to that for acetone, *i.e.* the extracting solvent (δ = 20.3 $MPa^{1/2}$), these high-boiling-temperature liquids were used as porogenic agents. To generate nanoporous film structures, a mere extraction of the porogen-containing PCN networks in acetone was applied. Fig. 3.2 schematically depicts the formation of porous PCN networks.

3.2. Determination of gel fraction contents

The gel fraction content associated with PCN samples was determined after acetone extraction [47]. As shown in Fig. 3.3 the experimental data on gel fractions are close to the theoretical values, which confirms the chemical inertness of phthalates and strongly attests to their quantitative extraction from the PCN-based networks. The experimental and theoretical values of gel fractions were calculated using Eqs. 2.1 and 2.2 given in Section 2.2.

Interestingly, for the PCN/DBP 70/30 wt% sample, the gel fraction was found to be equal to 50 wt%. In addition to the total extraction of DBP, some precursory material (20% of the total sample mass) was also extracted. This fact suggest that the presence of 30 wt% of DBP in the initial system limits the formation of a regular crosslinked PCN structure, thus the network synthesized probably possessed a higher degree of irregularity. This decrease in the gel fraction might arise from a lower rate of DCBE polymerization, due to a dilution effect. As a result, soluble uncrosslinked cyanurate pre-polymers were removed during the extraction process, according to an FTIR analysis (not shown here).

3.3. FTIR analysis

FTIR spectra of the neat PCN and PCN/DMP (or DBP) samples (Fig. 3.4) give evidence of the absence of absorption bands at 2272—2236 cm^{-1} corresponding to stretching vibrations of cyanate groups of DCBE [3], along with the appearance of intensive bands at 1358 and 1557 cm^{-1} associated with —C=N— and phenyl-oxygen-carbon valence vibrations of cyanurate units, respectively [3, 4, 18, 26].

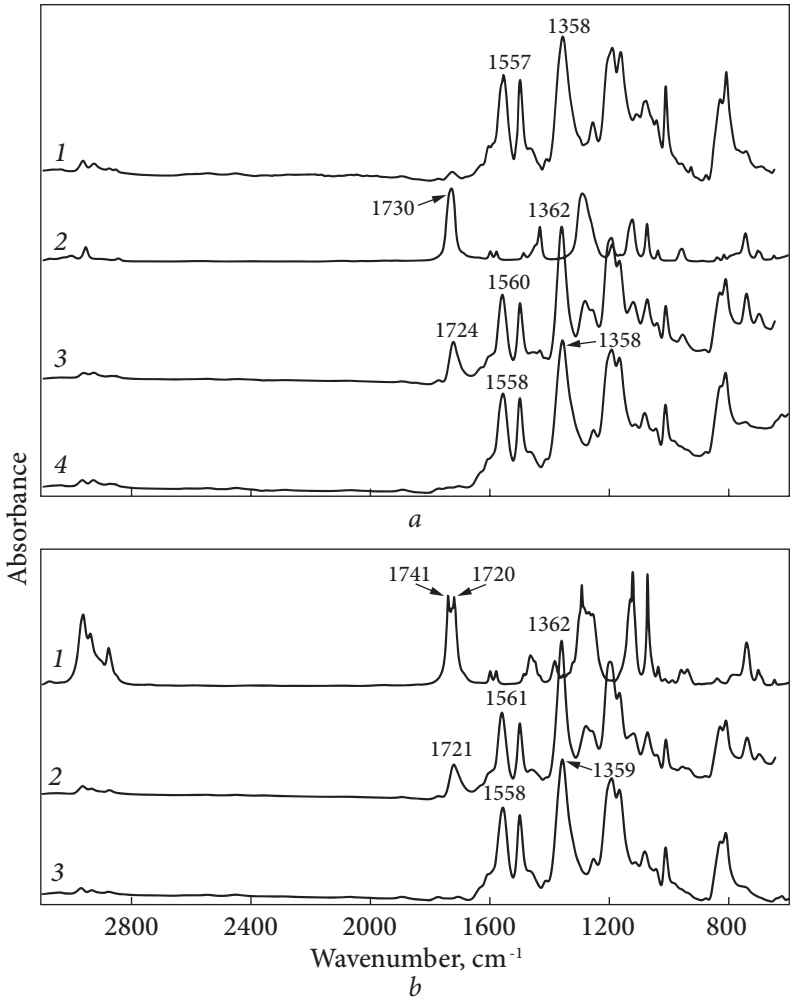

Fig. 3.4. FTIR spectra of (*a*) pure PCN network (*1*), pure DMP (*2*), PCN/DMP 70/30 wt% (*3*), resulting PCN network after DMP extraction (*4*), and (*b*) pure DBP (*1*), PCN/DBP 70/30 wt% (*2*), resulting PCN network after DBP extraction (*3*). The spectra are shifted vertically for the sake of clarity

Therefore, one can conclude that DCBE was fully converted into PCN networks. The presence of phthalates (DMP or DBP) in the corresponding PCN systems is confirmed by the occurrence of the strong carbonyl absorption bands at 1724 and 1721 cm^{-1} respectively. The slight frequency shift of the $\nu_{C=O}$ absorption maxima observed in the FTIR spectra of PCN/DMP (or DBP) samples in comparison with the absorption bands for pure phthalates is obviously due to the PCN component surroundings [28].

Moreover, one can clearly observe the disappearance of the $\nu_{C=O}$ absorption bands in the spectra of the resulting PCN samples after extraction of DMP (or DBP) by acetone, thus confirming the complete removal of high-boiling-temperature liquids from the PCN networks.

3.4. Glass transition behavior

The thermal behavior of PCN/DMP (or DBP) systems before and after extraction of the phthalates used has been investigated by the authors using DSC [47]. Typical thermograms are shown in Fig. 3.5 and the T_g values determined for all the systems under investigation are given in Table 3.1.

Table 3.1. **DSC data for PCN-based films before and after extraction**

Initial composition (wt%)	Samples before extraction			Samples after extraction		
	T_g[a], °C	ΔT_g[b], °C	ΔC_p[c], $J \cdot g^{-1} \cdot K^{-1}$	T_g[a], °C	ΔT_g[b], °C	ΔC_p[c], $J \cdot g^{-1} \cdot K^{-1}$
PCN 100	192	20	0.33	201	13	0.32
PCN/DMP						
95/5	180	21	0.34	214	16	0.27
90/10	168	22	0.33	213	16	0.25
85/15	119	31	0.37	213	20	0.31
70/30	111	33	0.34	210	21	0.31
PCN/DBP						
95/5	179	24	0.33	219	14	0.24
90/10	179	28	0.32	222	18	0.24
85/15	160	34	0.32	208	25	0.29
70/30	70	45	0.35	207	18	0.25

[a] Value determined at the midpoint of specific heat increment; [b] $\Delta T_g = T_{g,end} - T_{g,onset}$: width of T_g range, where $T_{g,end}$ and $T_{g,onset}$ are associated with intercepts of the tangent to the midpoint of specific heat increment with the viscous and glassy baselines, respectively; [c] $\Delta C_p = C_{p,v} - C_{p,g}$: heat capacity jump at T_g, where C_p is the heat capacity, and the subscripts v and g refer to the viscous and glassy states, respectively.

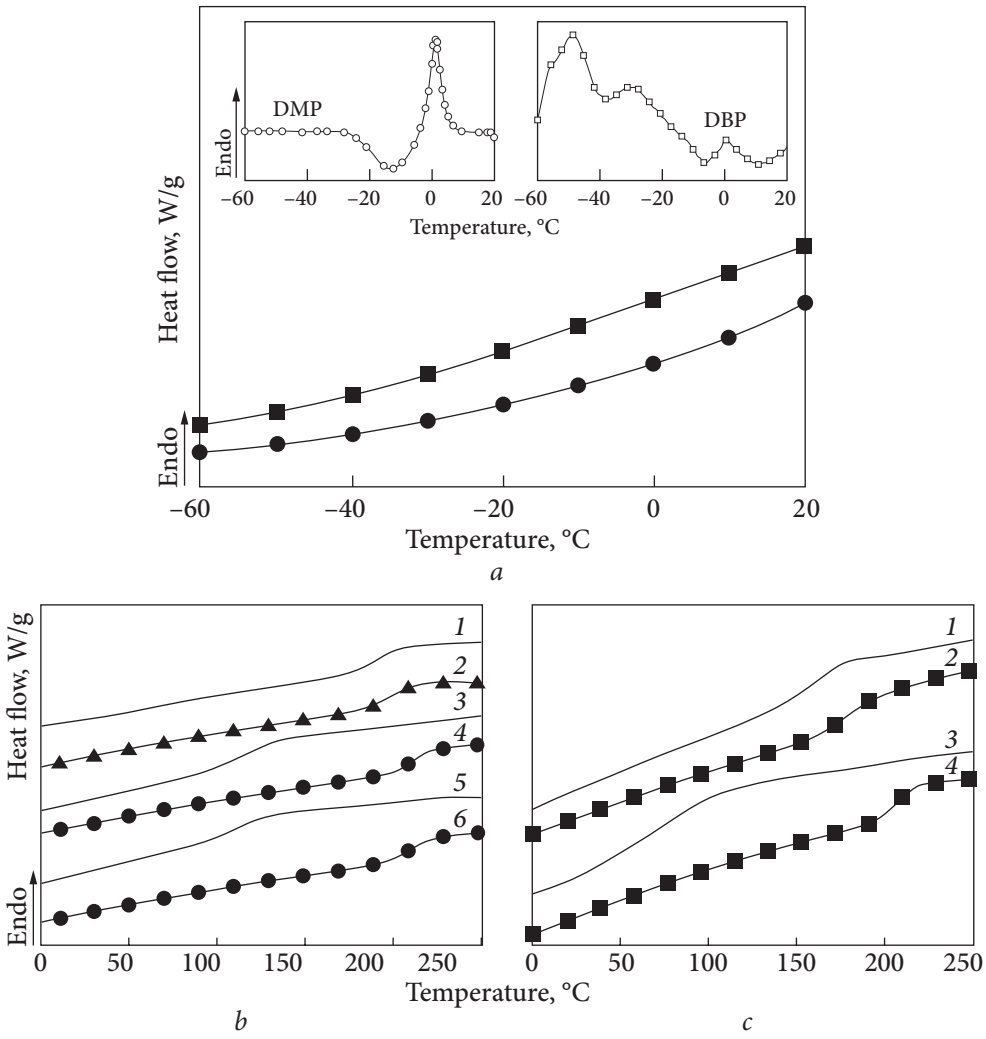

Fig. 3.5. Typical DSC thermograms: (*a*) first heating scan of pure DMP and DBP, (*1*) PCN/DMP 70/30 wt%, and (*2*) PCN/DBP 70/30 wt% before extraction; (*b*) second heating scan of (*1*, *2*) pure PCN network, (*3*, *4*) PCN/DMP 85/15 wt%, (*5*, *6*) PCN/DMP 70/30 wt%; (*c*) second heating scan of (*1*, *2*) PCN/DBP 85/15 wt%, (*3*, *4*) PCN/DBP 70/30 wt%. In (*b*) and (*c*), the solid lines correspond to the data before extraction, while the lines with symbols represent the data after extraction. The DSC traces are shifted vertically for the sake of clarity

First, in PCN-based samples before extraction, it is noteworthy that no melting endotherm of individual DMP (or DBP) (m.p.: ~0—1 °C for DMP, ~–35 °C for DBP) is detected (Fig. 3.5*a*). This suggests that the formation of PCN network prevents phthalate crystallization, and DMP (or DBP) is in the amorphous state in the crosslinked systems. The transparency of phthalate-

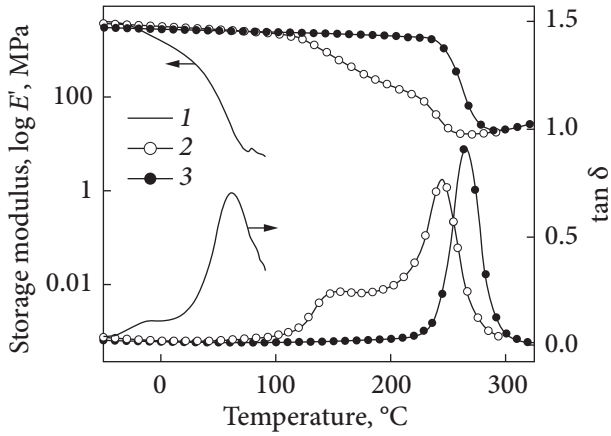

Fig. 3.6. Temperature dependence of storage modulus (E') and tangent delta (tan δ) for the samples studied: *1* — initial PCN/DMP 50/50 wt%, *i.e.* before extraction of porogen; *2* — nanoporous PCN/DMP 50/50 wt% after extraction, 1st heating run; *3* — PCN/DMP 50/50 wt% after extraction, 2nd heating run

containing samples can be explained by the insignificant difference between the refractive indices of PCN and phthalates (n_D^{25}(PCN) = 1.53, n_D^{20} (DMP) = = 1.49, n_D^{20}(DBP) = 1.51) [52, 53].

Second, the presence of DMP or DBP in PCN-based samples before extraction is reflected by a substantial decrease in the T_g values and a widening of the glass transition zone (ΔT_g), as compared to the pure PCN (Fig. 3.5*b*, *c*). The higher the phthalate content, the lower the T_g value and the broader the ΔT_g range, thus clearly indicating that phthalates act as plasticizers for the PCN crosslinked structure [47]. The lowest T_g value (70 °C) was obtained for the PCN/DBP 70/30 wt% sample, which correlates well with the previous data on gel fraction contents: for the latter system, not only DBP but also uncrosslinked cyanurate-containing macromolecules formed during the initial steps of the polymerization process induce a dramatic lowering of the T_g associated with the PCN network.

One can assume that, in addition to their plasticizing effect, the porogenic phthalates behave like diluents, thus facilitating the diffusion of growing chains and, consequently, the formation of a PCN network with a higher crosslink degree and structure regularity during the DCBE polycyclotrimerization.

In another work [48], three samples were investigated by DMTA (Fig. 3.6) to check the effect of DMP on their viscous-elastic properties (*i.e.* glass transition temperature, T_g). The DMTA for the initial PCN/DMP 50/50 wt% sample before extraction of porogen confirmed a significant decrease in the glass transition temperature of the PCN matrix ($T_g \approx 61$ °C, Fig. 3.6 curve *1*), due to the presence of a high amount of DMP. For the extracted PCN/DMP 50 wt% sample, two glass transition regions with $T_{g1} \approx 151$ °C and $T_{g2} \approx 245$ °C as well as the corresponding two step-drop mechanisms in the storage modulus ($log\ E' = f$ (T)) were observed (Fig. 3.6 curve *2*). The presence of the two T_g values can be explained by the occurrence of a micro-

phase-separated morphology with domains containing both PCN and residual DMP (T_{g1}) along with the pure PCN microphase (phthalate-free) with a higher T_{g2} value. For the extracted PCN/DMP 50/50 wt% sample after the second heating DMTA run, only one T_g value was observed ($T_g \approx 266$ °C, Fig. 3.6 curve *3*), which evidences the absence of the plasticizer in the sample. One can conclude that in such a sample, DMP is completely evaporated from the PCN matrix.

3.5. Characterization of porous structure

The occurrence of a porous morphology in the extracted PCN films was evidenced by SEM as illustrated in Fig. 3.7. Pore sizes varied from about 10 to 140 nm, and the average pore diameter in most of the samples was around 40 nm (Table 3.2). For instance, the SEM micrograph associated with the cross-section of porous PCN after extraction of 30 wt% of DMP (Fig. 3.7*b*) reveals the presence of longitudinal channels (dark cylindrical regions), which originated from the porogen tracks. Similar images were observed for the other samples with different initial PCN/DMP (or DBP) compositions (Fig. 3.7*a* as an example). It was found that neither the chemical structure of the porogenic phthalate (DMP or DBP) nor its initial content significantly influenced the average pore diameter in the resulting porous PCN films.

Additional confirmation of nanopore generation in PCN samples after phthalate extraction was provided by DSC-based thermoporometry described in Sections 1.1 and 2.2. Typical melting thermograms of water in the temperature region between –5 and +5 °C for porous PCN films are given in Fig. 3.8*a*, and the corresponding profiles of pore size distributions are shown in Fig. 3.8*b*. The peak intensity strongly depends on the initial phthalate content: a higher

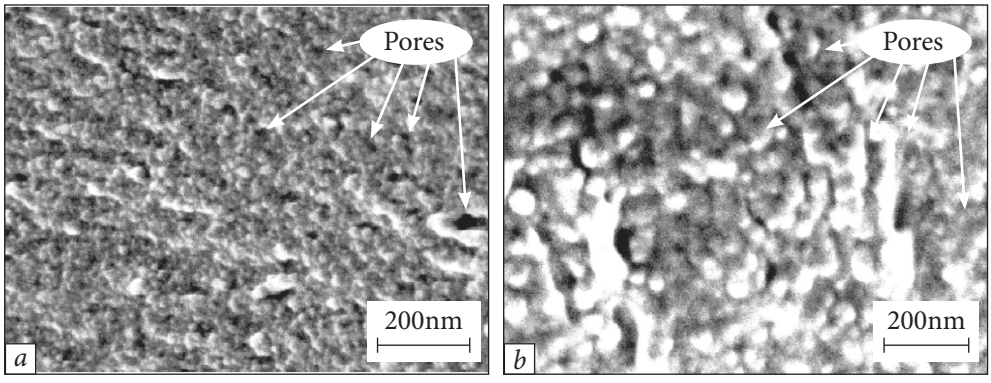

Fig. 3.7. Cross-sectional SEM micrographs of porous PCN-based networks: *a* — PCN/DBP 90/10 wt% and *b* — PCN/DMP 70/30 wt% after extraction

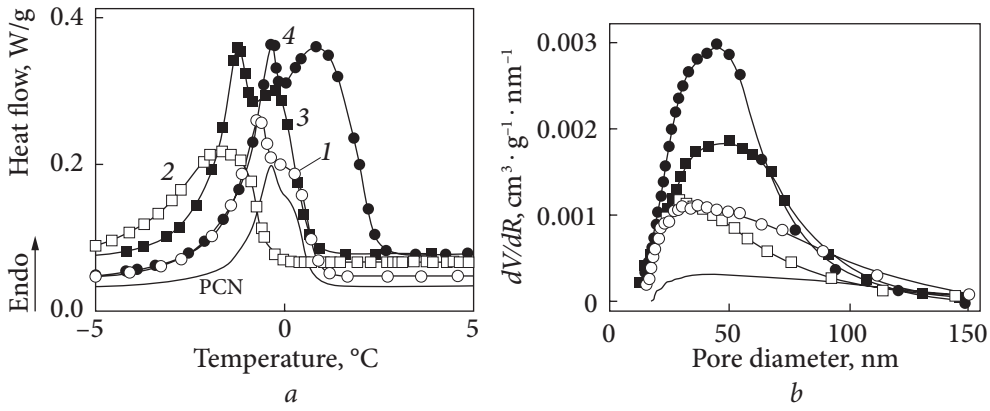

Fig. 3.8. Typical DSC melting thermograms of water associated with pure PCN and porous samples after extraction (*a*): *1* — PCN/DMP 95/5 wt%, *2* — PCN/DBP 95/5 wt%, *3* — PCN/DMP 70/30 wt%, *4* — PCN/DBP 70/30 wt%; *b* — corresponding pore size distribution profiles as determined by DSC-based thermoporometry

Table 3.2. **Main porosity characteristics for typical porous PCN films after phthalate extraction**

Initial phthalate content, wt%	Average pore diameter, $D_{p(av)}$, nm				Pore size distribution, nm			
	SEM		DSC		SEM		DSC	
	DMP	DBP	DMP	DBP	DMP	DBP	DMP	DBP
5	—	—	33	29	—	—	15—150	25—145
15	40	32	37	42	10—140	20—130	15—150	15—150
30	44	45	50	45	10—140	20—135	20—150	15—150

Initial phthalate content, wt%	Total pore volume [a] V_p, $cm^3 \cdot g^{-1}$		Porosity, *P*			
			Experimental [b]		Theoretical [c]	
	DMP	DBP	DMP	DBP	DMP	DBP
5	0.09	0.07	0.05	0.04	0.08	0.07
15	0.11	0.14	0.14	0.13	0.19	0.15
30	0.12	0.16	0.15	0.17	0.26	0.49

[a] Values calculated from the eq: $V_p = 1/d_s \times (q_w - 1)$, where d_s is the solvent density (water), q_w is the water uptake; [b] Values calculated from eq: $P = 1 - d_{app}/d_{true}$, where d_{app} and d_{true} stand for the apparent and true densities of PCN matrices, respectively; [c] Values calculated by taking into account the soluble fractions after extraction in acetone.

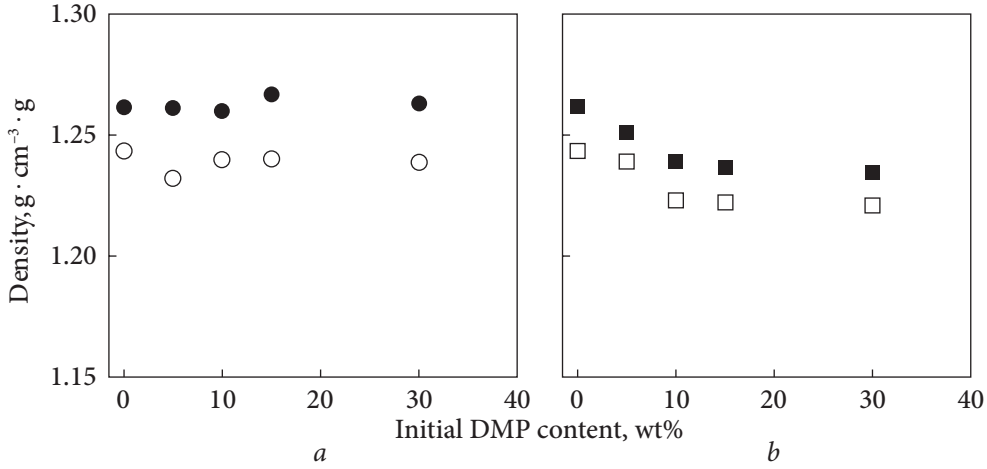

Fig. 3.9. Dependence of density associated with PCN-based precursors (full symbols) and corresponding porous samples (open symbols) on *a* — DMP or *b* — DBP content in initial compositions with DCBE

porogen content is associated with an increase in the peak intensity, due to the melting of a higher volume of confined water.

Therefore, increasing porogenic phthalate contents resulted in an increase in the peak intensity of dV/dR vs. D_p curves, thus affording higher pore volumes. A reference experiment was also realized with the neat PCN film to verify that it was basically non-porous, even after extraction.

Even though pore size distributions of PCN/DMP (or DBP) films were in the range of 15—150 nm, their average pore diameters were centered around 30—50 nm (Table 3.2). It should be stressed that pore diameters smaller than 50 nm represented up to 90 % of all pore sizes. The data thus determined using thermoporometry match pretty well the results obtained by SEM.

The porosity associated with the porous PCN films were evaluated from water uptake calculations and density measurements (Table 3.2). As expected, the higher the initial phthalate content in the precursor, the higher the porosity of the resulting porous film. Simultaneously, the porosity ratios were calculated theoretically by taking into account the soluble fraction content after acetone extraction. The theoretical values were systematically higher than the experimental ones. The discrepancy between both sets of results might probably stem from the fact that water did not probe all the pores of the analyzed films due to the high hydrophobicity of PCN matrices.

Fig. 3.9 displays the composition dependence of the density for PCN/DMP and PCN/DBP films before and after the extraction of phthalates from the networks. All porous samples exhibit density values lower than those of the corre-

sponding phthalate-containing precursors. The former have density even lower than that of non-porous neat PCN. Such a density decrease might account for the occurrence of a closed pore structure. Indeed, if the residual films after porogen extraction were constituted of interconnected open pores, their density values would be equal or closer to those of the non-porous neat PCN films.

3.6. Thermal stability and annealing behavior of nanoporous polycyanurate films

The influence of pores formed in PCN structures on the thermal stability of polymer films was investigated through TGA analyses. Typical curves of mass loss for different PCN-based samples, before and after extraction of the phthalates, are presented in Fig. 3.10, and the main thermal characteristics are listed in Table 3.3. The thermal stability of the PCN/phthalate precursory networks was significantly lower than that of non-porous neat PCN, due to the plasticizing effect induced by phthalates. PCN/DMP and PCN/DBP films before extraction showed an additional degradation stage with maxima at T_{d1} ~ 210 °C and 250 °C, respectively, which corresponded to the onset of phthalate evaporation. Moreover, the porogen-containing samples lost 15—30% of their mass in the temperature interval of 130—345 °C depending on the initial phthalate content. Interestingly, the temperature of the maximum degradation rate T_{d2} associated with these samples was only a few degrees lower than that for the pure PCN reference. This confirms the absence of any strong interaction between phthalates and PCN networks.

It is more noteworthy that, after the quantitative removal of DMP or DBP from PCN networks, the thermal stability of the residual porous samples was nearly identical to that of non-porous pure PCN. One can conclude that pore formation had no influence on the thermal stability of PCN networks; therefore, mesoporous PCN films may be considered promising materials for high-performance technology requiring high thermal stability.

Later on, we enlarged the concentration range and the phthalate types used for pore generation [62]. Moreover, a highly efficient catalytic complex instead of trimethylamine was used. Finally, a series of nanoporous PCN was synthesized with 20—50 wt% of porogen (dioctyl phthalate (DOP), DBP, or DMP) [54]. For the sake of clarity, in the further studies, a common coding for all the extracted and nanoporous samples was given, namely PCN_{AB}, where the subscripts A and B indicate the type (DMP, DBP, or DOP) and the initial content (from 20 to 50 wt%) of the porogen used, respectively.

The main porosity characteristics of the nanoporous PCN-based samples are given in Table 3.4. Further isothermal annealing was carried out in a programmable oven at temperatures (T_a) equal to 50, 100, or 150 °C for 48 h as

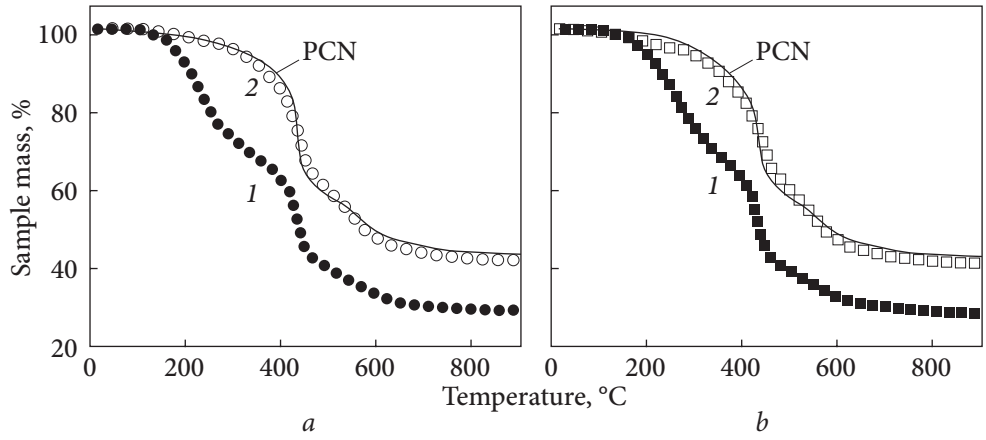

Fig. 3.10. Typical mass loss curves from TGA for non-porous PCN network, (*a*) PCN/DMP 70/30 wt% (*1*) before and (*2*) after extraction, as well as (*b*) PCN/DBP 70/30 wt% (*1*) before and (*2*) after extraction

Table 3.3. **Thermal properties of typical PCN-based films before and after extraction as investigated by TGA**

Thermal characteristic	PCN/DMP 70/30, wt%		PCN/DBP 70/30, wt%		PCN 100	
	before extraction	after extraction	before extraction	after extraction	before extraction	after extraction
T_{d1} [a], °C	210	—	250	—	—	—
T_{d2} [a], °C	429	440	426	438	427	435
T_{d3} [a], °C	535	543	541	553	—	547
$T_{d(5\%)}$ [b], °C	176	305	198	294	411	310
$T_{d(50\%)}$ [c], °C	434	579	434	571	698	589
m_1 [d], %	11	—	14	—	—	—
m_2 [d], %	23	27	44	26	17	27
m_3 [d], %	44	45	63	45	—	46
m_{char} [e], %	30	43	30	42	46	44

[a] T_{di}: temperature of maximum degradation rate for stage i considered; [b] $T_{d(5\%)}$: temperature for a 5 % mass loss; [c] $T_{d(50\%)}$: temperature for a 50 % mass loss; *d* m_i: mass loss at degradation temperature T_{di}; [e] m_{char}: mass corresponding to char residue.

well as at 250 °C for 24 h under an air atmosphere. Since significant darkening and brittleness of the samples were observed after 24 h at 250 °C, subsequent annealing was discontinued. To determine the mass evolution with time at a given temperature, the samples were periodically removed from the oven and weighed [54].

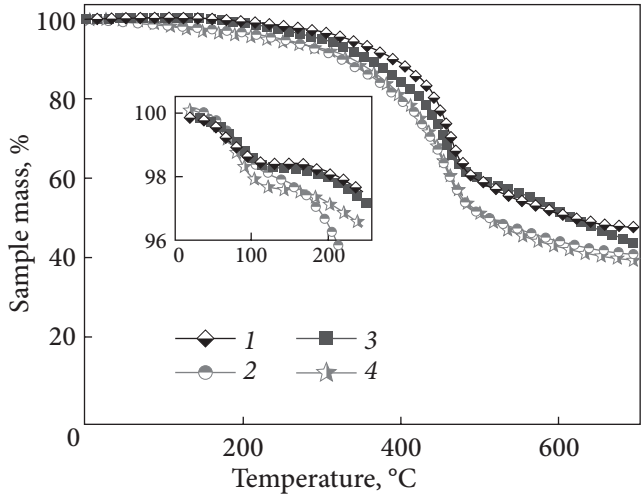

Fig. 3.11. TGA mass loss curves for the initial nanoporous samples: *1* — PCN_{DOP20}, *2* — PCN_{DBP30}, *3* — PCN_{DMP30}, and *4* — PCN_{DMP50}

Table 3.4. **Main porosity characteristics of nanoporous PCN-based samples under investigation**

Sample code	DSC-based thermoporometry		N_2 sorption	Sample code	DSC-based thermoporometry		N_2 sorption
	$D_{p(av)}$, nm	Pore volume [a], $cm^3 \cdot g^{-1}$	Specific surface area [b], $m^2 \cdot g^{-1}$		$D_{p(av)}$, nm	Pore volume [a], $cm^3 \cdot g^{-1}$	Specific surface area [b], $m^2 \cdot g^{-1}$
PCN_{DOP20}	33	0.08	58	PCN_{DMP30}	33	0.19	30
PCN_{DBP30}	49	0.12	61	PCN_{DMP50}	34	0.34	77

[a] Values determined according to the technique previously described [48]; [b] Values determined from nitrogen sorption measurements at 77 K by the BET method with relative pressure (P/P_0) values ranging from 0.05 to 0.30.

Prior to annealing studies, the thermogravimetric curves were obtained for these materials (Fig. 3.11). For the low-temperature range (<250 °C), a zoom of the data was included in the Figure. For all the systems, two main mass loss stages were observed [54], namely one of low magnitude (with a mass loss of around 2%) close to 100 °C followed by a plateau, then a second one centered at 450—470 °C (taking the extremum value on the corresponding derivative curve) with a 50—60% mass loss. At higher temperatures (~700 °C), about 40% of char residues was still present.

It is clear that all the samples exhibit similar thermal behavior, which is consistent with the fact that their chemical structures are very close. These results are also in good agreement with those for the neat PCN networks, as already observed by Korshak *et al.* [55, 56] and Ramirez *et al.* [57]. Although the curves are similar, some deviations arising from the structural differences caused by

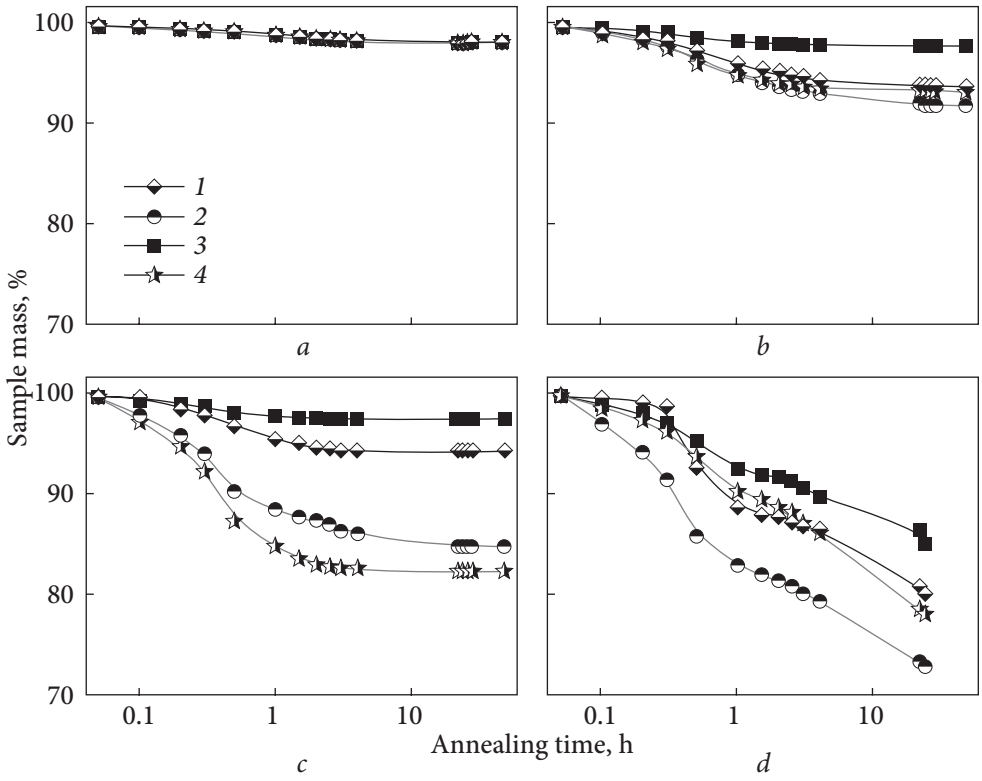

Fig. 3.12. Isothermal thermogravimetric curves for nanoporous samples: PCN_{DOP20} (*1*), PCN_{DBP30} (*2*), PCN_{DMP30} (*3*), and PCN_{DMP50} (*4*). Annealing was performed at T_a equal to 50 °C (*a*), 100 °C (*b*), and 150 °C (*c*) for 48 h or 250°C for 24 h (*d*)

the porogen used should be pointed out. For the low-temperature stage of mass losses, the curves obtained for the PCN_{DOP20} and PCN_{DMP30} samples are quasi superimposed, and a plateau at around 100—250 °C is clearly observed before the occurrence of the second mass-loss stage (in the temperature range ~250—450 °C). For the nanoporous PCN_{DMP50} sample such a plateau is less pronounced, and it is quasi absent for the PCN_{DBP30} network. Thus, the thermal stability in terms of mass loss at temperatures varying from 30 to ~100 °C seems to be identical for all the samples investigated, while within 100—250 °C thermal behavior of the nanoporous PCNs studied strongly depends on both the type and amount of the porogen used.

The results of thermal stability studies of the nanoporous PCN-based film materials associated with further isothermal annealing in the temperature range from 50 to 250 °C for 24—48 h are displayed in Fig. 3.12.

As seen, during annealing at T_a = 50 °C (Fig. 3.12*a*), all the curves are superimposed, and a very small mass loss of ~1% (quasi negligible) occurs after

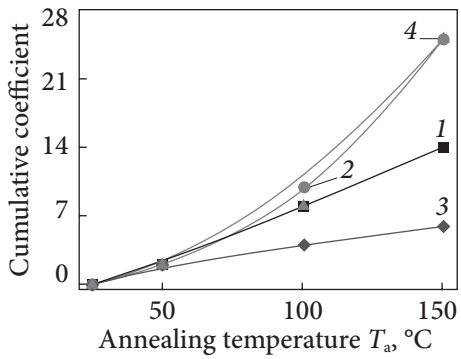

Fig. 3.13. Dependence of cumulative coefficient on annealing temperature for nanoporous samples: PCN_{DOP20} (*1*), PCN_{DBP30} (*2*), PCN_{DMP30} (*3*), and PCN_{DMP50} (*4*)

1 h which can be attributed to some moisture evaporation from the sample surface [18]. When the annealing temperature reaches T_a = 100 °C the mass of the PCN_{DMP30} sample remains quasi constant as compared to that after 48 h at T_a = 50 °C. Nevertheless, for the other samples, the mass loss changes are more apparent. The samples PCN_{DOP20} and PCN_{DBP30} reach a plateau with a mass loss of around 6%, while the PCN_{DMP50} network displays a plateau with ~8% mass loss. Annealing of the PCN_{DMP30} sample at T_a = 150 °C for 48 h was performed without any essential mass variations (a steady state was reached with ~2 % mass loss), whereas for the three other samples, more significant mass losses under different kinetic behaviors were observed. For instance, the nanoporous PCN_{DOP20} reached a steady state with ~5% mass loss after 2 h of annealing at T_a = 150 °C while relatively constant mass loss values for PCN_{DBP30} and PCN_{DMP50} samples (~15—17%) were reached after more than 10 h of annealing at the same T_a.

It is noteworthy that after 24 h of annealing at T_a = 250 °C for all the compositions investigated, no constant mass loss was achieved. A significant darkening and an increase in the fragility of the samples were also noticed. In this case, thermal-oxidative degradation occurred. Such results are consistent with the literature data published previously on the same family of nonporous PCN-based materials [55—57].

To have a better insight into the mass stability for all the nanoporous samples investigated, we have replotted the evolution of mass loss using the cumulative mass loss (CML) coefficient as a function of T_a applied. The CML parameter represents itself as a sum of mass loss values determined at the plateaus from the isothermal thermogravimetric curves (Fig. 3.12). The dependence presented in Fig. 3.13 allowed a comparative assessment of the PCN samples investigated and consequently of the equivalence of processes running after isothermal annealing.

The figure makes it possible to affirm that PCN_{DMP30} is quasi-stable during annealing at T_a ranging from 50 to 150 °C but that is not the case for all the other samples. For low annealing temperatures, we might accept the idea that the mass losses observed correspond to the bulk and confined water within the nanoporous materials. However, a mass loss of 20 % is too high to justify only a water evaporation process.

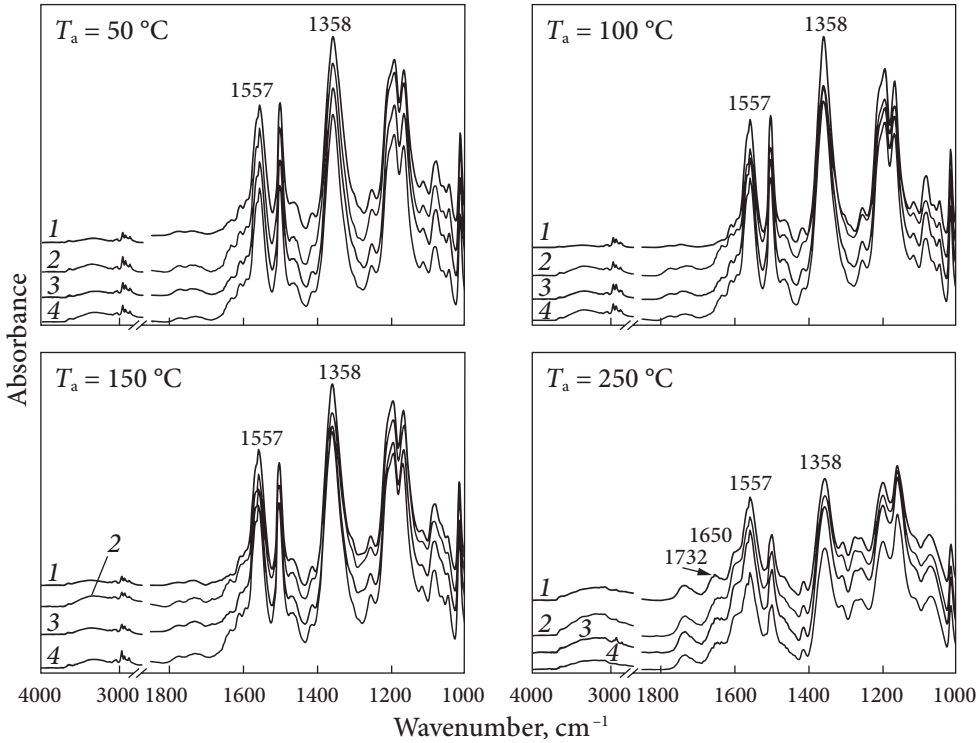

Fig. 3.14. FTIR spectra of nanoporous samples after annealing at different temperatures for PCN_{DOP20} (*1*), PCN_{DBP30} (*2*), PCN_{DMP30} (*3*), and PCN_{DMP50} (*4*). The curves are shifted vertically for the sake of clarity

Consequently, we investigated the effect of annealing on the chemical structure of these nanoporous PCN samples by means of FTIR spectroscopy (Fig. 3.14).

All the spectra evidence only marginal differences for the nanoporous PCNs after annealing at 50—150 °C for 48 h (Fig. 3.14) as compared to their non-annealed analogs. Therefore, the chemical structures of the nanoporous PCNs studied are not significantly affected by the annealing conditions used. However, after 24 h at 250 °C distinctive stretching vibrations with maxima at 1650 cm^{-1} and 1732 cm^{-1} corresponding to –C=N– and –C=O groups, respectively, appear in the FTIR spectra of all the samples. Moreover, redistribution and a significant decrease in the characteristic triazine peaks in the wavenumber range of 1100—1240 cm^{-1} and 1450— 1620 cm^{-1} are established. The growth of the intensity of bands within 3100—3800 cm^{-1} reflecting the changes in both OH and NH groups was also found. The revealed changes confirm the propagation of thermal-oxidative degradation of PCN triazine skeleton through the formation of at least carbamate derivatives [57]. At the same time, the significant decrease in the intensities of all the absorption bands in the middle IR range

allows assuming the generation of numerous gaseous degradation products investigated in detail in [55—57].

The main thermal characteristics of the annealed samples were also investigated by DSC and TGA (Table 3.5). The glass transition temperatures (T_gs) of all the nanoporous film samples annealed at 50—150 °C are found in the temperature range from 204 to 226 °C. For the samples annealed at 250 °C it is possible to determine the glass transition under the DSC conditions used.

Concerning the TGA results for the samples after annealing at 50, 100, and 150 °C one can observe the high thermal stability of the samples regardless the porogen used. The temperatures of the most distinctive stages of mass

Table 3.5. **Main thermal characteristics for the nanoporous PCNs annealed at different temperatures**

Annealed samples	Glass transition temperature T_g, °C	Temperature of maximum degradation rate [c]		Mass loss at T_{dmax}		Char residue, %
		T_{dmax1}, °C	T_{dmax2}, °C	Δm_1, %	Δm_2, %	
PCN_{DOP20}						
50 °C [a]	225	85	458	1	31	47
100 °C	221	77	458	1	30	48
150 °C	225	80	451	1	32	44
250 °C	— [b]	107	396	2	23	46
PCN_{DBP30}						
50 °C	209	88	459	1	34	45
100 °C	208	80	456	1	36	43
150 °C	209	83	449	1	34	45
250 °C	— [b]	105	396	2	18	48
PCN_{DMP30}						
50 °C	207	88	457	1	30	47
100 °C	208	75	462	1	30	48
150 °C	212	84	454	1	32	46
250 °C	— [b]	101	395	2	19	48
PCN_{DMP50}						
50 °C	204	79	462	1	34	41
100 °C	206	82	460	1	40	44
150 °C	207	80	455	1	33	40
250 °C	— [b]	92	395	2	20	46

[a] annealing temperature, T_a; [b] value not determined in the investigated temperature range (20—260 °C); [c] maximum values determined from derivative curves in the temperature range up to 500 °C.

losses with maxima at T_{dmax1} and T_{dmax2} are ~75—88 °C and 449—462 °C respectively, corresponding to the mass losses ~1% and 30—40 % (Table 3.5). The char residues are equal to 40—48 % for all the PCN-based nanoporous samples. The values of T_{dmax1} for the films annealed at T_a = 250 °C for 24 h were ~13—30% higher than those of the samples isothermally treated for 48 h at 50—150 °C. However, T_{dmax2} decreased from 450—460 °C to 395—396 °C apparently, due to the partial degradation of the network skeleton during annealing at 250 °C.

By coupling TGA and FTIR results and keeping in mind that the annealing process was performed far below the glass transition region ($T_a \leq T_g$), one could conclude that the mass loss observed at T_a up to 150 °C did not concern the degradation of any chemical bond in the PCN network skeleton. Therefore, only the porogen and some volatile molecules should be taken into account, *i.e.*, a temperature-induced desorption took place. This conclusion gave us the possibility to apply basic laws describing the diffusion processes to estimate the impact of the porous structure on the annealing behavior of the nanoporous PCN-based materials investigated. For this, Fick's second law was implemented as commonly used in similar cases. In this regard, the isothermal gravimetric curves were replotted in terms of conversion (α) as a function of annealing duration, where "zero-point" represents the initial mass of the nanoporous PCN sample investigated and 100 % conversion stands for the mass value after 48 h of annealing at 50, 100, or 150 °C (Fig. 3.15). Since the release of degradation products was detected after annealing at 250 °C no further calculations were considered.

The apparent diffusion coefficient, D_{ka}, was determined from the dependence of $\sqrt{t}$ on using the following equation:

$$\alpha = \frac{4}{L}\sqrt{\frac{D \cdot t}{\pi}}, \text{ for } \alpha < 0.5, \tag{3.1}$$

where L is the thickness of the sample, and t stands for the duration of annealing.

For $\alpha > 0.5$ α values were theoretically determined as follows:

$$\alpha = 1 - \frac{8}{\pi^2}\exp\left(-\frac{\pi^2 D t}{L^2}\right). \tag{3.2}$$

Fig. 3.15 reflects strong direct relationships between the annealing temperature and the α values, for all the samples. All the curves have similar features allowing assuming that their kinetic behaviors follow identical laws. The theoretical curves obtained by using Eqs. 3.1 and 3.2 are drawn with dashed lines. Based on the results obtained, the apparent diffusion coefficients D_{ka} were calculated for all the samples as a function of annealing temperature (Fig. 3.16).

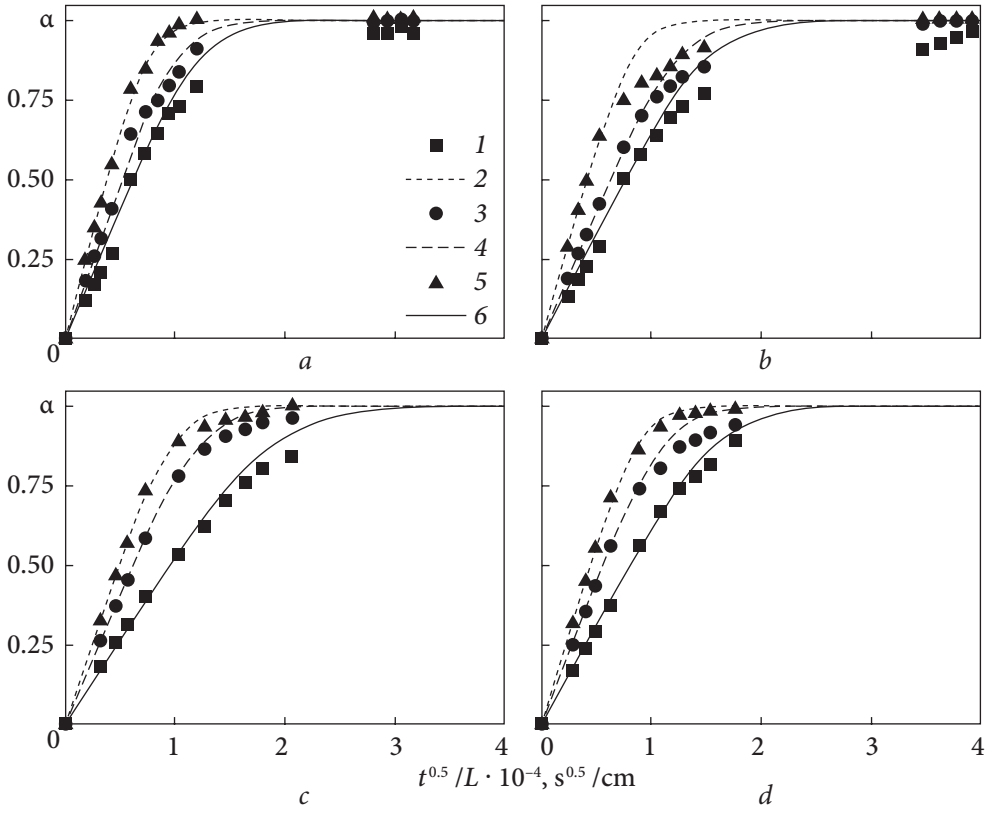

Fig. 3.15. Dependence of conversion (α) on $t^{0.5}/L$ for nanoporous PCN_{DOP20} (*a*), PCN_{DBP30} (*b*), PCN_{DMP30} (*c*), and PCN_{DMP50} (*d*) samples during annealing. Symbols represent the experimental data and dashed curves correspond to the theoretical values (as determined by Eqs. 3.1 and 3.2). Annealing was performed at 50 °C (*1*, *2*), 100 °C (*3*, *4*), and 150 °C (*5*, *6*)

The absolute uniformity of the relationships between the T_a and D_{ka} values for all the nanoporous samples studied thus confirms the similarity of the processes running during their annealing. Since no significant changes in chemical structures were found, the differences in D_{ka} values could rise from the structural changes in the nanoporous PCN samples (Fig. 3.16). We found nearly identical D_{ka} values for nanoporous PCN_{DBP30} and PCN_{DMP50} samples at any T_a applied, while for PCN_{DOP20}, the D_{ka} factor was the highest as compared to the other samples. Finally, for the nanoporous PCN_{DMP30} film material, the D_{ka} values were the lowest in comparison with those measured for the other nanoporous PCNs. It is clear that the sequence from the lowest to the highest values of D_{ka} is directly related to the data presented in Fig. 3.13, in particular they are associated with the cumulative lost masses obtained for each annealing temperature.

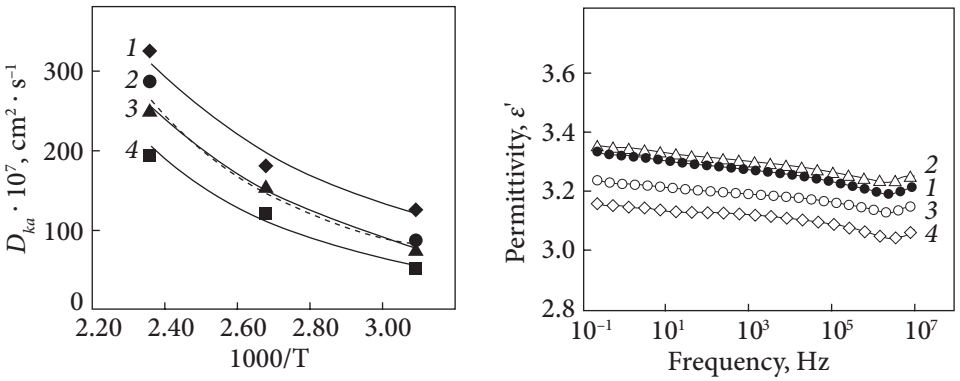

Fig. 3.16. Dependence of D_{ka} on $1/T$ for nanoporous samples during isothermal annealing: PCN_{DOP20} (*1*), PCN_{DBP30} (*2*), PCN_{DMP30} (*3*), and PCN_{DMP50} (*4*)

Fig. 3.17. Frequency dependence of permittivity (ε') for the samples of neat PCN (*1*), PCN_{DBP30} (*2*), PCN_{DMP30} (*3*), and PCN_{DMP50} (*4*). All the samples were tested after annealing at T = 250 °C for 2h

The D_{ka} values were mainly affected by the template of the nanoporous structure of the PCN-based samples prescribed by thermodynamic miscibility between the initial components (determined through the solubility parameters δ), the size of the porogen molecules, and the initial composition. In this regard, the most thermodynamically stable system was the DCBE/DMP mixture (of the hthalates used, the δ value of DMP was the closest to that for PCN monomer) while the DCBE/DOP composition display the lowest stability. Consequently, the chemically-induced phase separation in the DCBE/DMP mixture could occur later than in both DBP and DOP-containing DCBE mixtures under the same experimental conditions. Moreover, DMP molecules were the smallest porogenic agents, thus the generation of the most densely crosslinked PCN network after high-temperature synthesis was expected in this case, and consequently the lowest D_{ka} value for the final nanoporous PCN_{DMP30} sample was obtained. Increasing the initial DMP content up to 50 wt% facilitated the phase separation process (due to dilution effect), thus resulting in higher pore volume and D_{ka} values for the nanoporous PCN_{DMP50} sample as compared to the PCN_{DMP30} film with an invariable pore diameter. Replacing DMP with DBP caused a reduction in the thermodynamic stability of the initial DCBE-containing mixture, as mentioned above. Therefore, pore sizes in the PCN_{DBP30} sample increased, but pore volume appeared to be lower (due to the lower initial DBP content in the mixture) as compared to the PCN_{DMP30} sample. Since the δ value of pure DOP is lower by ~5.3 $MPa^{1/2}$ than that for individual DCBE component, the DCBE/DOP mixture possessed the poorest thermodynamic miscibility as compared to both DMP and DBP-containing DCBE compositions. The size of DOP molecules was

15—35 % larger than that of the other porogens used. Therefore, a rapid phase separation process could occur for the DCBE/DOP mixture under the same synthesis conditions. As a result, only 20 wt% of DOP could be successfully introduced into the PCN film material, and the final nanoporous PCN_{DOP20} sample had quite large pore sizes and the highest D_{ka} value, but the lowest pore volume as compared to the other PCN-based samples investigated.

Dielectric properties of the series of PCN/phthalate samples after thermal annealing were studied as well [48]. The neat PCN film presented a permittivity ε′ at 1 kHz equal to 3.29 (Fig. 3.17, curve *1*), which is relatively low and is known for polycyanurates [3]. It is noteworthy that the neat PCN sample was extracted in the same conditions as those used for the other samples. In the case of PCN/DBP 30 wt% (Fig. 3.17, curve *2* at 1 kHz, ε′ ~ 3.31), the ε′ values were slightly higher than those for the neat PCN film, which were probably within the range of experimental errors or due to the presence of DBP traces. For typical nanoporous PCN-based films, the permittivity values ε′ of PCN/DMP 30 wt% and PCN/DMP 50 wt% samples were equal to 3.20 and 3.13, respectively (at 1 kHz, Fig. 3.17, curves *3* and *4*). They were a little bit lower than the value of permittivity for the neat PCN, thus indicating the presence of pores in the films, but in relatively small content. Such results are in accordance with the formation of nanosized pores associated with relatively low values of the total pore volume in the PCN-based samples, as shown above by SEM and DSC-based thermoporometry (see Table 3.2).

By using the mixing rules ($\log \varepsilon' = x \times \log \varepsilon'_1 + (1 - x) \times \log \varepsilon'_2$ with x the pore content, ε'_1 and ε'_2 the dielectric constants of air (pores) and matrix, respectively), it as is possible to assess that nanoporous PCN-based matrices contained about 5 % of pores, thus corresponding to a slight decrease in the effective permittivity of the medium. Evidently, some pores collapsed after annealing of the samples at T = 250 °C for 2 h. Finally, it can be concluded that the nanoporous films studied exhibit dielectric properties typical for PCN matrices with low pore contents.

The specific surface area (S_p) is one of the most important features in the characterization of porous materials, and the Brunauer-Emmett-Teller (BET) analysis is the standard method for its determination from nitrogen adsorption isotherms [58]. When the BET method was applied to some nanoporous PCN-based samples developed, it was found that thermal annealing increased their S_p values, as expected, due to the increase in the V_p values. For example, for the nanoporous PCN_{DMP30} sample, the S_p value was equal to around 30 m^2/g while after annealing at 150 °C, it increased up to 70 m^2/g. Similarly, for the nanoporous PCN_{DBP30} sample, after annealing at 150 °C, the S_p value increased from 61 to 167 m^2/g. Correspondingly, such results are in accordance with the conclusions inferred from the DSC-based thermoporometry and SEM data.

3.7. Gas transport properties

Gas transport properties in polymers are governed by a diffusion/solubility mechanism which is closely related to the polymer chain mobility and to free volumes available for gas sorption and diffusion process. Although some gas sorption data have recently been determined for micro- and mesoporous polycyanurate networks [59, 60], no data concerning both gas diffusion and sorption properties have hitherto been reported for such PCN networks. It is worth noting that both parameters are important and useful to probe the structure and chain mobility of thermosets. As an example, previous studies performed on glassy epoxy networks [61] showed that increasing the network crosslink degree leads to an increase in gas solubility. It was observed that the gas diffusion simultaneously dropped due to the increase in the glass transition temperature. Also, there was revealed an increase in the diffusion coefficient within the network in the presence of a plasticizer (dibutyl phthalate) associated with a decrease in the gas solubility. These results were assigned to the rise of chain mobility and descent of the free voids available for gas sorption [61].

In our work [62] concerning nanoporous PCN films obtained through the use of phthalates as high-boiling-temperature porogens, gas transport properties, namely diffusion coefficient, solubility coefficient, and resulting permeability coefficient, were determined for a series of gases of different kinetic diameters, and the evolution of gas transport parameters of nanoporous PCNs as a function of the initial porogen content and the processing steps applied was discussed regarding the network structure.

Permeation measurements were performed at 20 °C for helium (He), oxygen (O_2), and carbon dioxide (CO_2) with respective kinetic diameters of 2.60, 3.46, and 3.30 Å respectively [63]. The PCN-based samples with a useful area of 3 cm^2 and a constant thickness of around 150 μm were placed between the upstream and downstream compartments of the permeation cell. A secondary vacuum desorption step was performed prior to each permeation experiment. The permeation was measured under an upstream pressure, P_1, equal to 3 bars. The downstream pressure, P_2, was estimated as a function of time. The permeability coefficient, P was calculated from the slope of the linear time dependence of P_2 in a steady state, and the diffusion coefficient, D was deduced from the time lag, θ as determined by the extrapolation of the steady state line on the time axis:

$$D = \frac{e^2}{6\theta}\ , \tag{3.3}$$

where e is the film thickness in cm, and D is expressed in $cm^2 \cdot s^{-1}$.

Assuming the Fickian transport mechanism, the solubility coefficient, S was calculated from the following equation [63]:

$$P = D \cdot S\,, \tag{3.4}$$

where S is expressed in $cm^3_{STP} \cdot cm^{-3} \cdot cm_{Hg}^{-1}$ and P — in barrers.

The sorbed CO_2 concentration (C_{CO_2}) was calculated from the solubility parameter by taking into account the gas pressure P_1 at which the permeation experiments were performed:

$$C_{CO_2} = S \times P_1\,, \tag{3.5}$$

The transport coefficient accuracy was estimated to be equal to ±8 %.

The ideal selectivity for a gas pair ($\alpha_{A/B}$) was also calculated by the ratio of the gas permeability coefficients as follows:

$$\alpha_{A/B} = \frac{P_A}{P_B}\,, \tag{3.6}$$

The gas transport parameters measured for different PCN films are listed in Table 3.6 [62]. It was impossible to determine the diffusion coefficient for helium with a high accuracy because the low kinetic diameter of He molecule

Table 3.6. **Gas transport parameters for PCN films under investigation**

Sample code	P_{He}, barrer	P_{O_2}, barrer	$D_{O_2}\,10^{-8}$, $cm^2 \cdot s^{-1}$	$S_{O_2}\,10^{-2}$, $cm^3_{STP} \cdot cm^{-3} \cdot cm_{Hg}^{-1}$	P_{CO_2}, barrer
PCN/DBP (70/30)	4.49	0.61	4.55	0.13	3.69
PCN/DMP (70/30)	3.14	0.37	2.00	0.18	1.40
PCN/DMP (50/50)	4.13	0.56	4.66	0.12	2.87
PCN_{DBP30}	6.82	0.61	0.58	1.05	3.15
a-PCN_{DBP30}	7.30	0.45	0.64	0.70	1.46
a-PCN_{DMP30}	7.30	0.72	0.94	0.76	2.28
a-PCN_{DMP50}	7.00	1.08	1.10	0.98	3.13

Sample code	$D_{CO_2}\,10^{-8}$, $cm^2 \cdot s^{-1}$	$S_{CO_2}\,10^{-2}$, $cm^3_{STP} \cdot cm^{-3} \cdot cm_{Hg}^{-1}$	C_{CO_2}, $cm^3_{STP} \cdot cm^{-3}$	α_{He/O_2}	α_{He/CO_2}
PCN/DBP (70/30)	1.56	2.40	5.62	7.4	1.2
PCN/DMP (70/30)	0.52	2.70	6.07	8.5	2.2
PCN/DMP (50/50)	1.21	2.37	5.33	7.4	1.4
PCN_{DBP30}	0.22	14.20	32.17	11.2	2.2
a-PCN_{DBP30}	0.16	9.30	20.92	16.2	5.0
a-PCN_{DMP30}	0.22	10.10	22.81	10.1	3.2
a-PCN_{DMP50}	0.26	12.10	27.22	6.5	2.2

The prefix 'a-' in sample codes distinguishes the annealed nanoporous PCN films.

made its diffusion rate high, leading to very low time lag values caused by the thickness of the films investigated.

Different trends can be observed from the transport parameters (Table 3.6). In particular, for all the membranes studied, the permeability coefficient increased going from O_2 through CO_2 to He. These variations are in agreement with the general trends observed for polymers. The high permeability level obtained for helium can be assigned to its low kinetic diameter and high diffusion rate. Oxygen exhibited lower permeability due to the combination of its low diffusion rate and low solubility. The intermediate values of permeability obtained for CO_2 can be assigned to the high solubility of this molecule.

In the film series investigated, the lowest gas permeability and solubility coefficient along with the highest gas diffusion rate were obtained before the Soxhlet extraction step. The phthalate molecules occupied the network's free volumes, which therefore were not available for gas sorption. It should also be noticed that increasing the DMP content in the PCN network had a much higher impact on the diffusion coefficient than on the solubility coefficient. In the non-extracted network series, the permeability seems to be governed by the kinetic parameter of the transport.

The high diffusion rate can be assigned to significant network chain mobility due to the plasticizing effect induced by the phthalate moieties. Indeed, the non-extracted networks exhibited low glass transition temperature with respect to the extracted ones (Table 3.7). After extraction, a narrowing of the ΔT_g range and a shift of the glass transition temperature to higher values were observed for all the samples studied. The interpretation of the ΔT_g values presented by Saiter *et al.* [64] indicates the fact that the higher the ΔT_g values, the larger the width of time distributions characterizing molecular

Table 3.7. **DSC data for PCN-based samples under investigation**

Sample code	Glass transition temperature, T_g, °C			
	onset	midpoint	end	ΔT_g^a
PCN/DBP (70/30)	80	104	129	49
PCN/DMP (70/30)	74	96	119	45
PCN/DMP (50/50)	88	105	123	35
PCN_{DBP30}	214	225	236	22
PCN_{DMP30}	210	224	238	20
PCN_{DMP50}	204	214	224	28

[a] The glass transition temperature range (ΔT_g) calculated as the difference between end and onset temperatures associated with the glass transition zone.

dynamics, and therefore the higher long-scale structural disorder in the materials is expected.

The impact of the extraction step was investigated on the PCN/DBP (70/30) sample (Table 3.6). Indeed, the previous analysis performed on PCN films based on higher porogen contents evidenced the presence of a certain degree of heterogeneity after the Soxhlet extraction [48]. This could make difficult the interpretation of the gas transport behavior. The data presented in Table 3.6 reveal that the extraction performed on the PCN/DBP film has a significant effect on He permeability, whereas it only slightly modifies O_2 and CO_2 permeability values. The low variation of the oxygen and carbon dioxide permeability values observed for this network can be explained by the opposite variation of the diffusion and solubility coefficients. The extraction step led to the formation of nanosized pores, thus explaining the significant increase observed in gas solubility. However, the loss of DMP simultaneously led to a significant decrease in the chain mobility, thus making the diffusion rate slower.

The significant impact of the extraction step observed on He permeability can be assigned to the small kinetic diameter of this molecule and its lower sensitivity to variation of polymer chain segmental mobility. The expected decrease in the diffusion coefficient due to chain mobility restriction should then be much less important for this gas in comparison with gases constituted of larger molecules. As a result, a significant increase in helium permeability was observed for the films after extraction causing an increase in the He/CO_2 and He/O_2 selectivity by a factor of ~1.5—1.8 with respect to the non-extracted analog. Last, it is noteworthy that the amount of CO_2 sorbed in the PCN_{DBP30} film (*e.g.*, C_{CO_2} ~32 $cm^3_{STP} \cdot cm^{-3}$ Table 3.6) is close to those reported on micro- and mesoporous polycyanurate networks, despite different pore contents and sizes. Indeed, the films prepared by Yu *et al.* [59, 60] were characterized by smaller pore sizes but bigger total pore volumes as compared to those investigated in our work [62].

The effect of additional heating of the nanoporous films above their glass transition temperatures (*i.e.*, at 250 °C) was also estimated. Comparative studies of transport properties of PCN_{DBP30} membranes before and after annealing showed that one such a post-treatment does not significantly modify He permeability; it rather leads to a decrease in CO_2 and O_2 permeability coefficients. Taking into account the uncertainty, one can conclude that O_2 and CO_2 diffusion coefficients did not vary, whereas the gas solubility diminished after the annealing step. It was shown that during annealing at 250 °C porogen evaporation occurred, and post-curing of dangled PCN chains might also take place. As the PCN crosslink degree was already high before the annealing step, it can be assumed that the variation of the T_g value induced by the additional thermal post-curing was not high enough to have a significant impact on the D values.

However, as the annealing at 250 °C took place in the rubbery state, changes in porosity occurred due to possible chain rearrangement within the PCN networks. The decrease in the gas solubility indicates hat a decrease in the global pore volume and an increase in the gas selectivity can be related to the decrease in the average pore sizes.

The CO_2 and O_2 transport parameters measured for the a-PCN_{DMP30} sample were systematically slightly higher than those determined for a-PCN_{DBP30}. The lower molecular mass of DMP as compared to that of DBP as well as the lower affinity of DBP to PCN monomer (DCBE) [48, 54] led to the introduction of a higher number of porogen molecules in the PCN/DMP samples than that in the PCN/DBP ones. After porogen desorption, these facts resulted in higher pore volume contents for PCN/DMP samples as compared to PCN/DBP ones. This effect was emphasized by increasing the DMP amount from 30 to 50 wt%. A certain growth of the pore volume had a higher impact on the behavior of CO_2 and O_2 in comparison with He, thus showing again the importance of the diffusant kinetic diameter for the transport mechanism in the nanoporous thermosetting polymer series studied.

3.8. Conclusions

The synthesis of polycyanurate networks in the presence of high-boiling-temperature liquids, such as dimethyl phthalate, dibutyl phthalate, or dioctyl phthalate, followed by their quantitative extraction with acetone and drying of the resulting films, enables the straightforward and effective formation of mesoporous PCN thermosetting films. Such frameworks have fully been characterized by gel fraction determination, FTIR, DSC, SEM, DSC-based thermoporometry, and pycnometry. Pore sizes ranging from 10 to 150 nm can be generated. Although phthalates act as plasticizers by decreasing the thermal features of the modified PCN networks such as T_d (TGA) and T_g (DSC), the removal of porogenic liquids in porous frameworks leads to the recovery of thermal characteristics compared with those of the neat PCN.

Thermostable nanoporous polycyanurate films possessing high glass transition temperatures and low dielectric constants are expected to be promising materials for advanced applications in many branches of industry, including microelectronics, airspace technology, and the automotive industry.

This chapter has reported the annealing behavior and thermal stability of nanoporous thin-film materials based on cyanate ester resins synthesized via chemically induced phase separation using high-boiling-temperature (T_b ~ 282—384 °C) low-molecular-mass (M ~ 194—310 g · mol^{-1}) phthalates as porogens with different sizes of molecules (r ~ 4.05—5.45 · 10^{-10} m). The response of the materials investigated to isothermal annealing (in an air atmo-

sphere) in the temperature range from 50 to 250 °C for up to 48 h has been analyzed in detail. It was found that depending on the type and amount of the porogen used, a steady state during isothermal treatment at temperatures below the glass transition (*i.e.*, up to ~200—220 °C) in the final nanoporous films is reached after 5—20% loss of the initial mass associated with the desorption process of both moisture and porogen molecules trapped in the densely crosslinked CER matrix. It has been established that isothermal annealing has no influence on the chemical structure and thermal performances of the annealed PCN-based samples, which allowed for applying the desorption law to describe the kinetics of annealing of the nanoporous PCNs studied using the proposed model in a quantitative manner. The values of the apparent diffusion coefficient have shown a strong influence of the molecule size and amount of the porogen used on the desorption behavior of the nanoporous PCN-based films during isothermal annealing at 50—150 °C.

The increase in annealing temperature to 250 °C resulted in an unceasing mass loss tendency accompanied by irreversible changes, such as darkening, increasing fragility, and some changes in chemical structure, in all the nanoporous samples studied, as confirmed by the FTIR spectroscopy measurements, which were associated with the thermal-oxidative degradation process. Thus, the methodology applied and the numerous dependences revealed can be useful in terms of understanding and prediction of high-temperature short-term and long-term application of nanoporous thin-film materials based on high-performance cyanate ester resins under both isothermal and dynamic conditions.

Interestingly, the nanoporous thermosetting materials demonstrated a significant increase in He permeability after porogen extraction. Moreover, all membranes exhibited higher CO_2 and O_2 sorption abilities and increased He/O_2 and He/CO_2 selectivity factors after porogen desorption (*i.e.*, after the annealing step). It has been shown that both the chain mobility and free volume govern the gas transport properties before porogen extraction, whereas the pore volume content and pore size become predominant factors in the case of the PCN membranes obtained. Additional annealing of these high T_g systems in the rubbery state clearly leads to the modification of the porous network structure, which allows for an increase in the separation ability between low- and high-sized gas molecules in the glassy state.

CHAPTER 4

CREATION OF NANOPOROUS POLYCYANURATE THERMOSETS BY USING IONIC LIQUIDS

4.1. Introduction

Ionic liquids (ILs) are organic salts that typically consist of bulky, asymmetric organic cations and inorganic symmetric anions. Room-temperature ILs are defined as salts with melting points below or equal to room temperature [65, 66]. ILs have attracted widespread interest in polymer science due to their versatile properties, such as negligible saturated vapor pressure, wide liquid-state temperature range, non-flammability, incombustibility, high electrical conductivity, and good stability to oxidation [67—71]. They have progressively been used as solvents and catalysts for polymerization reactions [71] as well as additives in the design of polymer materials [72]. Their peculiar structure enables easy separation, recovery, and recycling of the catalyst from the reaction mixtures. In the case of membrane processes, ILs are used in the design and modification of advanced materials that enable performance levels not typical for conventional materials [73]. Another application of ILs consists in using them as effective and reusable porogens in vinylic networks [74]. When ILs are used as porogenic solvents, during the *in situ* formation of polymer networks, chemically-induced phase separation occurs. To act as efficient porogens, ILs have to possess: (*i*) high-boiling temperature to avoid any premature evaporation, (*ii*) high thermal stability to remain unchanged up to the complete curing of the polymer networks, and (*iii*) easy extractability to be readily removed from the cured networks, thus affording porous thermosetting materials. Porous polymeric materials have a large variety of applications in many areas as highly selective membranes, adsorbents, and filters, porous electrodes for fuel cells, sensors or insulators, *etc.* [44].

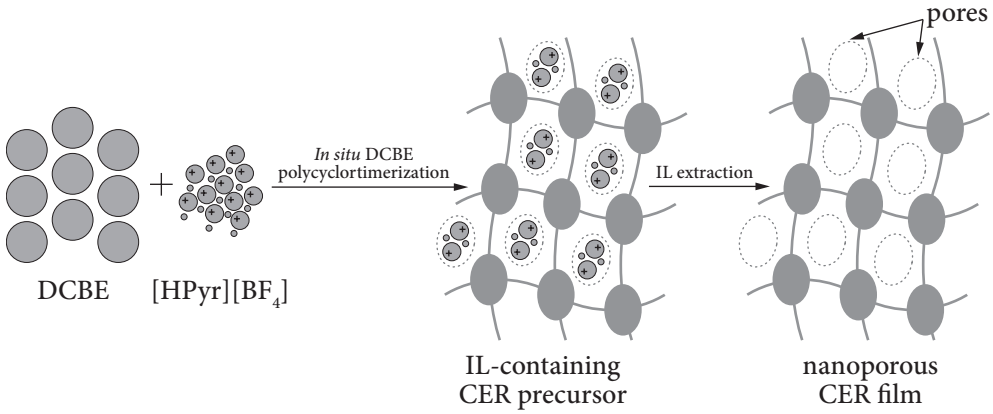

Fig. 4.1. Representative scheme of CER formation in the presence of $[HPyr][BF_4]$ and subsequent pore generation

Recently, we have investigated the catalytic effect of ILs on the curing process of CERs, and an acceleration effect has clearly been highlighted in the polycylotrimerization of dicyanate ester of bisphenol E in the presence of a specific IL [75].

In papers [75, 76], we have informed about our engineering novel nanoporous CER-based thermosetting films by using a room-temperature IL, namely 1-heptylpyridinium tetrafluoroborate ($[HPyr][BF_4]$), as a porogen, and investigation of the effect of porogen content on the structure and properties of resulting porous CERs.

DCBE was mixed with $[HPyr][BF_4]$ in a given ratio (the content of $[HPyr][BF_4]$ was equal to 20, 30, and 40 wt%), and the homogeneous mixtures were subjected to an ultrasonic bath at 60 °C for 30 min. These solutions were then poured into a PTFE-coated mold and cured over the temperature range from 25 to 250 °C with a heating rate of 0.5 °C/min. The generation of nanoporous thermosetting films was accomplished through the formation of CER-based thin films derived from the *in situ* polycyclotrimerization of DCBE in the presence of $[HPyr][BF_4]$ with further removal of the latter. The CER formation in the presence of $[HPyr][BF_4]$ and subsequent pore generation are schematically presented in Fig. 4.1) [76].

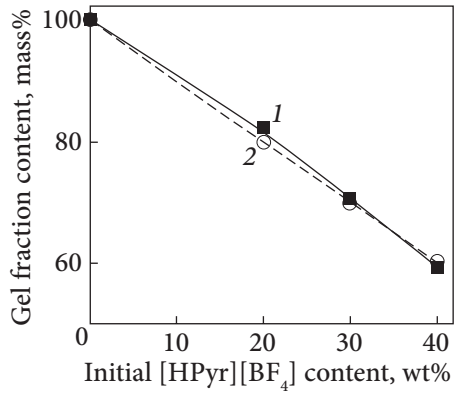

Fig. 4.2. Experimental (*1*) and theoretical (*2*) values of gel fraction contents after extraction as a function of the $[HPyr][BF_4]$ content wt%

For the generation of a porous structure, the films obtained with a thickness of around 100 μm were subjected to ext-

raction with ethanol in a Soxhlet apparatus for 16 h. After extraction, the samples were dried at 25 °C up to a constant mass. The following codes were applied to the samples under investigation: CER_{ext}, CER_{20ext}, CER_{30ext}, and CER_{40ext} for the extracted CER sample synthesized without IL and for extracted CER samples synthesized in the presence of IL, where the subscripts indicate the initial content of [HPyr][BF_4]. The code CER40 was applied to the non-extracted sample with a [HPyr][BF_4] content of 40 wt%; it was used as a reference sample for the sake of comparison.

The gel fraction contents associated with CER samples were determined after ethanol extraction [76]. Fig. 4.2 shows that the experimental and theoretical values of the gel fraction content nearly, coincide thus strongly suggesting the completion of CER formation and [HPyr][BF_4] extraction from CER-based networks and confirming the chemical inertness of the IL toward CER. It should be noted that even a [HPyr][BF_4] content as high as 40 wt% in the initial system did not hinder the formation of a highly crosslinked CER structure.

4.2. Spectroscopic analysis of network structure

In order to evaluate the effect of [HPyr][BF_4] on the network structure and further confirm its chemical inertness to DCBE, the FTIR analysis was performed [76]. Fig. 4.3 displays FTIR spectra of CER_{ext}, CER_{40ext}, CER_{40}, and pure [HPyr][BF_4]. The FTIR analysis of the CER_{40ext} sample (and of the other extracted CER samples, not shown here) demonstrates the presence of C=N—C and N—C—O/N=C—O stretching absorption bands of cyanurate repeating units at 1356 cm^{-1} and 1558 cm^{-1} respectively, and does not indicate any stretching absorption bands of unreacted cyanate groups at 2272—2236 cm^{-1} thus corroborating the formation of CER network.

It should be pointed out that, for both the CER40 and the pure [HPyr][BF_4], the band at 1490 cm^{-1} and the broad band with a maximum at 1058 cm^{-1} corresponding to the stretching mode of pyridinium cation [77] and the asymmetric stretching of BF_4^- anion of the IL, respectively, were observed. Logically, after [HPyr][BF_4] extraction, such absorption bands disappeared from the FTIR spectrum of the CER_{40ext} sample, while the intensities of the bands at 1558 cm^{-1} and 1356 cm^{-1} did not change significantly. It is noteworthy that the well-defined bands in the region of 1100—1000 cm^{-1} in the spectra of CER_{ext} and CER_{40ext} corresponded to the C—O—C bonds in the CER network structure. Consequently, the FTIR analysis confirmed the chemical inertness of IL to the CER network and the efficient removal of [HPyr][BF_4] from the CER matrix.

^{1}H NMR spectra of [HPyr][BF_4] and a typical sol fraction obtained after CER extraction are shown in Fig. 4.4. The resonance signals at 0.84, 1.28, 1.91,

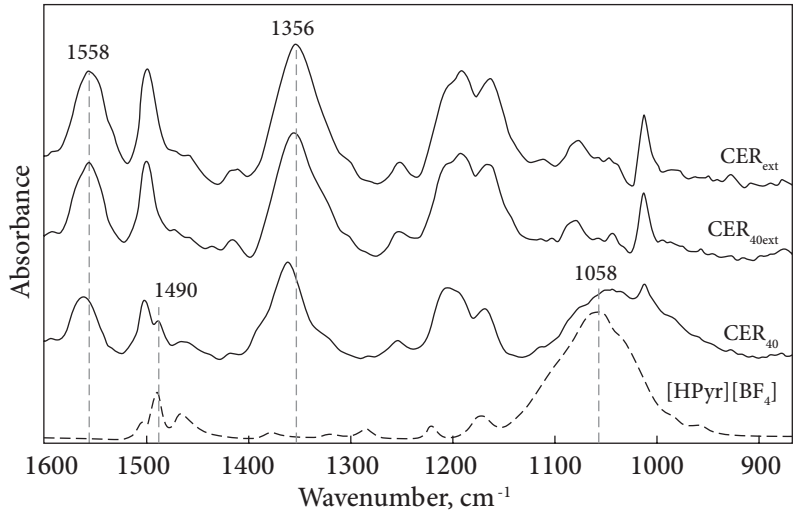

Fig. 4.3. FTIR spectra of ionic liquid [HPyr][BF_4] and typical CER networks before and after extraction

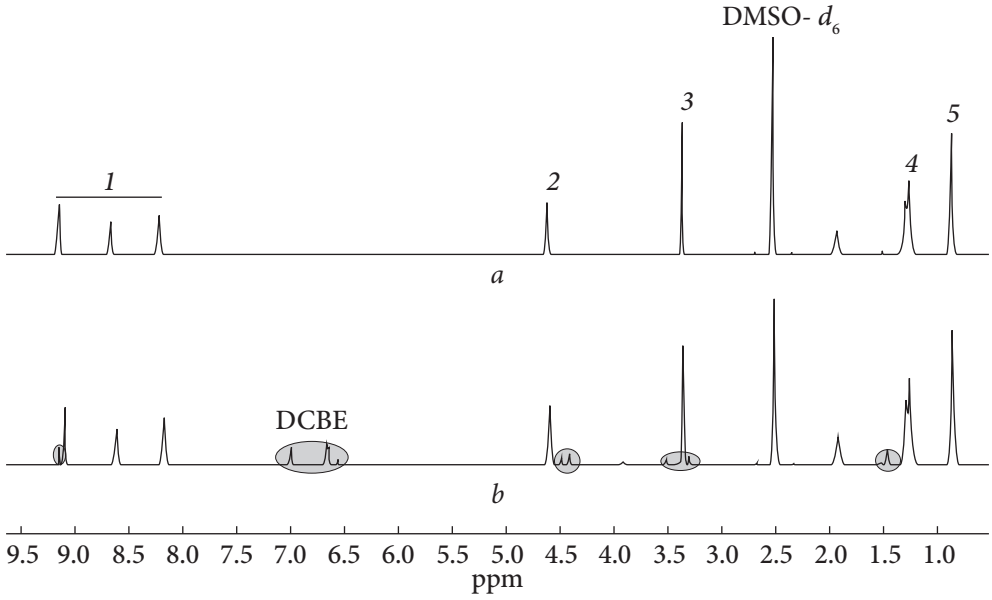

Fig. 4.4. ^{1}H NMR spectra of [HPyr][BF_4] (*a*) and sol fraction after CER_{40} extraction (*b*)

3.34, and 4.60 ppm can be assigned to the protons from -C_7H_{15}, and the presence of protons from pyridinium ring is observed with chemical shifts equal to 8.16, 8.60, and 9.08 ppm [76]. Obviously enough, the ^{1}H NMR spectrum of the sol fraction closely matches that of [HPyr][BF_4], only traces of unreacted DCBE and/or soluble low molar mass cyanurate fragments non-incorpora-

ted into CER network are observed in the interval of 6.62—7.08 ppm. Once again, this spectroscopic analysis confirms that [HPyr][BF_4] was undoubtedly removed from CER networks.

4.3. SEM, EDX, and DSC-based thermoporometry studies

Typical SEM images of CER films before and after extraction of [HPyr][BF_4] are presented in Fig. 4.5. As expected, both CER_{ext} and CER_{40} samples (Fig. 4.5*a*, *c*, respectively) exhibit compact and non-porous structures, whereas CER_{20ext} and CER_{40ext} samples (Figs. 5*b* and 4.5*d*, respectively) display a nanoporous structure with pore diameters ranging from 25 to 170 nm, depending on their CER/IL composition. Pore sizes generally increase and pore size distributions widen with increasing the porogenic solvent (*i.e.* [HPyr][BF_4]) content (Table 4.1) in the IL-filled CER precursors. The micrographs were carefully analyzed using the *ImageJ* software. Most pore area fractions fall in the range of 500 to 5000 nm^2 (Fig. 4.6), which corresponds to pore diameters (D_p) from ~25 to 80 nm. The quantity of larger pores (with pore area higher than 5000 nm^2, *i.e.* D_p > 80 nm) turned out to be negligible. The values of average pore diameters were found to be around 40, 60, and 65 nm for CER_{20ext}, CER_{30ext}, and CER_{40ext}, respectively (Table 4.1). It is noteworthy that the porosity ratio values as determined from SEM data are in excellent agreement with expected values, considering the complete removal of IL initial content.

Besides SEM micrographs, Fig. 4.5 also shows corresponding EDX spectra. As expected, the absence of B and F elements of [HPyr][BF_4] is observed in the porous samples studied, which confirms the complete extraction of IL from CER/IL precursor samples. Table 4.2 summarizes the experimental and theoretical values of element contents in the CER-based samples under study. Interestingly, both sets of values are in good agreement.

Table 4.1. **Main porosity characteristics for nanoporous CER-based films**

Porous films	SEM			DSC-based thermoporometry		
	Average pore diameter, nm	Pore size distribution, nm	Porosity	Average pore diameter, nm	Pore size distribution, nm	Total pore volume, $cm^3 \cdot g^{-1}$
CER_{20ext}	40	~25—100	0.18	45	~20—105	0.037
CER_{30ext}	60	~25—165	0.30	60	~20—175	0.120
CER_{40ext}	65	~25—170	0.39	60	~20—180	0.124

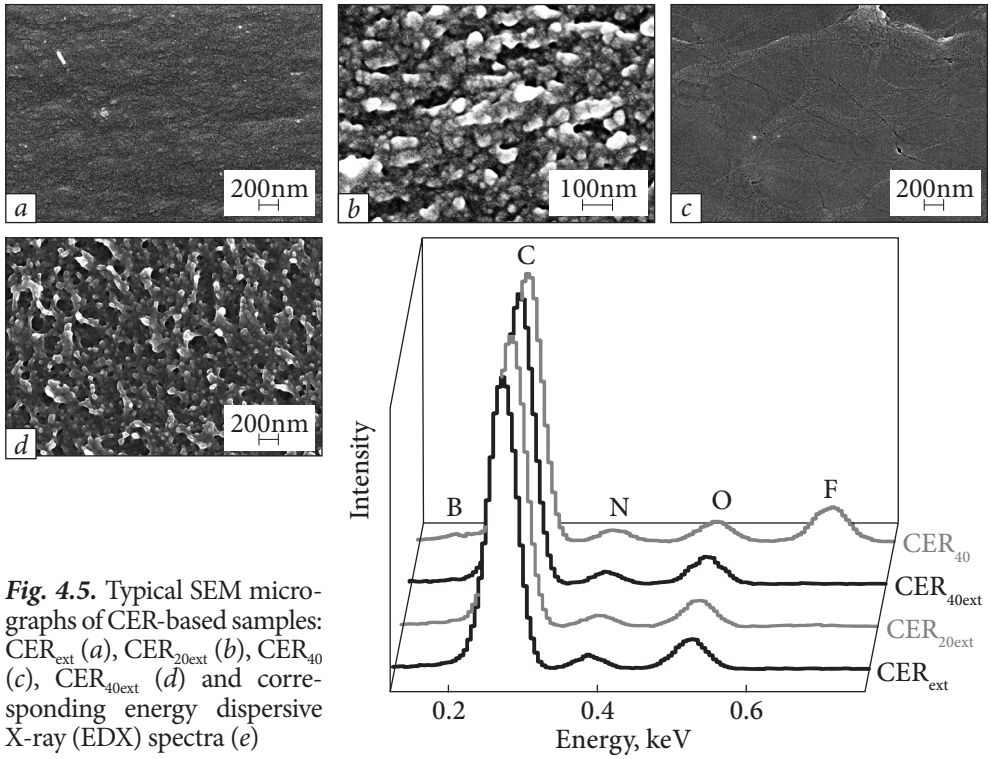

Fig. 4.5. Typical SEM micrographs of CER-based samples: CER_{ext} (*a*), CER_{20ext} (*b*), CER_{40} (*c*), CER_{40ext} (*d*) and corresponding energy dispersive X-ray (EDX) spectra (*e*)

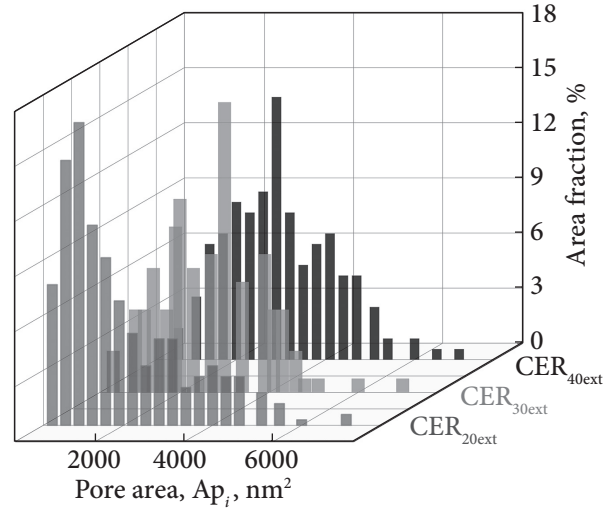

Fig. 4.6. Pore area distributions derived from SEM data for the nanoporous CER-based samples

The melting thermograms of water in nanoporous CER samples in the temperature region between –3 and 4 °C and the corresponding profiles of pore size distributions are given in Fig. 4.7*a*, *b*, respectively.

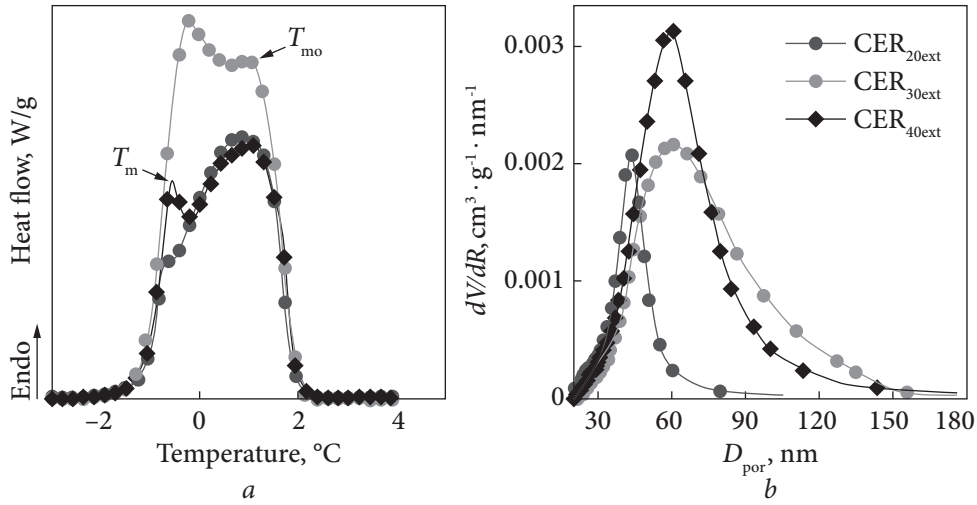

Fig. 4.7. DSC melting thermograms of water confined within the pores of nanoporous CERs (*a*) and the corresponding pore size distribution profiles (*b*)

Table 4.2. **Experimental and theoretical values of element contents in typical CER-based samples**

Samples	Element contents (wt%)									
	Experimental (EDX)					Theoretical (calculated)				
	C	N	O	F	B	C	N	O	F	B
CER_{ext}	76.0	12.0	12.0	0	0	76.2	11.1	12.7	0	0
CER_{20ext}	75.8	12.1	12.1	0	0	76.2	11.1	12.7	0	0
CER_{30ext}	76.8	11.5	11.7	0	0	76.2	11.1	12.7	0	0
CER_{40ext}	77.3	11.7	11.0	0	0	76.2	11.1	12.7	0	0
CER_{40}	67.1	9.0	7.1	14.4	2.4	69.3	9.0	7.7	12.1	1.8

In the thermograms of CER samples, two endothermic peaks were detected: one with a maximum, T_m, between –2 and 0 °C corresponding to the melting of water constrained within the film pores, and the other with a maximum, T_{m0}, between 0 and 2 °C related to the melting of bulk water (Fig. 4.7*a*). It was found that pore size distributions for the porous CER-based films were in the range of ~20—180 nm (Fig. 4.7*b*), and their average pore diameters were around 45—60 nm, depending on the initial IL content in the CER precursors (Table 4.2). It is noteworthy that an increase in the [HPyr][BF_4] content resulted in increasing pore diameters and a broadening pore size distributions, along with increasing pore volumes. These results are in close agreement with those obtained from SEM analysis. The minor discrepancies between the pore characteristics

determined by both techniques can be explained by the difference between real pore shapes of CER structures and circular ones used for the mathematical data processing in SEM analysis.

4.4. Thermal stability of CER-based films by TGA

The influence of [HPyr][BF_4] on the thermal stability of nanoporous CER networks has been investigated by the authors using TGA [76]. Mass loss and corresponding derivative curves are presented in Fig. 4.8 and the main corresponding data are summarized in Table 4.3. For the neat CER sample, the first step of the intensive mass loss was observed in the temperature range of ~390—490 °C which was associated with the degradation of the skeleton of crosslinked CER network, and the second step was observed at higher temperatures with a small mass loss. For pure [HPyr][BF_4], we could observe a single degradation stage in the temperature interval from ~350 to 438 °C with an intense mass loss of ~94%.

In contrast to pure CER, the thermal decomposition of nanoporous CER films was more complex and involved more stages, especially in the lower temperature range. A slight initial mass loss of ~2—5% below 280 °C might arise from the removal of entrapped moisture within the CER network. The first decomposition step for CER_{20ext}, CER_{30ext}, and CER_{40ext} really occurred in the temperature range of 285—395 °C with a mass loss of ~14—17% corresponding to the degradation of porous and defective network regions of CER structures. Near 400 °C the onset temperature of intensive degradation with higher mass loss (~29—30%) occurred, which can be attributed to the destruction of triazine cycles of CER skeleton. The overall decomposition led to 40—42% char residues. Surprisingly, the thermal stability of the nanoporous CER-based networks decreased compared to that of pure CER, although they had the same chemical structure: the temperature for the onset of intensive degradation (T_{d1}) and 50% mass loss ($T_{d50\%}$) decreased respectively from 425 °C and 694 °C for the CER sample to 395 °C and 503 °C for the CER_{40ext} sample (Table 4.3). The higher the initial [HPyr][BF_4] content in the CER precursors, the lower the thermal stability of the nanoporous films obtained. Nevertheless, the temperatures of maximum mass loss (T_{dmax}) are nearly identical for the CER, CER_{20ext}, CER_{30ext}, and CER_{40ext} films. The presence of IL in the CER_{40} sample led to a significant reduction of T_{dmax} by 50 °C and one such film degraded in a single step. One could suppose that one such strong dilution (40 wt% of IL) hindered the DCBE polycyclotrimerization, as the probability of the elementary reaction step might decrease, *i.e.* the reaction of three cyanate groups together to afford the formation of cyanurate rings. The presence of DCBE monomer molecules or other

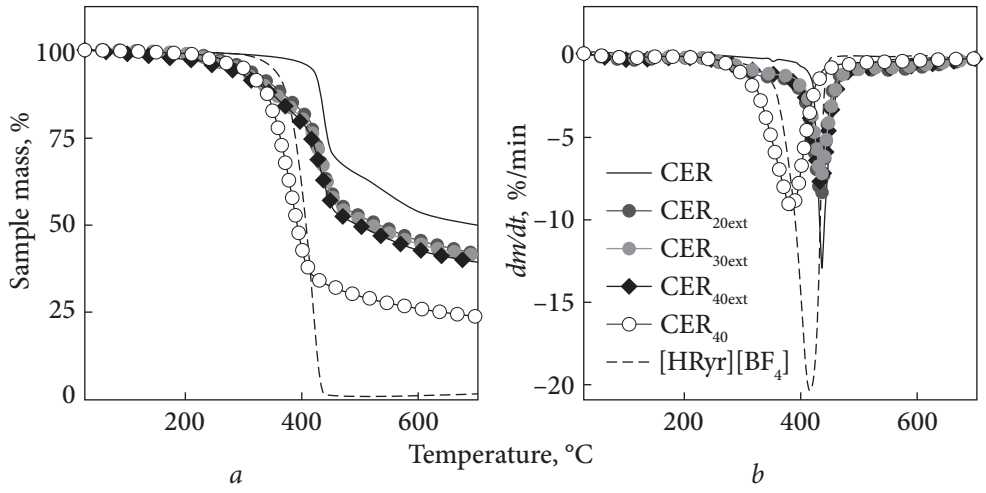

Fig. 4.8. Mass loss (*a*) and corresponding derivative (*b*) curves as determined by TGA for [HPyr][BF_4] and typical CER-based films

Table 4.3. **TGA data obtained for CER-based networks and pure [HPyr][BF_4]**

Samples	T^{a}_{d1}, °C	$T^{b}_{d\,max}$, °C	$T^{c}_{d50\%}$, °C	Mass loss at $T_{d\,max}$, %	Char residue, %
CER	425	435	694	16	50
CER_{20ext}	399	435	538	32	42
CER_{30ext}	396	434	528	33	42
CER_{40ext}	395	435	503	35	40
CER_{40}	340	385	393	42	25
[HPyr][BF_4]	376	416	407	67	2

[a] T_{d1}: onset temperature of intensive degradation as determined by value for intersection of the tangents to curve at the first inflection point; [b] $T_{d\,max}$: temperature of maximal degradation rate; [c] $T_{d50\%}$: temperature of 50% mass loss.

intermediate oligomeric molecules that were not incorporated into the CER network (as confirmed by ^{1}H NMR spectrum of the sol fraction, see Fig. 4.4), along with IL, might drastically decrease the T_{dmax} value of CER_{40} sample. After extraction of all the soluble fragments, the final nanoporous CER_{40ext} sample was characterized by a high T_{dmax} value comparable to that of the other nanoporous materials obtained (T_{dmax} = 435 °C).

Removing IL from CER precursory networks afforded nanoporous films, which degraded in two steps corresponding to the destruction of the defective CER network at lower temperatures and the degradation of the regularly crosslinked network regions with $T_{d\,max}$ equal to that of the nonporous CER

analog. Consequently, applying [HPyr][BF_4] as a porogen reduced the thermal stability of resulting nanoporous films compared to that of the neat CER probably, due to the formation of less regular CER structures.

4.5. Conclusions

Novel nanoporous film materials based on thermostable polycyanurates generated *in situ* by polycyclotrimerization of DCBE in the presence of ionic liquid [HPyr][BF_4] have been developed. Nanoporous CER-based films were obtained by extraction of the ionic liquid from CER networks. Complete IL removal was confirmed by the determination of gel fraction contents, FTIR, ^{1}H NMR, and EDX spectroscopic analyses. SEM and DSC-based thermoporometry were used as complementary techniques for nanopore characterization. Depending on the IL porogen content, the average pore diameter was found in the range of 45—60 nm with pore size distributions of ~20—180 nm. It is also noteworthy that an increase in the [HPyr][BF_4] content resulted in increasing pore diameters and broadening pore size distributions. The TGA curves showed high thermal stability of the nanoporous films obtained with an onset decomposition temperature of near 300 °C. It should be stressed that the synthesis of CERs in the presence of IL was carried out without using any additional solvent or specific catalyst, the ionic liquid being highly thermostable and potentially being utilized repeatedly.

CHAPTER 5

STRUCTURE–PROPERTY RELATIONSHIPS FOR NANOPOROUS THERMOSETTING CYANATE ESTER RESINS VIA INCOMPLETE MONOMER CONVERSION

5.1. Synthesis

The synthesis of CER-based polymer networks (polycyanurates, PCN) is generally carried out by polymerizing dicyanate ester monomers using a step-by-step heating procedure [3, 4, 78]. Each curing step brings a higher temperature, and subsequently, a higher conversion degree for the cyanate groups of dicyanate monomer. The gel point at conversion around 50—60 % is reached, and curing promotes simultaneous increase in the conversion degree, crosslink density, and glass transition temperature of the CER network formed. Such a stepwise process eventually results in the generation of rather regular and fully crosslinked structures. A reaction scheme associated with the polycyclotrimerization of pure dicyanate monomer (DCBE) leading to the network formation is shown in Fig. 3.1. Therefore, the curing rate and crosslink density as well as the final properties of the CER synthesized depend on the temperature-time schedule. However, the polycyclotrimerization process is rather slow, and it is usually difficult to attain high degrees of conversion. Hence, curing catalysts, *e.g.* complex catalysts combining transition metal salts or chelates with alkylphenols or other active hydrogen sources, are widely used to reach quasi-completion [3, 4].

DCBE was mixed with the catalytic complex (a mixture of cobalt acetyl acetonate (0.017 phr) and nonylphenol (2 phr) to CER amount), poured into a PTFE-coated mold, and then heated according to different step-by-step schedules. The code of samples prepared and the corresponding temperature-time schedules are given in Table 5.1.

The thickness of as-obtained CER films was around 150 μm. Porous structures were generated via acetone extrac-

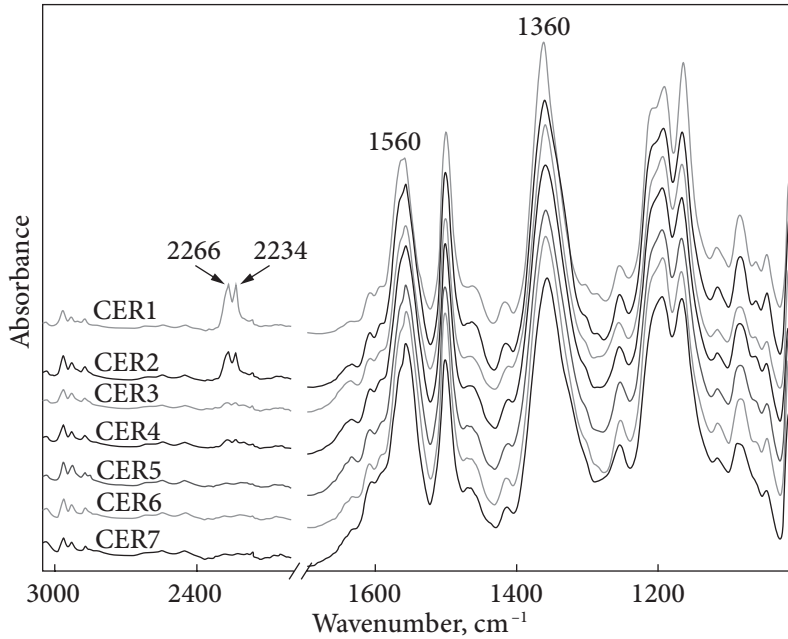

Fig. 5.1. FTIR spectra of CER samples synthesized with varying conversion of cyanate groups. The spectra are shifted vertically for the sake of clarity

Table 5.1. **Temperature-time schedules for synthesis of CERs with controlled monomer conversion**

Sample code	Temperature step, T_i, °C	Duration of curing at T_i, h	Total polymerization time, h
CER1	150 + 180	5 + 0.5	5.5
CER2	150 + 180	5 + 1.5	6.5
CER3	150 + 180	5 + 3	8.0
CER4	150 + 180 + 210	5 + 3 + 1	9.0
CER5	150 + 180 + 210 + 230	5 + 3 + 1 + 1	10.0
CER6	150 + 180 + 210 + 230 + 250	5 + 3 + 1 + 1 + 1	11.0
CER7	150 + 180 + 210 + 230 + 250 + 270	5 + 3 + 1 + 1 + 1 + 0.5	11.5

tion of partially cured CER films using a Soxhlet apparatus for 16 h followed by drying under vacuum up to constant mass. Below, index in sample codes will refer to the extracted samples.

To acquire information on conversion degree of cyanate groups in the CER films synthesized, FTIR studies were carried out. The FTIR results for the CER samples after each temperature step showed the presence of strong absorption

bands at 1360 and 1560 cm^{-1} arising from stretching vibrations of cyanurate rings (triazine and phenyl-oxygen-triazine bands, respectively) (Fig. 5.1). On the other hand, in the spectra of the CER samples with the lowest temperature of the final heating step (Table 5.1 CER1–CER3 samples), the bands with maxima at 2266 and 2234 cm^{-1} associated with stretching vibrations of cyanate (O—C≡N) groups are present, thus denoting the incompletion of polycyclotrimerization reaction. After curing at 210 °C (CER4 sample), some residual cyanate groups of CER monomer are observed. In contrast, for the samples with higher final heating temperatures (CER5-CER7 samples), these bands were hardly detected in the corresponding FTIR spectra and a magnification of the spectral region between 2400 and 2100 cm^{-1} was needed to clearly detect the traces of O—C≡N groups and quantify monomer conversion. Therefore, one can anticipate that the higher the curing temperature and/or the duration of curing, the higher the conversion degree of cyanate groups and the higher the crosslink density of the resulting CERs.

However, after the extraction of unreacted monomer and chemically non-incorporated soluble CER fragments from the rigid networks, the generation of porous structures in all the cases is expected. FTIR analysis of extracted samples gave evidence of the absence of absorption bands corresponding to the non-reacted OCN groups at 2266—2234 cm^{-1}. On the opposite, the residual monomer and aforementioned uncrosslinked fragments were found in the sol fractions, as expected.

5.2. Determination of conversion degree and gel fraction content

The time dependence of DCBE conversion as determined from FTIR measurements showed that the degree of conversion increased from ~79 % for the CER1 sample up to 96% for the CER7 one (Fig. 5.2). Moreover, each heating step brought close to the linear growth of cyanate conversion. The additional heating of CER samples to 180—210 °C resulted in increasing the conversion degree by ~9%, while the subsequent stages of heating (230—270 °C) for 2.5 h allowed conversion to be additionally increased by only ~8%. According to the literature data [3], it was impossible to reach the highest conversion of OCN groups at relatively low temperatures since at each curing stage, a CER system with limited crosslink degree could be achieved. As a matter of fact, to allow the polymerization process to be continued, the curing temperature had to be increased over the T_g of the growing network [78]. By such step-by-step curing, nearly complete monomer conversions associated with high crosslink degrees could be achieved for CER systems.

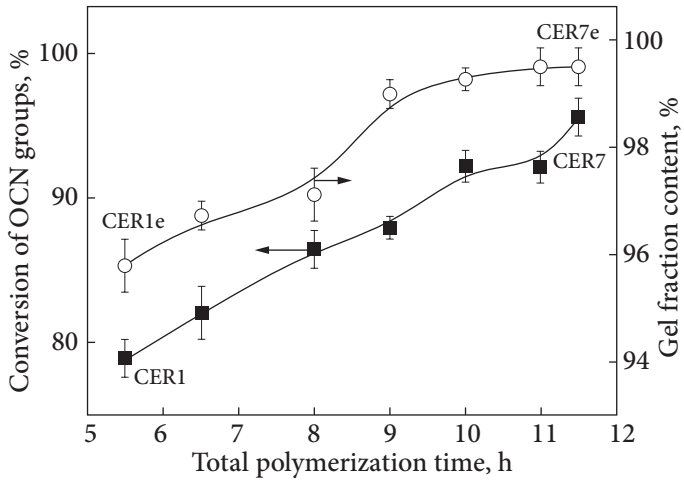

Fig. 5.2. Time dependence of cyanate conversion and gel fraction content after extraction for the CER samples synthesized

The conclusions inferred from the FTIR studies were confirmed by the results of gel fraction determination (Fig. 5.2). The gel fraction content appeared to be high, *i.e.* ranging from 95.8 % for the CER1e sample up to 99.5 % for the CER7e network. This can be explained by the presence of a highly efficient catalytic complex providing a high curing degree of CER monomer, even after short-term treatment at 180 °C. Therefore, high thermal stability of nanoporous CER samples along with a slight variation in porosity characteristics can be achieved. Similar time dependences of the gel fraction and the conversion degree were noticed. Thereby, it can be assumed that, after reaching 99.5 % gel fraction, an almost completely cured CER network would be generated. The corresponding sol fraction content would tend to zero, thus resulting in a significant decrease in the created porosity and even the formation of a non-porous material after the further extraction procedure.

5.3. Morphology and porosity parameters

The morphology and porous structure of all extracted CER films produced were investigated by SEM (Figs 5.3 and 5.4) and by DSC-based thermoporometry (Fig. 5.5). The main porosity characteristics for typical samples are summarized in Table 5.2.

First, non-extracted CER samples do not exhibit any porous structure, as shown in our previous reports [26, 40]. As expected, for the CER1 sample (with the lowest final degree of OCN conversion) after extraction, a nanoporous structure with the highest porosity equal to 7.4 % was found (cf. Fig. 5.3 and Table 5.2 CER1e sample). After extraction of the other CER samples with higher final conversion of OCN groups, nanoporous structures could also be created (Fig. 5.3 CER6e and CER7e samples); however, the porosity decreased

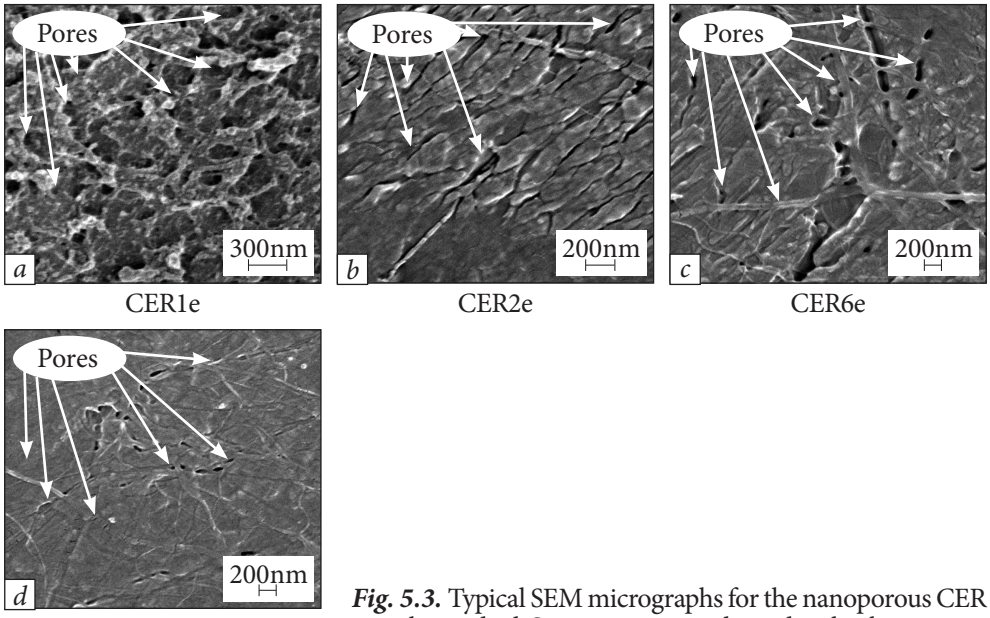

Fig. 5.3. Typical SEM micrographs for the nanoporous CER samples studied. Some pores are indicated with white arrows

down to 4.9% for CER3e, and even to 2.8% for the CER7e sample. According to Zhu *et al.* [79], one can assume that the occurrence of nanopores in CER samples is due to not only the removal of non-embedded CER fragments but also the own intrinsic porosity associated with the triazine framework. The average pore sizes as measured by SEM varied from 10 to 230 nm for all the CERe samples studied.

Consequently, varying the temperature-time schedule of CER curing, followed by an extraction procedure, allows for tunable variation of the main porosity characteristics of the CERe films, namely pore sizes and their distribution as well as the porosity value.

The micrographs obtained were carefully analyzed using the *ImageJ* software. As seen, most of the area fractions are occupied by pores ranging from ~60 to 2000 nm^2, which corresponds to the diameters of circle-shaped pores (D_p) from ~10 to 50 nm (Fig. 5.4). The quantity of larger pores (with pore area > 5000 nm^2, *i.e.* D_p > 80 nm) appeared to be negligibly small. The average pore diameters $D_{p(av)}$ were found to be ~20—45 nm for all the CERe films investigated (Table 5.2). Moreover, the higher the curing temperature, the lower the pore sizes and the narrower the pore size distribution in the final nanoporous CERe sample. The increase in the synthesis duration resulted in decreasing porosity (Table 5.2), which can be explained by the transformation of a loose CER network into a denser structure at a higher conversion degree of OCN groups.

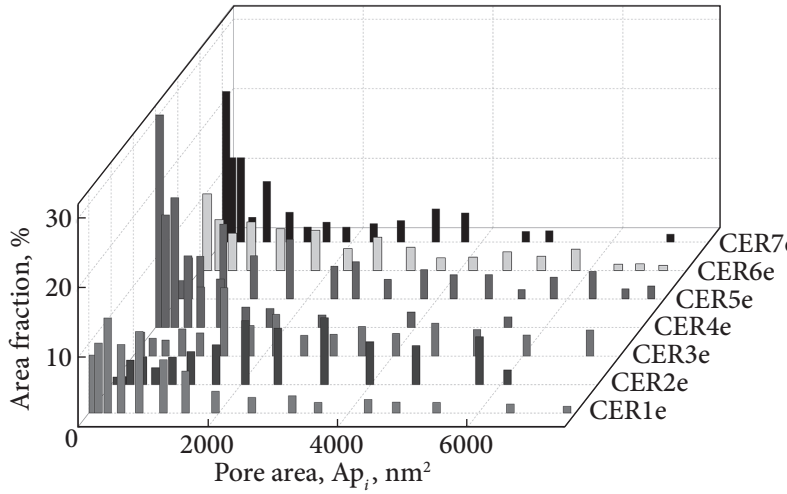

Fig. 5.4. Pore area distributions derived from SEM data (*ImageJ analysis*) for the nanoporous CER samples studied

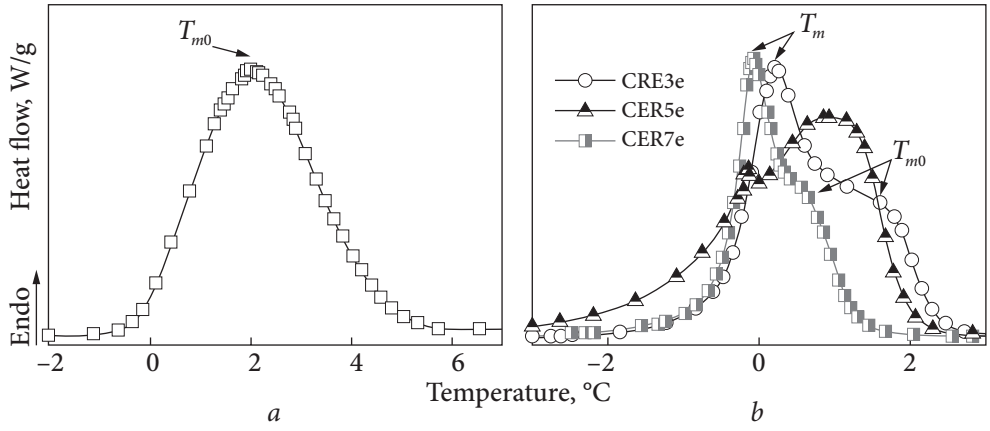

Fig. 5.5. Typical DSC melting thermograms of (*a*) bulk deionized water and (*b*) water confined within the pores of different nanoporous CER structures investigated

The occurrence of a nanoporous structure in the CER1e-CER7e samples was confirmed by DSC-based thermoporometry measurements (Figs. 5.5 and 5.6 Table 5.2). In contrast to the single melting of crystallites in the bulk water (Fig. 5.5*a*), two well-defined overlapping endothermic peaks indicating melting of the frozen bulk water (T_{m0}) and crystallites confined within the pores (T_m) are distinctly seen in the DSC thermograms of the porous CER samples studied (Fig. 5.5*b*). Finally, pore diameters (D_p) and pore size distributions (dV/dR) were also determined (Fig. 5.6).

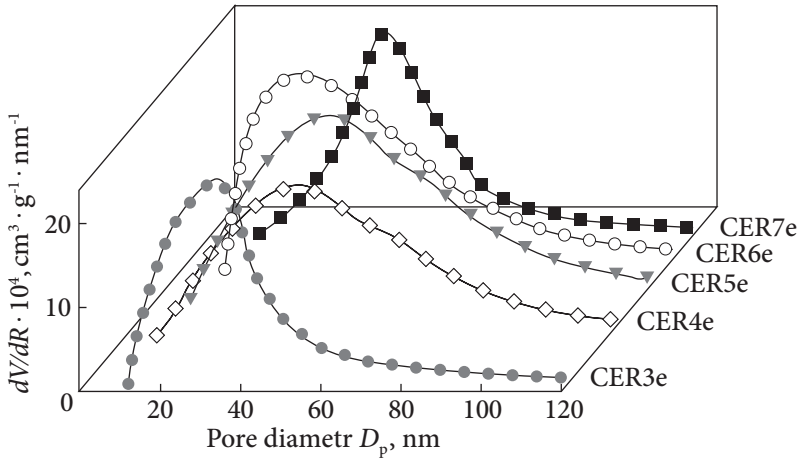

Fig. 5.6. Typical pore size distribution profiles as determined by DSC-based thermoporometry for nanoporous CERs studied

Table 5.2. **Main porosity characteristics of several nanoporous CER films as determined by SEM and DSC-based thermoporometry**

Sample code	SEM [a]				DSC-thermoporometry [b]	
	Average pore diameter, $D_{p(av)}$ (nm)	Pore size distribution, D_p (nm)	Pore circularity (a.u.)	Porosity, %	Average pore diameter, $D_{p(av)}$ (nm)	Pore size distribution, D_p (nm)
CER1e	45	10—220	0.83	7.4	45	10—160
CER3e	35	15—230	0.85	4.9	30	10—120
CER5e	30	10—220	0.80	3.0	40	10—100
CER7e	20	10—125	0.90	2.8	30	15—165

[a] The values calculated using *ImageJ 1.48v* software; [b] The values determined from DSC thermograms

The results obtained by DSC-thermoporometry clearly show that pore characteristics are in good agreement with those determined by SEM (Table 5.2). The minor discrepancies can be explained by the difference between pore shapes of the real CER structures and those used for the mathematical data processing in SEM analysis.

Table 5.2 and Fig. 5.6 also demonstrate that changes in synthesis conditions bring a slight narrowing in pore size distribution and an insignificant variation in average pore diameters, due to a possible increase in CER shrinkage during synthesis. Therefore, the structure of the CER samples after extraction can be considered nanoporous, and their porosity can be controlled to some extent by varying the temperature and duration of high-temperature polymerization.

5.4. Thermal characterization of nanoporous CER networks

Previous studies on the thermal stability of crosslinked CERs showed that the thermal degradation process of a completely cured CER consisted of two main degradation stages with maxima at ~420—430 °C and ~540—560 °C [55—57]. Fig. 5.7 and Table 5.3 represent the typical TGA results for the nanoporous CER samples under investigation. The data obtained show that the temperatures for 5 % ($T_{d5\%}$) and 40 % ($T_{d40\%}$) mass losses increase respectively from 199 °C and 466 °C for the CER1e sample up to 326 °C and 503 °C for the CER7e sample (Table 5.3).

The generation of a nanoporous structure also resulted in the appearance of a slight mass loss (~1—2%) at ~86—90 °C corresponding to the removal of adsorbed moisture (not shown here). The maximal degradation rate for the CER1e-CER7e samples was observed at $T_{d\ max}$ ~426—432 °C due to the breakage of bonds between phenyl and triazine cycles, followed by the degradation stage with the maximal rate at $T_{d\ max}$ ~543—547 °C which testifies the intensive decomposition of triazine cycles of CER skeleton (Fig. 5.7). Char residues for all the samples investigated varied from 44 to 48 %.

It is noteworthy that a much lower thermal stability was found for the nanoporous CER samples cured at 180 °C, which obviously reflects the imperfection of the CER structure formed due to lower conversion degrees of cyanate groups of DCBE as compared to all other CER samples synthesized. Therefore, one can suppose that DCBE monomers as well as CER fragments incorporated into the CER frameworks by at least one reactive group strongly affect the thermal behavior of the final materials.

As noted above, there are different degrees of completion of the polycyclotrimerization reaction for all the nanoporous CER samples. Therefore, along with the characterization of the glass transition behavior for all the extracted

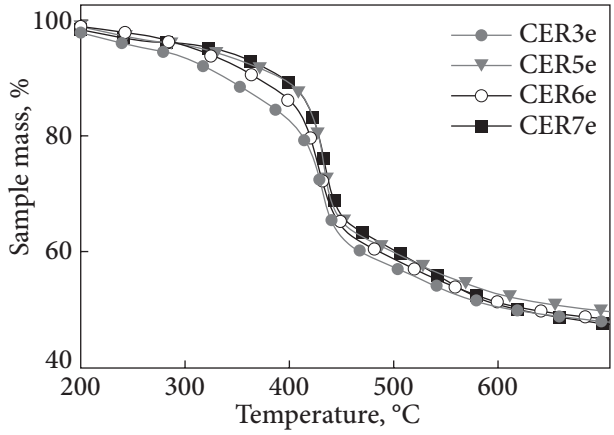

Fig. 5.7. Typical mass loss curves from TGA for the nanoporous CER samples under investigation

CERs, the possibility of a post-curing reaction at temperatures above the glass transition was also examined.

Fig. 5.8 discloses the DSC results for the nanoporous CERs studied, and Table 5.4 summarizes their main thermal characteristics as determined by DSC. The DSC thermograms reveal the presence of an exothermic transition starting from ~190 to ~290 °C depending on the sample, which corresponds to the additional curing (post-curing) of the nanoporous CERs produced. Moreover, the lower the final temperature of synthesis, so in turn, the lower the conversion degree in the final CER (Table 5.1 and Fig. 5.2), the lower the onset temperature of post-curing ($T_{postcur}$), and the higher the exothermic effect. Such a tendency can be explained by the generation of a more rigid CER structure with higher conversion of cyanate groups (Fig. 5.2) and crosslink density in the CER5e-CER7e samples as compared to the "less cured" CER1e-CER4e networks formed at lower temperatures (Table 5.2). However, for samples with a quite high degree of conversion (CER5e-CER7e samples), a slight post-curing effect at $T_{postcur}$ ~260—290 °C was still recorded. The negligibility of the mass loss at $T_{postcur}$ for all the samples investigated, as determined by TGA, precluded the possible attribution of the effect observed to any degradation process.

The same dependence of the main glass transition characteristics on the final curing temperature in a sequence from CER1e to CER7e samples was also noticed (Table 5.4). The glass transition behavior was expressed by a sharp endothermic transition with an onset temperature ($T_{g\,onset}$) ranging from 167 °C

Table 5.3. **Main TGA data on characteristic nanoporous CER films studied**

Sample	$T_{d5\%}$ [a], °C	$T_{d40\%}$ [a], °C	$T_{d\,max}$ [b], °C	Mass loss at $T_{d\,max}$, %	Char residue, %
CER1e	199	466	426	23	44
CER3e	272	471	431	27	46
CER5e	313	487	431	23	48
CER6e	316	499	431	26	47
CER7e	326	503	432	23	47

[a] $T_{d5\%}$ and $T_{d40\%}$ are temperatures for % and 40 % mass losses, respectively; [b] $T_{d\,max}$, temperature of maximal degradation rate

Table 5.4. **DSC data for the nanoporous CER samples investigated**

Sample code	$T_{g\,onest}$, °C	T_g, °C	$T_{postcur}$, °C	Sample code	$T_{g\,onest}$, °C	T_g, °C	$T_{postcur}$, °C
CER1e	167	171	190	CER5e	223	235	262
CER2e	182	187	203	CER6e	224	237	264
CER3e	185	199	209	CER7e	227	246	289

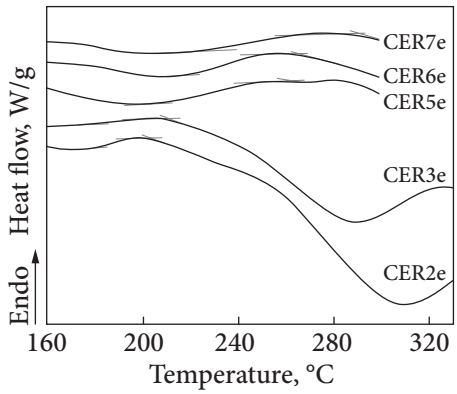

Fig. 5.8. Typical DSC thermograms for the nanoporous CER samples investigated

for the CER1e sample to 227 °C for the CER7e network (Fig. 5.8). As seen, the glass transition temperature, T_g, regularly increases from 171 °C for CER1e to 246 °C for CER7e samples, due to the formation of a much denser CER structure in the latter. The results obtained correlate with the FTIR and TGA data. Therefore, a simple, easy-handling, and effective method for generating well-defined nanoporous crosslinked CER thin films through network formation with incomplete conversion of cyanate groups, followed by an extraction procedure, has been developed with a significant loss in thermal characteristics compared to those of non-porous high-performance CER thermosets.

5.5. Conclusions

The present investigation reveals the possibility of generating nanoporous film materials based on thermosetting cyanate ester resins by merely varying the degree of completion associated with the polycyclotrimerization of dicyanate monomer. A series of nanoporous CER films obtained by this incomplete conversion technique were thus synthesized. The nanoporous structures were generated by the extraction of unreacted monomer or/and soluble oligomeric and/or polymeric CER fragments non-incorporated into the growing CER networks. Depending on the temperature-time schedule of CER synthesis, the peculiarities of porous structures as well as the thermal features of nanoporous CER samples were different. It was established that the lower the conversion degree, the higher the porosity of nanoporous structures. TGA studies on nanoporous networks have shown that their thermal stability strongly depends on the final curing temperature of network synthesis and its duration, considering that the conversion degree and crosslinking density of CERs increase while temperature and time rise. It is noteworthy that the thermal stability decreases significantly for nanoporous CERs cured at 180 °C due to lower conversion degree as compared to the other samples cured at higher temperatures.

CHAPTER 6

THERMALLY STABLE NANOPOROUS CYANATE ESTER RESIN/LINEAR POLYURETHANE GRAFTED SEMI-INTERPENETRATING POLYMER NETWORKS CREATED BY IRRADIATION TECHNOLOGIES

6.1. Introduction

The pioneering studies by Fleischer and co-authors on track etching in thin sheets of materials [80, 81] exploded a huge trend in further development of physics and chemistry of porous polymer materials, in particular the generation of novel track-etched membranes (TMs), also known as Nuclepore membranes [82—84].

Nowadays, the track-etching technology is extensively used on an industrial scale for producing multipurpose polymer-based membranes for micro- and ultrafiltration, gas and liquid separation, and water purification [82—86], as well as in the areas of medicine, biotechnology, and genetics [87]. The essence of the technology lies in the irradiation of thin polymer films with charged particles of high energy (ions, protons, α-particles, γ-irradiation, etc.) or with fragments of heavy nuclei fissions (argon, krypton, xenon, uranium, etc.) resulting in radiation degradation of macromolecules and formation of damaged channels (*i.e.*, so-called "tracks") in the materials. During further etching of the irradiated films with solutions of alkalis, acids, oxidants, and other chemical reagents, the material fragments are washed out from the tracks, and a regular through porosity is formed [82—94]. To generate track-etched membranes based on the most known polymers, the etching process usually does not exceed 30—90 min. The resulting TMs are characterized by an extremely regular porous structure with well-defined pore size, pore shape, and density, ensuring the required controllable transport and retention characteristics [83, 84, 94—96]. Moreover, the nuclear technology developed is quite universal and can be widely applied to most polymers and polymer blends [82—87].

Depending on the chemical structure and initial thickness of the polymer film and on the irradiation and etching conditions (type of irradiation, source applied, temperature, atmosphere, and humidity during irradiation, etchant composition, component concentrations, etc.), the resulting porous structure and physicochemical properties of the final material can be varied in a very wide range. To change pore size and shape, pore size distribution, and correspondingly, the final permeability of the membrane produced, an additional sensitization of the irradiated film can be fulfilled, prior to etching. Sensitization is carried out through exposure to ultraviolet, plasma, or γ-irradiation, additional temperature treatment, etc., thus resulting in increasing defectiveness of macromolecules and growth of the etching rate inside the tracks formed [82—84, 92]. Usually, the preliminary sensitization procedure allows for improving pore shape and pore size distribution, increasing permeability coefficient along with easing etching conditions (decreasing etching temperature and duration, concentration of etching solution, etc.) [82, 96].

In addition to conventional polyethylene, poly(vinylidene fluoride), polypropylene, and polyester-based TMs [85, 89], numerous efforts have been made to develop similar products based on high-temperature polymers, such as poly(ethylene terephthalate), polyamides, polyimides, etc. over the last decades [87, 94—96]. However, producing TMs based on high-performance crosslinked polymers remains largely unexplored yet.

To the best of our knowledge, our research results are among the first attempts to produce track membranes from nanoporous materials on the basis of high-performance thermosetting polymers. Such materials are usually characterized by high glass transition temperature and temperature of degradation (in both inert and air atmospheres) of water resistance and resistance to aggressive media (acids, alkalis, etc.). Indeed, crosslinked cyanate ester resins (CERs) have higher thermal characteristics compared to PE, PET, and polyesters, much better water resistance compared to polyamides, and easier processing compared to polyimides (CER-based films can be produced by reactive forming with no toxic solvent). Usually, to improve the elastic properties of film-forming materials based on thermosetting polymers, some amount of a linear polymer with suitable elasticity is added. In our previous publications [17, 78], we have studied various combinations of CERs with some monomers, oligomers, and polymers, as well as the effect of the modifier type, chemical structure, and concentration on the basic physical properties of the modified CER-based networks. Semi-IPNs from cyanate ester resin/linear polyurethane compositions have appeared to be the most suitable as they improve mechanical properties without any significant loss in thermal stability.

Earlier, we published the pioneering results of our successful attempt to develop a highly porous structure in hybrid polymer networks of cyanate ester

resins modified with 30 wt% of poly(tetramethylene glycol) or poly(ε-caprolactone), which were chemically incorporated into the growing polycyanurate network. The encouraging results showed the potential of such an innovation [97]. Accordingly, the present detailed investigation is focused on the generation of track-etched membranes based on promising high-performance grafted semi-IPNs formed by CERs and linear polyurethane (LPU) possessing high thermal and chemical resistance, low dielectric loss, and moisture absorbance as potential membranes for multipurpose applications, especially in extreme conditions.

6.2. Synthesis of CER/LPU grafted semi-IPNs and generation of porous structure

The melt of DCBA (or DCBE) at $T \approx 100$ °C was mixed with co-catalysts, *i.e.* cobalt acetylacetonate (0.17 phr) and nonylphenol (2 phr), followed by degassing of the mixture under vacuum for $\tau \approx 5$ min at $T \approx 100$ °C. 10 wt% of LPU was then dissolved completely in the melt of DCBA (or DCBE). The mixture was poured into a PTFE-coated mold. The curing cycle consisted of three sequential stages: 5 h at 150 °C, 3 h at 180 °C, and 1 h at 210 °C. Finally, the CER-A/LPU and CER-E/LPU grafted semi-IPNs derived from DCBA and DCBE, correspondingly, were synthesized. The thickness of all the CER-based films was around 30—50 μm.

Our previous studies showed that the introduction of 30 wt% of a thermoplastic modifier and the final curing at 180 °C does not provide the desired mechanical strength of the resulting porous films after etching [17]. Therefore, then we involved a more effective catalytic complex along with increasing the final curing temperature up to 210 °C and decreasing the modifier amount to 10 wt%.

Irradiation. The CER-based films obtained were irradiated with α-particles of 27.2 MeV using a Cyclotron U-120 device (Institute of Nuclear Research, Kyiv). The density of α-particles that passed through the samples was varied from 2.65×10^{10} to 5.53×10^{10} particles/cm^2. In the technology developed, the deviation of holes (cylinders) from the vertical direction does not exceed 8—12 deg depending on the film thickness and the polymer nature. Note that the tracks were end-to-end, which was confirmed by the sensors detecting the same number of α-particles that entered and exited from the opposite side of the polymer film. Additionally, this fact was confirmed by SEM measurements of the irradiated films from both sides (not shown here).

Sensitization. To increase the etching rate, additional sensitization of some of the irradiated samples was implemented, prior to etching. The sensitization

Table 6.1. **Sample codes and pore generation conditions**

Sample code	Pore generation conditions		Sample code	Pore generation conditions	
	α-irradiation / γ-sensitization	Etching time, τ (min)		α-irradiation / γ-sensitization	Etching time, τ (min)
CER-A/LPU$_{\tau 1}$	+ / –	30	CER-A/LPU$_{\tau 2}$	+ / –	180
CER-E/LPU$_{\tau 1}$	+ / –	30	CER-E/LPU$_{\tau 2}$	+ / –	180
CER-A/LPU$_{\gamma,\tau 1}$	+ / +	30	CER-A/LPU$_{\gamma,\tau 2}$	+ / +	180
CER-E/LPU$_{\gamma,\tau 1}$	+ / +	30	CER-E/LPU$_{\gamma,\tau 2}$	+ / +	180

stage was performed by γ-irradiation at 1.4 kGy for ~17 min. All sample codes of sensitized samples have a subindex.

Etching. After irradiation, sensitized and non-sensitized films were etched using two different approaches named as a short-term and a long-term etching. During the short-term etching procedure, polymer films were treated with a solution of 5% KOH in ethanol at T ~70 °C and mixed with a magnetic stirrer for 30 min (sample code has subindex τ1), whereas during the long-term etching procedure, polymer films were etched at the same conditions for 180 min (sample code has subindex τ2). All the porous polymer films obtained were neutralized with 0.1 M HCl and then washed and dried up to constant mass. Finally, two series of porous film materials were obtained; their sample codes and corresponding pore generation conditions are given in Table 6.1.

Earlier, a series of hybrid materials based on CER networks and LPU were synthesized [17, 78], and their structure and segmental dynamics within –133—327 °C were studied by FTIR, small-angle X-ray scattering (SAXS), DSC, and laser-interferometric creep rate spectroscopy (CRS) techniques. The hybridization effect via the chemical interaction of cyanate/urethane groups was evidenced in these systems, which led to the formation of completely homogeneous structures on a scale of >2 nm, irrespective of material composition. At the same time, the combined CRS/DSC analysis allowed for revealing a pronounced nanoscale (<2 nm) dynamic heterogeneity within or below extraordinarily broad glass transition for these single-phase materials [17]. The existence of only stage of thermal-oxidative degradation for the CER/LPU compositions of 50/50 wt% and with an excess of CER reflected the chemical uniformity of the system (semi-IPN) [22]. Note that no individual degradation stage of the components in CER/LPU grafted semi-IPNs was observed. It was interesting to investigate the characteristics of porous structure and the effect of the pores generation using the irradiation technology and track etching procedure on the complex of properties of CER/LPU grafted semi-IPNs.

6.3. Morphological characterization of nanoporous structure

Fig. 6.1 represents the typical SEM micrographs for porous films of CER-A/LPU and CER-E/LPU grafted semi-IPNs, specifically, CER-A/LPU$_{\gamma,\tau 2}$ (Fig. 6.1*a*) and CER-E/LPU$_{\gamma,\tau 2}$ (Fig 6.1*b*). SEM photos for the other samples are not shown here. One can see the generation of well-defined nanoporous structures in the CER/LPU grafted semi-IPNs. The pore size distribution diagrams for different stages of pore generation in all CER/LPU grafted semi-IPNs are given in Fig. 6.2. The results of calculations on the basis of the SEM micrographs and *ImageJ* and *OriginLab* softwares are summarized in Table 6.2. A quantitative analysis of the porous structures showed the presence of numerous black areas of high circularity corresponding to pore diameters (D_p) sized from ~4 to ~27 nm with a predominant majority of pores not larger than ~15 nm. Increasing etching time and using sensitization for both the CER-A/LPU and the CER-E/LPU samples resulted in significantly increasing their total porosity (Table 6.3). It should be noted that the value of the total porosity of the studied nanoporous samples is not related only to the content of the LPU component in the samples, since α-particles penetrate both LPU and CER fragments of grafted semi-IPNs, and after etching of tracks, pores are formed everywhere in these samples.

It is known that sensitization ensures a more selective etching, and the samples sensitized before etching are characterized by a better defined and more regular porous structure with narrower pore size distribution per unit area. Sensitization was carried out in order to increase the material destruction along the tracks. This allowed for speeding up the process of film etching, and it was carried out by additional processing with sufficiently powerful irradiation [82—84]. One can see that extension of etching time from τ_1 = 30 to τ_2 = 180 min leads to increasing the total porosity by 3 and ~2 times for the CER-A/LPU and CER-E/LPU grafted semi-IPNs created, correspondingly. The additional sensitization during short-term etching increased the total porosity value by ~1.5 and 1.8 times, whereas during long-term etching — only by ~8% and 13% for the nanoporous CER-A/LPU and CER-E/LPU grafted semi-IPNs created, respectively. Thus, the sensitization with γ-rays facilitates and improves the efficiency of track etching. Moreover, increasing etching time leads to narrowing the pore size distribution (decreasing ΔD_p), but almost do not affect the average pore diameter ($D_{p(av)}$) (Table 6.2). Using an additional sensitization leads to some narrowing of pore size distribution and some increasing $D_{p(av)}$ values (Table 6.2). Thus, by varying the etching duration and using sensitization of CER/LPU grafted semi-IPNs, one can tune the porosity of such materials.

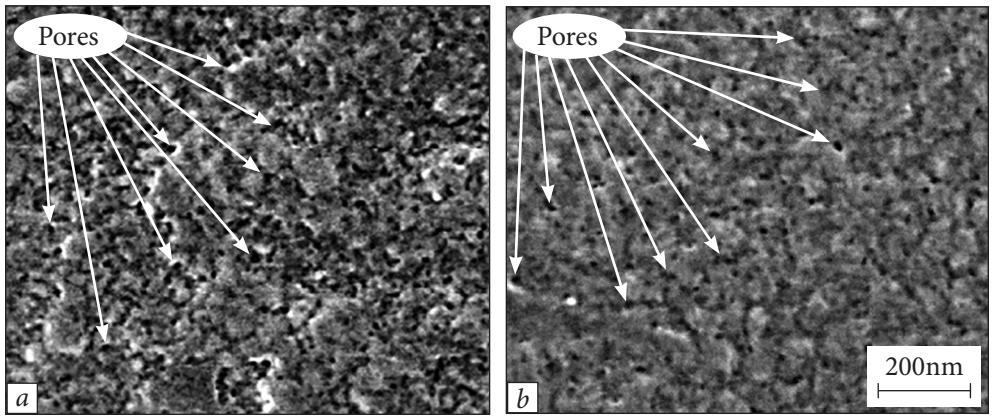

Fig. 6.1. Typical SEM micrographs for nanoporous CER/LPU grafted semi-IPNs created: *a* — CER-A/LPU$_{\gamma,\tau 2}$; *b* — CER-E/LPU$_{\gamma,\tau 2}$. Some pores are indicated with arrows

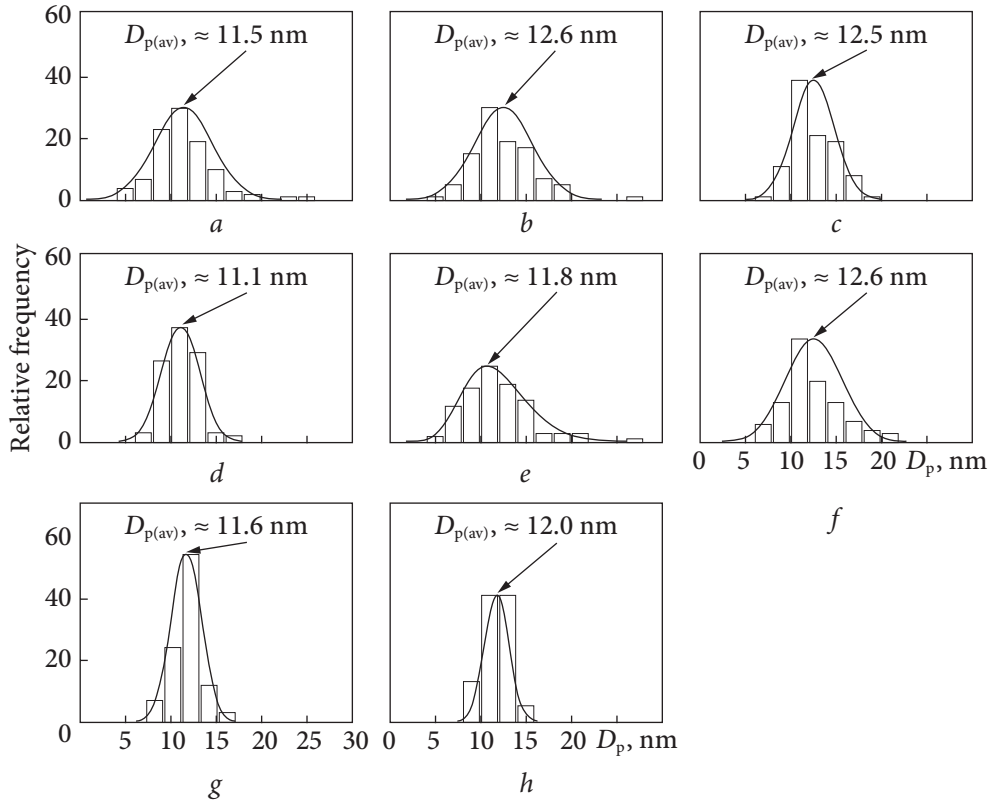

Fig. 6.2. Pore size distribution diagrams (from SEM data) for (*a-d*) nanoporous CER-A/LPU and (*e-h*) CER-E/LPU grafted semi-IPNs created: *a* — CER-A/LPU$_{\tau 1}$, *b* — CER-A/LPU$_{\gamma,\tau 1}$, *c* — CER-A/LPU$_{\tau 2}$, and *d* — CER-A/LPU$_{\gamma,\tau 2}$; *e* — CER-E/LPU$_{\tau 1}$, *f* — CER-E/LPU$_{\gamma,\tau 1}$, *g* — CER-E/LPU$_{\tau 2}$, and *h* — CER-E/LPU$_{\gamma,\tau}$

The average pore diameter in track technologies is determined both by the type and size of charged particles used for irradiation and by the conditions of sensitization and chemical etching. During α-irradiation, tracks of uniform size are formed in the samples that contain fragments of destroyed CER and LPU macromolecules. Then, as a result of their washing out from the tracks in the process of chemical etching, pores are formed. Alpha particles penetrate both LPU fragments and CER matrixes of the grafted semi-IPNs. Thus, after etching the tracks, a regular porous structure is formed. It is known that the longer the etching time, the larger the pore volume. We assume that in the CER/LPU grafted semi-IPNs, LPU fragments are etched more easily, while CER fragments require more time due to slower diffusion of the etching solution inside the more rigid densely crosslinked CER network as compared to LPU. An increase in the total porosity with increasing etching time or with using additional sensitization was predictable since both of these factors cause the appearance of additional pores, apparently in those parts of the sample where the etching lasts longer (CER fragments). At the same time, some narrowing of the pore size distribution (12—15 nm) was not expected, and it can be assumed that this is due to an increase in the number of pores close to the average size and a decrease in the proportion of large pores. In a series of these samples, the average pore diameter practically does not change because it is specified by the size of alpha particles that generate tracks of the same size, and by the etching solution chosen, which provides the formation of pores of similar sizes.

In order to confirm the observations and conclusions from SEM measurements on the nanoporous structures generated, DSC-based thermoporometry was performed for the CER-E/LPU samples obtained. Fig. 6.3*a* demonstrates typical DSC thermoporometry curves for melting ice crystallites of pure water and for ice crystallites of water inside the swollen nanoporous CER-E/LPU$_{\tau 1}$ sample onlyendothermic peak with $T_{m0} \approx 2.1$ °C of melting ice crystallites of pure water is present on the corresponding DSC thermoporometry curve.

Table 6.2. **Morphological characteristics of nanoporous materials as determined by SEM**

Sample	D_p / ΔD_p^*, nm	$D_{p(av)}$, nm	Total porosity, %	Sample	D_p / ΔD_p^*, nm	$D_{p(av)}$, nm	Total porosity, %
CER-A/LPU$_{\tau 1}$	4—27 / 23	11.5	13.8	CER-E/LPU$_{\tau 1}$	5—27 / 22	11.8	10.9
CER-A/LPU$_{\gamma,\tau 1}$	5—26 / 21	12.6	21.2	CER-E/LPU$_{\gamma,\tau 1}$	6—22 / 16	12.6	19.1
CER-A/LPU$_{\tau 2}$	6—20 / 14	12.5	41.8	CER-E/LPU$_{\tau 2}$	7—17 / 10	11.6	22.1
CER-A/LPU$_{\gamma,\tau 2}$	7—18 / 11	11.1	45.2	CER-E/LPU$_{\gamma,\tau 2}$	8—15 / 7	12.0	24.9

* $\Delta D_p = D_{p(max)} - D_{p(min)}$.

However, for the swollen nanoporous CER-E/LPU$_{\tau 1}$ sample, there are two endothermic peaks with $T_{m0} \approx 2.3$ °C and $T_{m(Rav)} \approx 0.7$ °C related to melting ice crystallites inside the pores (Fig. 6.3*a*, curve *1*) and melting ice crystallites in of the sample bulk (Fig. 6.3*a*, curve *2*).

Note, the cumulative curve of the Gaussian approximation (curve *3*) is in good correlation with the experimental data obtained for the swollen nanoporous CER-E/LPU$_{\tau 1}$ sample (Fig. 6.3*a*, filled squares). Similar DSC thermoporometry curves were obtained for other swollen nanoporous CER-E/LPU grafted semi-IPNs (not shown here).

The calculations made from DSC-based thermoporometry measurements confirmed the generation of nanoporous structures in all the samples, regardless of etching and sensitization conditions (Fig. 6.3*b, c* Table 6.3). Table 6.3 informs that the pore size distribution was in the range of ~15—75 nm and ~15—55 nm for the short-term and long-term etched CER-E/LPU samples, respectively, and their average pore diameters were centered within ~26—33.5 nm. Thus, it found that an increase in the etching time leads to some narrowing of pore diameter distribution, and significant increase (approximately by ~10 times) in the pore volume (V_p) for the compositions studied.

Note that the pore sizes determined by SEM and DSC-based thermoporometry are slightly different. It can be explained by the difference in the techniques applied. SEM allows determining the pores located on the sample surface only, whereas the DSC-thermoporometry allows counting the pores and their size not only on the surface but also inside the sample. It is an experimental fact that according to the results of DSC thermoporometry, the average pore size is indeed larger (Table 6.3) than that according to the SEM data (Table 6.2).

The SEM microphotographs (Fig. 6.1) evidence that during the bombardment, a significant part of the alpha particles forms closely spaced tracks.

It can be assumed that during chemical etching, these tracks, increasing in size, are combined due to the destruction of common walls, which leads to the formation of joint wider pores inside the sample. Since it is known that the etching rate of the surface of a polymer sample is much lower than that in tracks (the destroyed fragments of macromolecules inside the tracks are washed out

Table 6.3. **Main porosity characteristics for nanoporous CER-E/LPU grafted semi-IPNs as determined by DSC-based thermoporometry**

Composition	D_p / ΔD_p, nm	$D_{p(av)}$, nm	V_p, $cm^3 \times g^{-1}$	Composition	D_p / ΔD_p, nm	$D_{p(av)}$, nm	V_p, $cm^3 \times g^{-1}$
CER-E/LPU$_{\tau 1}$	15—75/60	33.5	0.03	CER-E/LPU$_{\tau 2}$	15—50/35	26.0	0.67
CER-E/LPU$_{\gamma,\tau 1}$	15—70/55	27.5	0.07	CER-E/LPU$_{\gamma,\tau 2}$	15—55/40	27.3	0.76

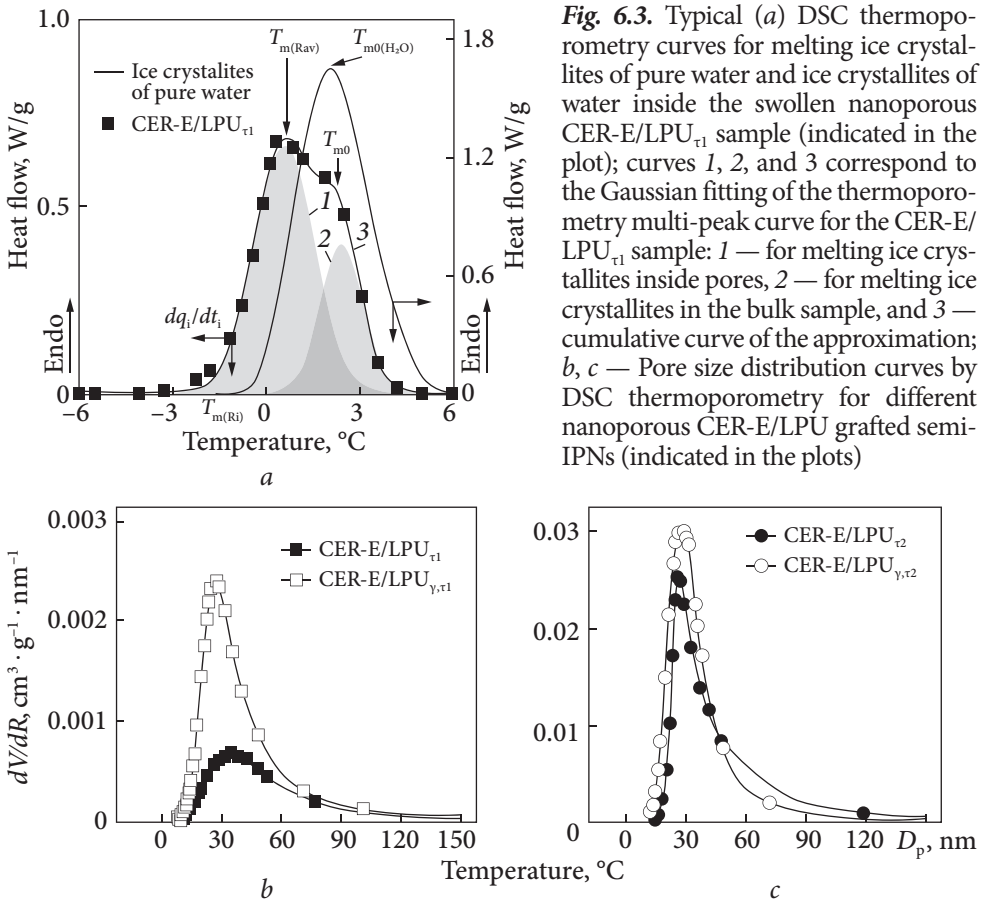

Fig. 6.3. Typical (*a*) DSC thermoporometry curves for melting ice crystallites of pure water and ice crystallites of water inside the swollen nanoporous CER-E/LPU$_{\tau 1}$ sample (indicated in the plot); curves *1*, *2*, and 3 correspond to the Gaussian fitting of the thermoporometry multi-peak curve for the CER-E/LPU$_{\tau 1}$ sample: *1* — for melting ice crystallites inside pores, *2* — for melting ice crystallites in the bulk sample, and *3* — cumulative curve of the approximation; *b*, *c* — Pore size distribution curves by DSC thermoporometry for different nanoporous CER-E/LPU grafted semi-IPNs (indicated in the plots)

faster), that is why closely spaced pores on the sample surface remain intact, as seen in SEM micrographs. Therefore, the *Image J* program considers such pores as separate, and as a result, the average pore size calculated from the SEM microphotographs is smaller than that determined by DSC thermoporometry.

6.4. FTIR investigation of chemical structure associated with nanoporous grafted semi-IPNs

FTIR spectra of all the nanoporous samples studied are shown in Fig. 6.4. The chemistry of CER polycyclotrimerization with the formation of polycyanurate network has been studied in detail using FTIR spectroscopy before [87, 88] as well as in the present of LPU with the formation of so-called grafted semi-interpenetrating polymer networks. All the characteristic bands are well-known and described more than once.

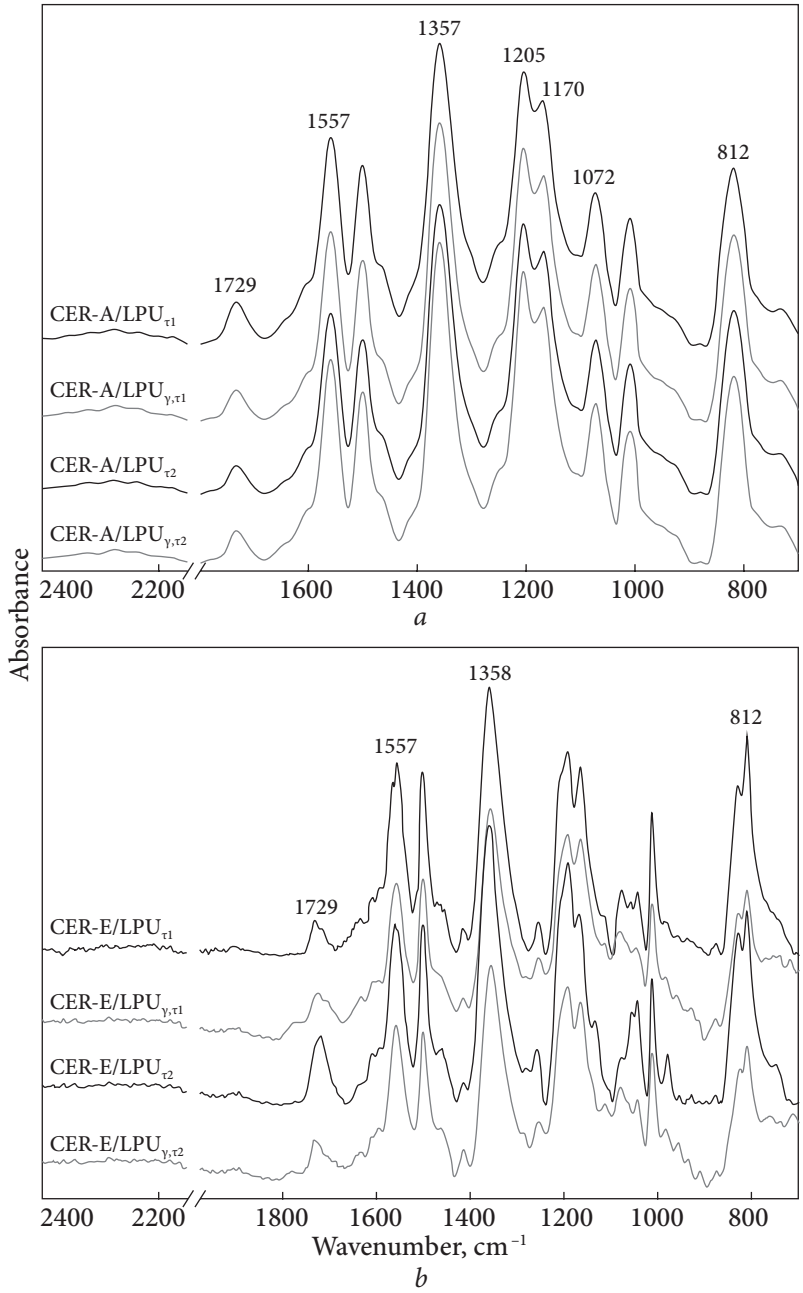

Fig. 6.4. FTIR spectra for nanoporous grafted semi-IPNs based on CER-A/LPU (*a*), and CER-E/LPU (*b*) (indicated in the plots)

Also, it was found that α-irradiation, when applying the sensitization prior to etching and increasing the etching duration, brings a slight decrease in the intensity of some absorption vibrations for all the samples studied. More specifically, such changes were manifested at 1078—1043 cm^{-1} reflecting C—O—C stretching vibrations, as well as at 1729 cm^{-1} corresponding to C=O of the urethane group stretching vibrations. These alterations in the chemical structure of the materials are probably caused by a minor breakage of chemical bonds in junctions and/or internodal fragments of polymer networks with subsequent chain termination and recombination reactions during the irradiation procedure, followed by the removal of fragments of destroyed macromolecules formed from the tracks through subsequent chemical etching.

Accordingly, the chemical structure of all the final porous samples was mainly preserved after irradiation applied, etching treatment, and even when subjected to additional sensitization.

6.5. Investigation of thermal properties using TGA and DSC techniques

The influence of the polymer matrix structure and polymer sample treatment on the thermal stability of the nanoporous CER/LPU grafted semi-IPNs was investigated by TGA. Figs. 6.5 and 6.6 display the mass loss and the corresponding derivative curves for the nanoporous CER-A/LPU and CER-E/LPU grafted semi-IPNs, respectively. Comparison of the TGA results for nanoporous CER-E/LPU and CER-A/LPU grafted semi-IPNs show that the latter are characterized by higher resistance to thermal degradation, which is logical since the CER-A matrix has improved thermal stability compared to the CER-E matrix [3].

It was found that the thermal behavior of all the systems studied does not depend significantly on the duration of etching and additional sensitization: the shape of the curves and the number of stages for different samples are similar. This fact indicates that the cumulative thermal stability of the final nanoporous materials remains sufficiently high after irradiation and chemical treatment them for nanoporous structure formation. For all the nanoporous grafted semi-IPNs, the degradation temperature onset, $T_{d\ onset}$, was found to be within 320—350 °C depending on the polymer matrix, and the main decomposition process consisting of one degradation stage occurred at 400—500 °C corresponding to the breakage of triazine cycles, followed by the CER skeleton destruction [88]. Char residue determined at $T \sim 700$ °C for all the compositions investigated varied from 37 to 42%.

The dependence of thermal degradation temperatures on the sample treatment for nanoporous CER-A/LPU and CER-E/LPU grafted semi-IPNs is shown

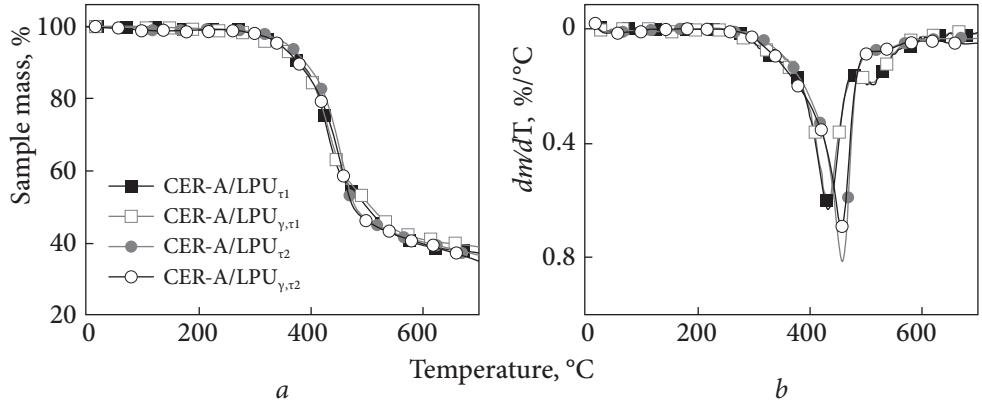

Fig. 6.5. TGA (*a*) and DTG (*b*) curves obtained for nanoporous CER-A/LPU grafted semi-IPNs created (indicated in the plots)

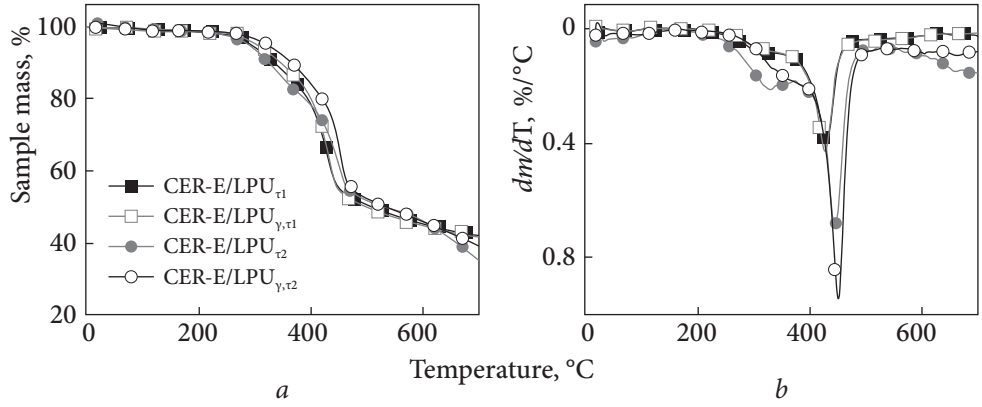

Fig. 6.6. TGA (*a*) and DTG (*b*) curves for nanoporous CER-E/LPU grafted semi-IPNs created (indicated in the plots)

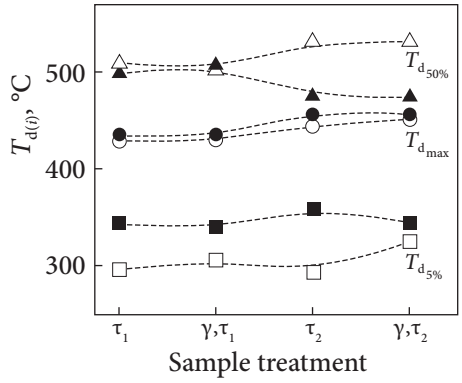

Fig. 6.7. Temperatures of thermal degradation ($T_{d(i)}$) versus sample treatment method for nanoporous grafted semi-IPNs: CER-A/LPU (solid symbols) and CER-E/LPU (open symbols). The $T_{d5\%}$, $T_{d50\%}$, and $T_{d\ max}$ are the temperatures corresponding to the indicated sample mass losses (subscript) and maxima of DTG peaks, respectively

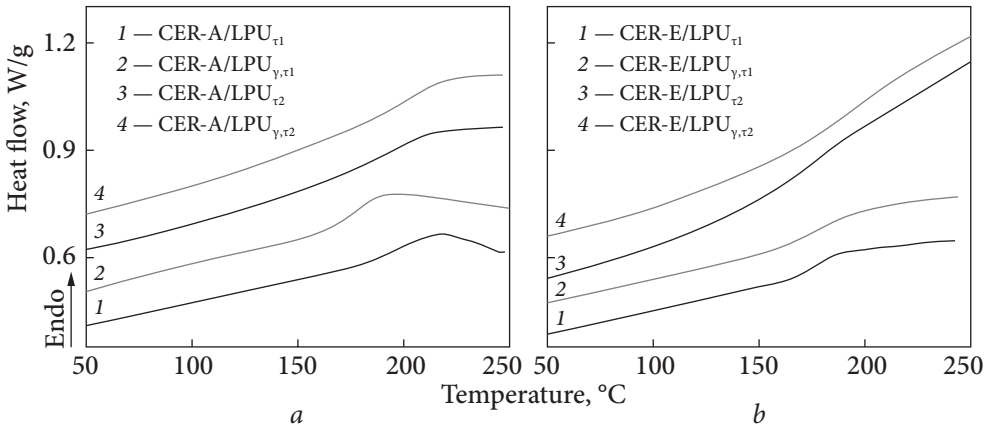

Fig. 6.8. DSC thermograms (2nd heating scan) for nanoporous CER/LPU semi-IPNs created. The curves are shifted vertically for the sake of clarity

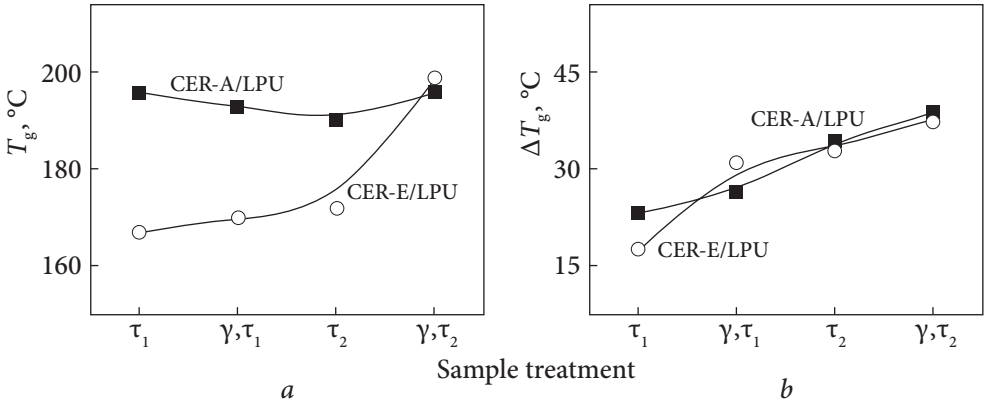

Fig. 6.9. Glass transition temperature, T_g, (a) and glass transition interval, ΔT_g, (b) *versus* the sample treatment method for nanoporous CER/LPU grafted semi-IPNs created

in Fig. 6.7. As seen, the temperatures corresponding to the 5% mass loss fall in the range of ≈293—325 °C and ≈339—359 °C correspondingly for CER-E/LPU and CER-A/LPU nanoporous grafted semi-IPNs.

Moreover, additional sensitization shifted the $T_{d5\%}$ values to higher temperatures by 10 °C for short-term etched and by 32 °C for long-term etched CER-E/LPU grafted semi-IPNs, whereas the $T_{d5\%}$ values for CER-A/LPU grafted semi-IPNs slightly decreased by ≈4 and 14 °C for short-term and long-term etching procedures, respectively. It was found that for both short-term and long-term etched samples, the additional sensitization did not affect significantly thermal stability, whereas an increase in etching time from 30 to 180 min shifted the $T_{d\,max}$ values to higher temperatures by ~16—25 °C (Fig. 6.7). One can conclude

that the combination of sensitization and longer time chemical etching enhances the process of removing macrochain debris formed due to the tracks and pore formation.

A thorough analysis of the DSC curves presented in Fig. 6.8 shows a single endothermic transition in the temperature range from ~167 to ~199 °C corresponding to the devitrification of the CER/LPU-based grafted semi-IPNs in the thermograms for all the nanoporous samples studied.

The dependences of glass transition temperature (T_g) and glass transition interval (ΔT_g) on the sample treatment method for the nanoporous CER-A/LPU and CER-E/LPU grafted semi-IPNs are depicted in Fig. 6.9.

For both series of samples, the additional sensitization and etching duration do not significantly affect the glass transition temperature, except for the CER-E/LPU$_{\gamma,\tau 2}$ hybrid network (Fig. 6.9*a*). At the same time, the ΔT_g for both CER-A/LPU and CER-E/LPU grafted semi-IPNs created is directly related to the sample treatment, namely, the longer the etching procedure with using the additional sensitization, the larger the glass transition interval (Fig. 6.9*b*), likely due to the formation of more defective structure of higher porosity.

6.6. Gas transport properties of nanoporous grafted semi-IPNs

The permeability of different gases was determined for the nanoporous CER-E/LPU grafted semi-IPNs. The results are shown in Table 6.4 which also contains the kinetic diameter values of the studied gases [63]. It is clearly seen that the CER-E/LPU nanoporous grafted semi-IPNs possess high permeability coefficients for all the gases investigated. Indeed, gas permeability values of dense CER-E based films are ~0.7 barrer for O_2, as an example [62]. Moreover, the additional sensitization contributes to increasing the transport properties of the nanoporous CER-E/LPU grafted semi-IPNs developed for gases, including O_2, CO_2, N_2, and CH_4 (the permeability coefficient increases by ~1.2—1.8 times depending on the gas). These trends are in good agreement with those observed in SEM data.

Table 6.4. **Gas permeability (*P*) of the nanoporous CER-E/LPU based grafted semi-IPNs with respect to the kinetic diameter of the diffusing gases (the uncertainty is equal to ±7%)**

Parameter	O_2	CO_2	N_2	CH_4
Gas kinetic diameter (Å)	2.92	3.23	3.64	3.8
P for CER-E/LPU$_{\tau 2}$ (barrer)	1117	1197	1256	1742
P for CER-E/LPU$_{\gamma,\tau 2}$ (barrer)	1801	1925	2010	3064

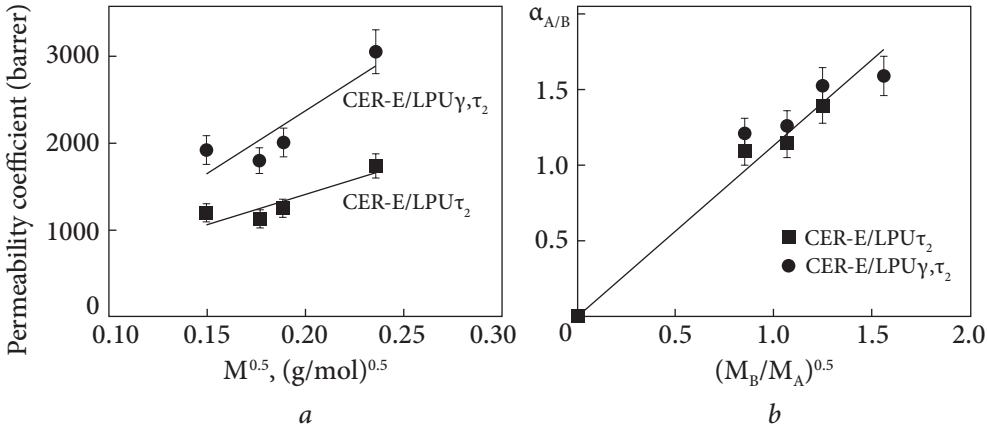

Fig. 6.10. Transport properties of different gases for nanoporous CER-E-based grafted semi-IPNs treated in different conditions: *a* — Permeability coefficients as a function of the square root of the molar mass of the diffusing molecule; *b* — Gas selectivity as a function of the square root of the inverse molar mass ratio of the molecular masses of the diffusing molecules for the gas pairs CO_2/O_2, CH_4/N_2, N_2/O_2, CH_4/CO_2

The data in Table 6.4 indicate that the permeability is not governed by the kinetic diameter of the diffusing molecule. Indeed, the permeability values measured for CH_4 are the highest, whereas this gas has the highest kinetic diameter. On the other hand, as shown in Fig. 6.10*a*, a linear relation could be established between the gas permeability and the inverse of the square root of the molar mass of the diffusing species, meaning that the gas transport properties are governed by the Knudsen mechanism. Thus, the small size of the created pores favors gas-pore walls' collisions. The shift toward higher permeability values is evidenced as the sensitization step was added without modifying the gas transport mechanism. This behavior is in good correlation with the observed morphology. Indeed, the average pore diameter and pore size distribution were not significantly modified by the sensitization step, whereas the total pore content increased. Concerning the gas separation properties of track-etched membranes created, the experimental selectivity values between two gases A and B ($\alpha_{A/B}$) can be calculated from the experimental permeability values according to:

$$\alpha_{A/B} = P_A/P_B. \qquad (6.1)$$

Fig. 6.10*b* shows that the experimental selectivity calculated for the different gas pairs (A/B) considered in this work (CO_2/O_2, CH_4/N_2, N_2/O_2, CH_4/CO_2) is directly related to the square root of the inverse molar mass ratio of the considered gases (*i.e.* $\sqrt{M_B}\,/\sqrt{M_A}$). It is noteworthy that the sensitization step does not lead to any significant modification of the gas selectivity for our membranes. Thus, by adding this step, it was is possible to increase the permeability without any loss of selectivity.

6.7. Conclusions

The implementation of a track-etching technique consisting in α-irradiation of CER/LPU-based thermosetting films with subsequent chemical etching has provided well-defined nanoporous structures. Such nanoporous materials were characterized by SEM to investigate the generation of uniform nanosized pores with no essential effect on the chemical structure of the polymer system, as determined from FTIR spectroscopy measurements. It is noteworthy that all the CER/LPU nanoporous grafted semi-IPNs derived from DCBA and DCBE monomers had a quite narrow pore diameter distribution and average pore diameters of ~12 nm. Increasing etching time for grafted semi-IPNs resulted in narrowing pore size distribution and increasing total porosity, while it almost did not affect the average pore diameter. Using an additional sensitization step led to some narrowing of pore size distribution and an increase in the average pore diameter and total porosity as well. DSC and TGA measurements showed that the cumulative thermal stability of the final nanoporous films remained sufficiently high ($T_{d5\%}$ ~ 293—359 °C). The CER/LPU nanoporous thermosetting materials demonstrated effective gas transport properties tested with gases such as O_2, CO_2, N_2, and CH_4. The combination of an additional sensitization using γ-rays and a longer time of chemical etching improved the properties of the nanoporous systems developed as the gas permeability increased without any loss of gas selectivity.

This investigation opens the way to numerous potential applications for the materials created, for example, as selective membranes for advanced technologies, especially under extreme conditions.

REFERENCES

1. Odani, H., Masuda, T. (1992). Design of polymer membranes for gas separation. In: N. Toshima (Ed.) Polymers for Gas Separation (107-144), New York: Wiley-VCH.
2. Pereira-Nunes, S., Peinemann, K.V. (Eds.). (2001). Membrane technology in the chemical industry. Weinheim: Wiley-VCH.
3. Hamerton, I. (Ed.). (1994). Chemistry and technology of cyanate ester resins. Glasgow: Chapman & Hall.
4. Nair, C.P.R., Mathew, D. & Ninan, K.N. (2001). Cyanate ester resins, recent developments. *Adv. Polym. Sci.*, 155, pp. 1-99. https://doi.org/10.1007/3-540-44473-4_1
5. Trautmann, C., Brüchle, W., Spohr, R., Vetter, J. & Angert. N. (1996). Pore geometry of etched ion tracks in polyimide. *Nucl. Instrum. Methods. Phys. Res.*, B111, pp. 70-74. https://doi.org/10.1016/0168-583X(95)01264-8
6. Apel, P. (2001). Track etching technique in membrane technology. *Rad. Measur.*, 34, pp. 559-566. https://doi.org/10.1016/S1350-4487(01)00228-1
7. Apel, P.Yu., Blonskaya, I.V., Dmitriev, S.N., Orelovitch, O.L. & Sartowska, B.J. (2006). Structure of polycarbonate track-etch membranes: Origin of the "paradoxical" pore shape. *J. Membr. Sci.*, 282, pp. 393-400. https://doi.org/10.1016/j.memsci.2006.05.045
8. Musket, R.G. (2006). Extending ion-track lithography to the low-energy ion regime. *J. Appl. Phys.*, 99, pp. 114314-114315. https://doi.org/10.1063/1.2200387
9. Hedrick, J., Labadie, J., Russell, T., Hofer, D. & Warharker, V. (1993). High temperature polymer foams. *Polymer*, 34, pp. 4717-4126. https://doi.org/10.1016/ 0032-3861(93)90707-H
10. Hedrick, J.L., Miller, R.D., Hawker, C.J., Carter, K.R., Volksen, W., Yoon, D.Y. & Trollsås, M. (1998). Templating nanoporosity in thin film dielectric insulators. *Adv. Mater.*, 10, pp. 1049-1053. https://doi.org/10.1002/(SICI)1521-4095 (199809)10:13<1049::AID-ADMA1049>3.0.CO;2-F
11. Hedrick, J.L., Carter, K.R., Labadie, J.W., Miller, R.D., Volksen, W., Hawker, C.J., Yoon, D.Y., Russell, T.P., McGrath, J.E. & Briber, R.M.

(1999). Nanoporous Polyimides. *Adv. Polym. Sci.*, 141, pp. 1-43. https://doi.org/10.1007/3-540-49814-1_1
12. Nguyen, C., Hawker, C.J., Miller, R.D., Huang, E., Hedrick, J.L., Gauderon, R. & Hilborn, J.G. (2000). Hyperbranched polyesters as nanoporosity templating agents for organosilicates. *Macromolecules*, 33, pp. 4281-4284. https://doi.org/10.1021/ma991407v
13. Eigner, M., Voit, B., Estel, K. & Bartha, J.W. (2002). Labile hyperbranched poly(triazene ester)s — decomposition behavior and their use as porogens in thermally stable matrix polymers. *e-Polymers*, 028. Retrieved from https://www.degruyter.com/document/doi/10.1515/epoly.2002.2.1.386/pdf
14. Loera, A.G., Cara, F., Dumon, M. & Pascault, J.P. (2002). Porous epoxy thermosets obtained by a polymerization-induced phase separation process of a degradable thermoplastic polymer. *Macromolecules*, 35, pp. 6291-6297. https://doi.org/10.1021/ma011567i
15. Kiefer, J., Hilborn, J.G., Hedrick, J.L., Cha, H.J., Yoon, D.Y. & Hedrick, J.C. (1996). Microporous cyanurate networks via chemically induced phase separation. *Macromolecules*, 29, pp. 8546-8548. https://doi.org/10.1021/ma960960z
16. Kiefer, J., Porouchani, R., Mendels, D., Ferrer, J.B., Fond, C., Hedrick, J.L., Kausch, H.H. & Hilborn, J.G. (1996). Macroporous thermosets via chemically induced phase separation. *Micropor. Macropor. Mater.*, 431, pp. 527-532. https://doi.org/10.1557/PROC-431-527
17. Hedrick, J.L., Russell, T.P., Hedrick, J.C. & Hilborn, J.G. (1996). Microporous polycyanurate networks. *J. Polym. Sci.*, Part A: Polym. Chem., 34, pp. 2879-2888. https://doi.org/10.1002/(SICI)1099-0518(199610)34:14<2879::AID-POLA5>3.0.CO;2-M
18. Bershtein, V.A., Egorova, L.M., Ryzhov, V.A., Yakushev, P.N., Fainleib, A.M., Shantalii, T.A. & Pissis, P. (2001). Structure and segmental dynamics heterogeneity in hybrid polycyanurate/polyurethane networks. *J. Macromol. Sci.*, Part B Phys., 40, pp. 105-131. https://doi.org/10.1081/MB-100000057
19. Fainleib, A.M., Grigoryeva, O.P. & Hourston, D.J. (2001). Structure-properties relationships for bisphenol A polycyanurate network modified with polyoxytetramethylene glycol. *Int. J. Polym. Mat.*, 51, pp. 57-75. https://doi.org/10.1080/00914030213025
20. Fainleib, A., Grigoryeva, O. & Hourston, D. (2001). Synthesis of inhomogeneous modified polycyanurates by reactive blending of bisphenol A dicyanate ester and polyoxypropylene glycol. *Macromol. Symp.*, 164, pp. 429-442. https://doi.org/10.1002/1521-3900(200102)164:1<429::AID-MASY429>3.0.CO;2-I
21. Fainleib, A., Hourston, D., Grigoryeva, O., Shantalii, T. & Sergeeva, L. (2001). Structure development in aromatic polycyanurate networks modified with hydroxylterminated polyethers. *Polymer*, 42, pp. 8361-8372. https://doi.org/10.1016/S0032-3861(01)00333-0
22. Fainleib, A., Kozak, N., Grigoryeva, O., Nizelskii, Y., Grytsenko, V., Pissis, P. & Boiteux G. (2002). Structure-thermal property relationships for polycyanurate-polyurethane linked interpenetrating polymer networks. *Polym. Degrad. Stab.*, 76, pp. 393-399. https://doi.org/10.1016/S0141-3910(02)00031-9
23. Fainleib, A., Grenet, J., Garda, M.R., Saiter, J.M., Grigoryeva, O., Grytsenko, V., Popescu, N. & Enescu, M.C. (2003). Poly(bisphenol A)cyanurate network modified with poly(butylene glycol adipate). Thermal and mechanical properties. *Polym. Degrad. Stab.*, 81, pp. 423-430. https://doi.org/10.1016/S0141-3910(03)00127-7

24. Grigoryeva, O., Fainleib, A. & Sergeeva, L.M. (2005). Thermoplastic polyurethane elastomers in interpenetrating polymer networks. In: Fakirov, S. (Ed.) Handbook of condensation thermoplastic elastomers (pp. 325-354), Weinheim: Wiley-VCH.
25. Fainleib, A., Grigoryeva, O., Garda, M.R., Saiter, J.-M., Lauprêtre, F., Lorthioir, C. & Grande, D. (2007). Synthesis and characterization of polycyanurate networks modified by oligo(ε-caprolactone) as precursors of porous thermosets. *J. Appl. Polym. Sci.*, 106, pp. 929-3938. https://doi.org/10.1002/app.27039
26. Grande, D., Grigoryeva, O., Fainleib, A., Gusakova, K. & Lorthioir, C. (2008). Porous thermosets via hydrolytic degradation of poly(ε-caprolactone) fragments in cyanurate-based hybrid networks. *Eur. Polym. J.*, 44, pp. 3588-3598. https://doi.org/10.1016/j.eurpolymj.2008.08.041
27. Elzein, T., Nasser-Eddine, M., Delaite, C., Bistac, S. & Dumas, P. (2004). FTIR study of polycaprolactone chain organization at interface. *J. Colloid. Interface Sci.*, 273, pp. 381-387. https://doi.org/10.1016/j.jcis.2004.02.001
28. Colthup, N.B., Daly, L.H. & Wiberley, S.E. (Eds.). (1990). Introduction to infrared and Raman spectroscopy. San Diego: Academic Press.
29. Rohman, G., Lauprêtre, F., Boileau, S., Guérin, Ph. & Grande, D. (2007). Poly (d,llactide)/poly(methyl methacrylate) interpenetrating polymer networks: Synthesis, characterization, and use as precursors to porous polymeric materials. *Polymer*, 48, pp. 7017-7028. https://doi.org/10.1016/j.polymer.2007.09.044
30. Fyfe, C.A., Niu, J., Rettig, S.J., Burlinson, N.E., Reidsema, C.M., Wang, D.W. & Poliks, M. (1992). Highresolution ^{13}C and ^{15}N NMR invesigations of the mechanism of the curing reactions of cyanate-based polymer resins in solution and the solid state. *Macromolecules*, 25, pp. 6289-6301. https://doi.org/ 10.1021/ma00049a028
31. Grenier-Loustalot, M.F., Lartigau, C. & Grenier, P. (1995). A study of the mechanisms and kinetics of the molten state reaction of non-catalyzed cyanate and epoxy-cyanate systems. *Eur. Polym. J.*, 31, pp. 1139-1153. https://doi.org/ 10.1016/0014-3057(95)00063-1
32. Wang, J., Cheung, M.K. & Mi, Y. (2002). Miscibility and morphology in crystalline/amorphous blends of poly(caprolactone)/poly(4-vinylphenol) as studied by DSC, FTIR, and ^{13}C solid state NMR. *Polymer*, 43, pp. 1357-1364. https://doi.org/10.1016/S0032-3861(01)00673-5
33. Keroack, D., Zhao, Y. & Prud'homme, R.E. (1998). Molecular orientation in crystalline miscible blends. *Polymer*, 40, pp. 243-251. https://doi.org/ 10.1016/S0032-3861(98)00187-6
34. Brun, M., Lallemand, A., Quinson, J.F. & Eyraud, C. (1997). A new method for the simultaneous determination of the size and the shape of pores: thermoporometry. *Thermochim. Acta*, 21, pp. 59-88. https://doi.org/10.1016/0040-6031(77)85122-8
35. Quinson, J.F., Mameri, N., Guihard, N. & Bariou, B. (1991). The study of the swelling of an ultrafiltration membrane under the influence of solvents by thermoporometry and measurements of permeability. *J. Membr. Sci.*, 58, pp. 191-200. https://doi.org/10.1016/S0376-7388(00)82455-2
36. Hay, J.N. & Laity, P.R. (2000). Observations of water migration during thermoporometry. Studies of cellulose films. *Polymer*, 41, pp. 6171-6180. https://doi.org/10.1016/S0032-3861(99)00828-9
37. Nedelec, J.M. & Baba, M. (2004). Abnormal phase transition temperature of liquids in divided media: New applications of thermoporosimetry to polymer science. *Recent Res. Devel. Physical Chem.*, 7 pp. 381-410.

38. Grande, D., Gusakova, K., Grigoryeva, O. & Fainleib, A. (2009). Original approaches to nanoporous cyanurate-based thermosetting films. *Polym. Mater. Sci. Eng.*, 101, pp. 1375-1376.
39. Grigat, E., Putter, R. (1967). Synthesis and reactions of cyanic esters. *Angew Chem. Int. Ed.*, 6 pp. 206-218. https://doi.org/10.1002/anie.196702061
40. Grigoryeva, O., Gusakova, K., Fainleib, A. & Grande D. (2011). Nanopore generation in hybrid polycyanurate/poly(ε-caprolactone) thermostable networks. *Eur. Polym. J.*, 47, pp. 1736-1745. https://doi.org/10.1016/j.eurpolymj.2011.06.004
41. Reverchon, E., Cardea, S. & Rappo, E.S. (2006). Production of loaded PMMA structures using the supercritical CO_2 phase inversion process. *J. Membr. Sci.*, 273, pp. 97-105. https://doi.org/10.1016/j.memsci.2005.09.042
42. Zeman, L. & Denault, L. (1992). Characterization of microfiltration membranes by image analysis of electron micrographs: Part I. Method development. *J. Membr. Sci.*, 71, pp. 221-31. https://doi.org/10.1016/0376-7388(92)80207-Z
43. Zeman, L. (1992). Characterization of microfiltration membranes by image analysis of electron micrographs: Part II. Functional and morphological parameters. *J. Membr. Sci.*, 71, pp. 233-246. https://doi.org/10.1016/0376-7388(92)80208-2
44. Weast, R.C. (Ed.). (1974). Handbook of chemistry and physics. 55th Edition. Cleveland: CRC Press.
45. Wu, D., Xu, F., Sun, B., Fu, R., He, H. & Matyjaszewski, M. (2012). Design and preparation of porous polymers. *Chem. Rev.*, 112, pp. 3959-4015. https://doi.org/10.1021/cr200440z
46. Li, J., Du, Z., Li, H. & Zhang, C. (2009). Porous epoxy monolith prepared via chemically induced phase separation. *Polymer*, 50, pp. 1526-1532. https://doi.org/10.1016/j.polymer.2009.01.049
47. Grande, D., Grigoryeva, O., Fainleib, A. & Gusakova, K. (2013). Novel mesoporous high-performance films derived from polycyanurate networks containing high-boiling temperature liquids. *Eur. Polym. J.*, 49, pp. 2162-2171. https://doi.org/10.1016/j.eurpolymj.2013.05.030
48. Grigoryeva, O., Fainleib, A., Gusakova, K., Starostenko, O., Saiter, J.-M., Levchenko, V., Serghei, A., Boiteux, G. & Grande, D. (2014). Nanoporous Polycyanurates Created by Chemically-Induced Phase Separation: Structure-Property Relationships. *Macromol. Symp.*, Special issue: Rouen symposium in advanced materials — Part II, 341(1), pp. 57–66. https://doi.org/ 10.1002/masy.201300174
49. Georjon, O., Galy, J. & Pascault, J.P. (1993). Isothermal curing of an uncatalyzed dicyanate ester monomer: Kinetics and modeling. *J. Appl. Polym. Sci.*; 49; 1441-52. https://doi.org/10.1002/app.1993.070490812
50. Georjon, O. & Galy, J. (1998). Effect of crosslink density on the volumetric properties of high T_g polycyanurate networks. Consequences on moisture absorption. *Polymer*, 39, pp. 339-345. https://doi.org/10.1016/S0032-3861(97)00267-X
51. Grulke, E.A. (1989). Solubility parameters values. In: Brandrup, J. & Immergut, E.H. (Eds.) Polymer Handbook, 3rd edition (pp. VII/519-59). New York: Wiley.
52. Seferis, J.C. (1989). Refractive indices of polymers. In: Brandrup, J. & Immergut, E.H. (Eds.) Polymer Handbook, 3rd edition. (pp. VII/451-461). New York: Wiley.
53. Van Krevelen, D.W. (1990). Properties of polymers, 3rd edition. New York: Elsevier.
54. Gusakova, K., Saiter, J.-M., Grigoryeva, O., Gouanve, F., Fainleib, A., Starostenko O. & Grande D. (2015). Annealing behavior and thermal stability of nanoporous poly-

mer films based on high-performance cyanate ester resins. *Polym. Degr. Stab.*, 120, pp. 402-409. https://doi.org/10.1016/j.polymdegradstab.2015.07.009
55. Korshak, V.V., Gribkova, P.N., Dmitrenko, A.V., Puchin, A.G., Pankratov, V.A. & Vinogradova, S.V. (1975). Thermal and thermal-oxidative degradation of polycyanates. *Vysokomol. Soed.* A 16, pp. 15-21 (in Russian).
56. Korshak, V.V., Pankratov, V.A., Gribkova, P.N., Puchin, A.G., Pavlova, S.A., Zhuravleva, I.V., Danilov, V.G. & Vinogradova, S.V. (1974). Effect of the structure of polycyanates prepared by polycyclotrimerization of aryl cyanates on their thermal stability. *Vysokomol. Soed.* A 17, pp. 482-485 (in Russian).
57. Ramirez, M.L., Walters, R., Lyon, R.E. & Savitski, E.P. (2002). Thermal decomposition of cyanate ester resins. *Polym. Degrad. Stab.*, 78, pp. 73-82. https://doi.org/10.1016/S0141-3910(02)00121-0
58. Brunauer, S., Emmet, P. & Teller E. (1938). Adsorption of gases in multimolecular layers. *J. Americ. Chem. Soc.*, 60, pp. 309-319. https://doi.org/ 10.1021/ja01269a023
59. Yu, H., Shen, C., Tian, M., Qu, J. & Wang, Z. (2012). Microporous cyanate resins: synthesis, porous structure, and correlations with gas and vapor adsorptions. *Macromolecules*, 45, pp. 5140-5150. https://doi.org/10.1021/ma3008652
60. Yu, H., Shen, C., Tian, M. & Wang, Z. (2013). Micro- and mesoporous polycyanurate networks based on triangular units. *ChemPlusChem*, 78, pp. 498-505. https://doi.org/10.1002/cplu.201300090
61. Damian, C., Escoubes, M. & Espuche, E. (2001). Gas and water transport properties of epoxyamine networks: influence of crosslink density. *J. Appl. Polym. Sci.*, 80, pp. 2058-2066. https://doi.org/10.1002/app.1305
62. Gusakova, K., Fainleib, A., Espuche, E., Grigoryeva, O., Starostenko, O., Gouanve, F., Boiteux, G., Saiter J.-M. & Grande D. (2017). Nanoporous cyanate ester resins: structure-gas transport property relationships. *Nanoscale Res. Let.*, 12, 305 (pp. 1-9) https://doi.org/10.1186/s11671-017-2071-3
63. Crank, J. & Park, G.S. (1968). Diffusion in polymers, London: Academic Press.
64. Saiter, A., Devallencourt, C., Saiter, J.-M. & Grenet, J. (2001). Thermodynamically "strong" and kinetically "fragile" polymeric glass exemplified by melamine formaldehyde resins. *Eur. Polym. J.*, 37, pp. 1083-1090. https://doi.org/ 10.1016/S0014-3057(00)00242-1
65. Appleby, D., Hussey, C.L., Seddon, K.R. & Turp, J.E. (1986). Room-temperature ionic liquids as solvents for electronic absorption-spectroscopy of halide-complexes. *Nature*, 323, pp. 614-616. https://doi.org/10.1038/323614a0
66. Tokuda, H., Tsuzuki, S., Susan, M.A.B.H., Hayamizu, K. & Watanabe, M. (2006). How ionic are room-temperature ionic liquids? An indicator of the physicochemical properties. *J. Phys. Chem*. B 110, pp. 19593-19600. https://doi.org/10.1021/jp064159v
67. Welton, T. (1999). Room-temperature ionic liquids. Solvents for synthesis and catalysis. *Chem. Rev.*, 99, pp. 2071-2083. https://doi.org/10.1021/cr1003248
68. Holbrey, J.D. & Seddon, K.R. (1999). Ionic liquids. *Clean Prod Process*, 1, pp. 223-236. https://doi.org/10.1007/s100980050036
69. Wassersheid, P. & Keim, W. (2000). Ionic liquids — new "Solutions" for transition metal catalysis. *Angew. Chem. Int. Ed.*, 39, pp. 3772-3789. https:// doi.org/10.1002/1521-3773(20001103)39:21<3772::AID-ANIE3772>3.0.CO;2-5
70. Wilkes, J.S. (2004). Properties of ionic liquid solvents for catalysis. *J. Mol. Catal.* A: Chem., 214, pp. 11-17. https://doi.org/10.1016/j.molcata.2003.11.029

71. Mecerreyes, D. (2015). Applications of ionic liquids in polymer science and technology. Berlin: Springer-Verlag.
72. Livi, S., Duchet-Rumeau, J., Gérard, J.F. & Pham, T.N. (2015). Polymers and ionic liquids: a successful wedding. *Macromol. Chem. Phys.*, 216, pp. 359–368. https://doi.org/10.1002/macp.201400425
73. Bara, J.E., Carlisle, T.K., Gabriel, C.J., Camper, D., Finotello, A., Gin, D.L. & Noble, R.D. (2009). Guide to CO_2 separations in imidazolium-based room-temperature ionic liquids. *Ind. Eng. Chem. Res.*, 48, pp. 2739-2751. https://doi.org/10.1021/ie8016237
74. Snedden, P., Cooper, A.I., Khimyak, Y.Z., Scott, K. & Winterton, N. (2005). Crosslinked polymers in ionic liquids: Ionic liquids as porogens. In: Brazel, C.S. & Rogers, D. (Eds.) Ionic liquids in polymer systems: solvents, additives and novel applications (pp. 133-147). Washington, DC: ACS Symposium Series 913. https://doi.org/10.1021/bk-2005-0913.ch009
75. Fainleib, A., Grigoryeva, O., Starostenko, O., Vashchuk, A., Rogalsky, S. & Grande, D. (2016). Acceleration effect of ionic liquids on polycyclotrimerization of dicyanate esters. *eXPRESS Polym. Lett.*, 10, pp. 722-729. https://doi.org/10.3144/expresspolymlett.2016.66
76. Fainleib, A., Vashchuk, A., Starostenko, O., Grigoryeva, O., Rogalsky, S., Nguyen, T.-T.-T. & Grande, D. (2017). Nanoporous polymer films of cyanate ester resins designed by using ionic liquids as porogens. *Nanoscale Res. Lett.*, 12, pp. 126 (1-9) https://doi.org/10.1186/s11671-017-1900-8
77. Billingham, J., Breen, C. & Yarwood, J. (1996). *In situ* determination of Bronsted/Lewis acidity on cation-exchanged clay mineral surfaces by ATR-IR. *Clay Miner.*, 31, pp. 513-522. https://doi.org/10.1180/claymin.1996.031.4.09
78. Fainleib, A. (Ed.) (2010). Thermostable polycyanurates: synthesis, modification, structure and properties. New York: Nova Science Publishers.
79. Zhu, X., Tian, C., Mahurin, S.M., Chai, S.H., Wang, C., Brown, S., Veith, G.M., Luo, H., Liu, H. & Dai, S. (2012). A superacid-catalized synthesis of porous membranes based on triazine frameworks for CO_2 separation. *J. Am. Chem. Soc.*, 134, pp. 10478-10484. https://doi.org/10.1021/ja304879c
80. Fleischer, R.L. & Price, P.B. (1963). Tracks of charged particles in high polymers. Science, 140, pp. 1221-1222. https://doi.org/10.1126/science.140.3572.1221
81. Fleischer, R.L., Price, P.B. & Symes, E.M. (1964). Novel filter for biological materials. Science, 143, pp. 249-250. https://doi.org/10.1126/science.143.3603.249
82. Apel, P. (2001). Track etching technique in membrane technology. *Radiat. Meas.*, 34 559-566. https://doi.org/10.1016/S1350-4487(01)00228-1
83. Apel, P.Y. & Dmitriev, S.N. (2011). Micro- and nanoporous materials produced using accelerated heavy ion beams. *Adv. Nat. Sci: Nanosci. Nanotechnol.*, 2 pp. 013002. https://doi.org/10.1088/2043-6262/2/1/013002
84. Apel, P.Yu. (2013). Track-etching. (pp. emst040). In: Encyclopedia of membrane science and technology. Hoboken: John Wiley & Sons, Inc.
85. Ilić, R., Skvarč, J. & Golovchenko, A.N. (2003). Nuclear tracks: present and future perspectives. *Radiat. Meas.*, 36, pp. 83-88. https://doi.org/10.1016/ S1350-4487(03)00247-6
86. Clough, R.L. (2001). High-energy radiation and polymers: A review of commercial processes and emerging applications. *Nucl. Instrum. Methods. Phys. Res.* B 185, pp. 8-33. https://doi.org/10.1016/S0168-583X(01)00966-1

87. Kaya, D. & Keçeci, K. (2020). Review — Track-etched nanoporous polymer membranes as sensors: A review. *J. Electrochem. Soc.*, 167, pp. 037543. https://doi.org/10.1149/1945-7111/ab67a7
88. Su, C.-S. (1989). The enhancement of the alpha track revelation in Lexan and LR-115 by ultrasonic etching. *Nucl. Instrum. Methods. Phys. Res.* B 44, 97-102. https://doi.org/10.1016/0168-583X(89)90693-9
89. Korolkov, I.V., Gorin, Y.G., Yeszhanov, A.B., Kozlovskiy, A.L. & Zdorovets, M.V. (2018). Preparation of PET track-etched membranes for membrane distillation by photo-induced graft polymerization. *Mat. Chem. Phys.*, 205, pp. 55-63. https://doi.org/10.1016/j.matchemphys.2017.11.006
90. Kravets, L.I., Dmitriev, S.N. & Apel, P.Yu. (2000). Polypropylene track membranes for micro and ultrafiltration of chemically aggressive agents. Joint Institute for Nuclear Research (JINR), 31/46, pp. 1-31 (in Russian).
91. Kitamura, A., Yamaki, T., Yuri, Y., Koshikawa, H., Sawada, S., Yuyama, T., Usui, A. & Chiba, A. (2019). Control of the size of etchable ion tracks in PVDF — Irradiation in an oxygen atmosphere and with fullerene C_{60}. *Nucl. Instrum. Methods. Phys. Res.* B 460, pp. 254-258. https://doi.org/10.1016/j.nimb.2019.06.030
92. Dmitriev, S.N., Kravets, L.I. & Sleptsov, V.V. (1998). Modification of track membrane structure by plasma etching. *Nucl. Instrum. Methods. Phys. Res.* B 142, pp. 43-49. https://doi.org/10.1016/S0168-583X(98)00203-1
93. Apel, P.Yu., Blonskaya, I.V., Oganessian, V.R., Orelovitch, O.L. & Trautmann, C. (2001). Morphology of latent and etched heavy ion tracks in radiation resistant polymers polyimide and poly(ethylene naphthalate). *Nucl. Instrum. Methods. Phys. Res.* B 185, pp. 216-221. https://doi.org/10.1016/S0168-583X(01)00967-3
94. Molokanova, L.G., Nechaev, A.N. & Apel, P.Yu. (2014). The effect of surfactant concentration on the geometry of pores resulting from etching of poly(ethylene naphthalate) films irradiated by high-energy ions. *Colloid J.*, 76, pp. 170-175. https://doi.org/10.1134/S1061933X14020045
95. Wen, Q., Yan, D., Liu, F., Wang, M., Ling, Y., Wang, P., Kluth, P., Schauries, D., Trautmann, C., Apel, P., Guo, W., Xiao, G., Liu, J., Xue, J. & Wang, Y. (2016). Highly selective ionic transport through subnanometer pores in polymer films. *Adv. Funct. Mater.*, 26, pp. 5796-5803. https://doi.org/10.1002/adfm.201601689
96. Nguyen, Q.H., Ali, M., Nasir, S. & Ensinger, W. (2015). Transport properties of track-etched membranes having variable effective pore-lengths. *Nanotechnology*, 26, pp. 485502. https://doi.org/10.1088/0957-4484/26/48/485502
97. Fainleib, O.M., Grigoryeva, O.P., Gusakova, K.G., Sakhno, V.I., Zelinsky, A.G. & Grande, D. (2009). Novel nanoporous thermostable polycyanurates for track membranes. Physics and Chemistry of Solid State, 10, pp. 692-696 (in Ukrainian).

Монографія присвячена синтезу, аналізу структури і морфології, параметрів пористості та фізико-хімічних властивостей термостійких нанопористих поліціануратів, а також можливості їх застосування для газорозділення. Описано нанопористі плівки, отримані з використанням реакційноздатних та інертних порогенів, високо киплячих рідин, неповної конверсії ціанатних мономерів, а також радіаційних технологій (одержання трекових мембран шляхом опромінення тонких плівок поліціануратів із подальшими хімічним травленням і сенсибілізацією).

Наукове видання

НАЦІОНАЛЬНА АКАДЕМІЯ НАУК УКРАЇНИ

ІНСТИТУТ ХІМІЇ ВИСОКОМОЛЕКУЛЯРНИХ СПОЛУК
НАН УКРАЇНИ

ФАЙНЛЕЙБ Олександр Маркович
ГРИГОР'ЄВА Ольга Петрівна
СТАРОСТЕНКО Ольга Миколаївна
ГУСАКОВА Крістіна Геннадіївна
ГРАНДЕ Даніель

ТЕРМОСТІЙКІ НАНОПОРИСТІ ПОЛІЦІАНУРАТИ

Англійською мовою

Редактор-коректор *Т.М. Ярмола*

Художнє оформлення *Є.О. Ільницького*

Технічне редагування *Т.М. Шендерович*

Комп'ютерна верстка *А.В. Цибенко*

Підп. до друку 06.04.2023. Формат 70 × 100/16. Гарн. Minion Pro.
Ум. друк. арк. 9,1. Обл.-вид. арк. 9,64. Тираж 100 прим. Зам. № 6894.

Видавець і виготовлювач Видавничий дім "Академперіодика" НАН України
01024, Київ, вул. Терещенківська, 4

Свідоцтво про внесення до Державного реєстру суб'єктів
видавничої справи серії ДК № 544 від 27.07.2001 р.